National Library of Canada
Acquisitions and Bibliographic Services Branch
395 Wellington Street
Ottawa, Ontario
K1A 0N4

Bibliothèque nationale du Canada
Direction des acquisitions et des services bibliographiques
395, rue Wellington
Ottawa (Ontario)
K1A 0N4

Your file Votre référence

Our file Notre référence

NOTICE

The quality of this microform is heavily dependent upon the quality of the original thesis submitted for microfilming. Every effort has been made to ensure the highest quality of reproduction possible.

If pages are missing, contact the university which granted the degree.

Some pages may have indistinct print especially if the original pages were typed with a poor typewriter ribbon or if the university sent us an inferior photocopy.

Reproduction in full or in part of this microform is governed by the Canadian Copyright Act, R.S.C. 1970, c. C-30, and subsequent amendments.

AVIS

La qualité de cette microforme dépend grandement de la qualité de la thèse soumise au microfilmage. Nous avons tout fait pour assurer une qualité supérieure de reproduction.

S'il manque des pages, veuillez communiquer avec l'université qui a conféré le grade.

La qualité d'impression de certaines pages peut laisser à désirer, surtout si les pages originales ont été dactylographiées à l'aide d'un ruban usé ou si l'université nous a fait parvenir une photocopie de qualité inférieure.

La reproduction, même partielle, de cette microforme est soumise à la Loi canadienne sur le droit d'auteur, SRC 1970, c. C-30, et ses amendements subséquents.

Canada

Constitutive Laws of Plastic Deformation and Fracture

by
Xijia Wu
M. Sci. and B. Sci.

A thesis submitted to
the Faculty of Graduate Studies and Research
in partial fulfillment of
the requirements for the degree of
Doctor of Philosophy

Department of Mechanical Engineering
University of Ottawa
Ottawa, Canada

UNIVERSITÉ D'OTTAWA
UNIVERSITY OF OTTAWA

Abstract

Environment assisted fatigue involves plastic deformation and degrading chemical reactions, which occur in a localized region ahead of the crack tip. Basically, transgranular crack growth proceeds by alternating slip processes. In this study, a transgranular fatigue crack growth rate model is developed on the basis of restricted slip reversibility (RSR), where transgranular fatigue crack growth rate is related to plastic deformation accommodation ahead of the crack tip (the product of the cyclic plastic strain range and the plastic zone size). The model is shown to take the form of the Paris equation with a power law exponent of 3 at positive R values.

Fatigue crack growth behavior of a 8090 aluminum-lithium alloy has been examined by a series of tests using compact tension (C(T)) specimens with the load axis a) parallel to the rolling direction (LT specimen), b) inclined at 15° (L+15°), c) inclined at 30° (L+30°), d) inclined at 45° (L+45°) to the rolling direction. It has been found that in the LT, L+15° and L+30° specimens macroscopic cracks propagate along the plane normal to the rolling direction regardless of the deviation of loading directions and the fatigue crack in the L+45° specimen propagates along the plane of specimen symmetry. Fatigue crack growth rate has been found to vary with the specimen orientation with the LT direction exhibiting the best fatigue crack growth resistance. These phenomena are discussed in terms of the crystallographic texture and the highly planar slip behavior of this alloy. A revised RSR model is developed for the description of transgranular fatigue crack growth in aluminum-lithium alloys, where the effect of texture is related to a geometric factor for the favorable slip planes.

Extension of the RSR model to environment assisted fatigue is also discussed. It is recognized that environmental effects contribute to crack propagation by the formation and rupture of an embrittlement zone in front of the crack tip. By incorporating a corrosion damage zone into the RSR model, fatigue crack growth rate in a deleterious environment is shown to be consists of two components: i) mechanical fatigue which occurs by partially reversible slip and ii) environmental enhancement of crack growth that results from the rupture of the embrittlement zone and is directly related to the characteristic dimension of this corrosion damage zone.

In addition, fracture kinetics analysis is extended to crack growth behavior which exhibits the positive-negative temperature dependence. A constitutive law is derived from the general rate equation for a two-barrier consecutive system which represents stress corrosion cracking. The transition condition of the positive-negative temperature dependence is discussed and defined in terms of microstructural characteristic quantities (activation energy and work factor) and loading constraints (stress intensity factor and temperature).

For the description of plastic deformation, a set of evolutionary rate equations is developed from deformation kinetics theory. Corresponding constitutive equations are derived for the dislocation glide mechanism, glide-plus-climb mechanism and diffusional flow. The operational equations are solved from the governing differential rate equation to determine deformation responses under different loading constraints.

Acknowledgement

The author wishes to express his deep sense of gratitude to his thesis advisor, Prof. A.S. Krausz, not only for the guidance and critical suggestions but also for teaching of the art of carrying out a research project.

Part of the work for this research was performed at the Structures and Materials Laboratory (SML) of Institute of Aerospace Research (IAR), National Research Council (NRC). The author would like to express his sincere gratitude to Dr. W. Wallace for providing the opportunity to work at SML-IAR, NRC, and for the guidance and encouragement throughout this research project. A special note of thanks goes to Dr. A.K. Koul for his supervision and constructive discussions. The author also would like to take this opportunity to thank all the staff of the laboratory, especially to M.D. Raizenne for his instructions and help in the testing and to Peter Au, Ray Dainty, Dave Chow, Dave Morphy for their technical help.

The generosity of Prof. A.S. Krausz in providing financial assistance from his NSERC grant is particularly acknowledged.

The author is also indebted to his wife, Xiaomeng, not only for her support and help in every way she could, but also for her patience during the four years to carry out this study.

Contents

Nomenclature

RSR	restricted slip reversibility
CF	corrosion fatigue
SCC	stress corrosion cracking
FCGR	fatigue crack growth rate
γ	shear strain
ε	normal strain
$\dot{\gamma}$	strain rate
$\Delta\gamma$	cyclic plastic strain range
τ	shear stress
σ	norminal tensile stress
a	crack length
da/dN	crack growth rate per cycle
K	$Y\sigma\sqrt{\pi a}$, stress intensity factor (Y is the shape factor)
K_{max}, K_{min}	maximum and minimun stress intensity factor during cycle
K_{cl}	stress intensity level for crack closure
ΔK	$K_{max} - K_{min}$, alternating stress intensity range
ΔK_{eff}	$K_{max} - K_{cl}$, the effective stress intensity range
R	K_{min}/K_{max}, stress ratio
G	K^2/E, energy release rate
K_c, K_{Ic}	stress intensities at final failure (fracture toughness)
K_{ISCC}	threshold of stress corrosion cracking
ΔK_{th}	threshold stress intensity range
J	J-integral
C^*	time-dependent J-integral
COD	crack opening displacement
CEB	normalized compliance
P	load
T	absolute temperature

Γ_s	specific surface energy
E	elastic modulus
μ	shear modulus
k	elementary rate constant
k	Boltzmann constant
$\Delta G^{\ddagger}(W)$	apparent activation energy
$\Delta G^{\ddagger}$	true activation energy
α	activation work factor
V	activation volume
l	activation distance
ν	frequency factor
τ_i	internal stress
τ_{eff}	$\tau - \tau_i$, the effective stress
H	work hardening coefficient
R^*	recovery rate
b	Burgers vector
ρ_m	mobile dislocation density
θ	angle of slip band to the width axis
ϕ	angle of slip band to the thickness axis
$\bar{\lambda}$	mean dislocation free path
σ_y	yield stress
r_p	plastic zone size
d	corrosion damage zone size
ε_c	fracture strain
ξ	$1-(1+\varepsilon_c)\Delta\gamma$, the weight function for corrosion fatigue
p	half cycle period
f	loading frequency

The subscripts

p	plasticity
f	forward
r	reverse
b	bond breaking
h	bond healing

Chapter 1

Introduction

1.1 Background

Failure of engineering components operating in various environments due to cracking is a safety and economic problem in many industries including the aerospace industry and energy industry. Time dependent plastic deformation and fracture are two of the major concerns in the design and maintenance of these engineering structures. Predictive material models (constitutive laws), as one of the necessary ingradients to predict deformation and fracture response (among other ingradients such as the equations of equilibrium and compatibility and the mathematical description of boundary conditions and loading history), are generally needed in large computer-based analysis schemes (e.g. finite element programs) which serve in manufacturing processes, product design and long-term life time prediction [1,2].

Fatigue crack growth has been the most common cause of structural failures and, therefore, is an important aspect of fracture. Despite the efforts that have been devoted to the understanding of the phenomena and mechanism of fatigue crack growth, some key problems remain unsolved and urgently need to be addressed. Among them is the establishment of physically based constitutive laws of environment assisted fatigue.

With the advent of aluminum-lithium (Al-Li) alloys as the promising materials to re-

place the conventional high strength aluminum alloys in the next generation aerospace structures, the study of fatigue crack growth behavior of Al-Li alloys has became a topic of interest in the aerospace industry. Quantitative assessment of the fatigue crack growth resistance of these alloys, through both experimental testing and deterministic physical models, needs to be done from the damage-tolerance-design standpoint.

1.2 Project Goals

The objectives of this project are as follows.

- To derive a mathematical model for transgranular fatigue crack growth from the underlying physics (the restricted slip reversibility (RSR) model) (Chapter 3).
- To do some preliminary studies for a future research project on the fatigue crack growth behavior of Al-Li alloys (chapter 4)
  - by a series of tests, to examine the fatigue crack growth rate in a 8090 Al-Li alloy as a function of the specimen orientation.
  - to study the possibility of extending the RSR model to include texture (preferred orientation) effects.
- To investigate the possibility of extending the RSR model to include time-dependent environmental effects (corrosion fatigue and hydrogen embrittlement) (Chapter 5).
- To give a fracture kinetics analysis for the cross-over behavior in stress corrosion cracking (Chapter 6).
- To derive kinetics representations for thermally activated plastic deformation mechanisms (Chapter 7).
- By doing all of these, to provide a physical framework for the future development of constitutive laws of plastic deformation and fracture.

Chapter 2

Literature Review

This chapter reviews the development of constitutive modeling for deformation and fracture in metals. The first section ("Plastic Deformation of Crystalline Materials") gives a summary of deformation mechanisms and a brief review of Ashby's deformation maps. The second section ("Environment Assisted Fatigue") provides an introduction to environment assisted fatigue crack propagation. Environment assisted fatigue is a generalized term to include fatigue in benign environments (mechanical fatigue) and in aggressive environments (corrosion fatigue); here the "aggressive environment" does not necessarily refer to the one which alone results in significant chemical attack but rather any environment which, when in conjunction with cyclic stress produces subcritical crack extension below a critical stress level determined in an inert environment. The phenomenology and mechanistic models of fatigue crack growth are summarized and critically reviewed. The third section "Deformation/Fracture Kinetics Theory" briefly reviews the key points of the deformation and fracture kinetics theory which will serve as the guidelines for the theoretical developments in later chapters.

2.1 Plastic Deformation of Crystalline Materials

Crystalline solids deform plastically by a number of independent mechanisms which are often divided into five groups [3,4]:

1. collapse at ideal strength—flow when the ideal shear strength is exceeded;
2. low-temperature plasticity by dislocation glide— limited by lattice resistance (Peierls' stress) or by discrete obstacles;
3. low-temperature plasticity by twinning;
4. dislocation creep — limited by glide-plus-climb or by glide alone;
5. diffusional flow— limited by lattice diffusion (Nabarro-Herring creep) or limited by grain boundary diffusion (Coble creep).

Time-dependent plastic deformation is controlled by the structure of the material and external constraints: temperature T, stress τ, and strain rate $\dot{\gamma}$. Ashby [3,4] developed the concept of deformation mechanism maps to represent the constitutive relation

$$\dot{\gamma} = f(\tau, T, S_i) \tag{2.1}$$

where S_i represents a set of structural variables.

The maps are divided into fields in each of which a particular deformation mechanism dominates. Superimposed on these fields are contours of constant strain rate. An example is shown in Figure 2.1. In Ashby's description, dislocation creep is represented by mechanism-based rate equations that take empirical forms such as power function or $\sinh^n$ function and therefore is named power law creep. These maps would allow one to predict the mechanism and the mode of deformation with the knowledge of applied stress and temperature, however, much empiricism they have in the form of representation and in the result of prediction. Furthermore, some important aspects of deformation such as threshold phenomena and transient behaviors are not included in Ashby's maps.

In the description of plastic deformation, an important realization was introduced by Becker [5], Eyring [6], Orowan [7,8] and Boas [9] that plastic deformation is essentially identical with chemical reactions and its description may follow chemical kinetics [10,11,12,13]. By this approach, deformation mechanisms can be related to the rate-controlling energy barrier system. Kinetics approaches relating various mechanisms with

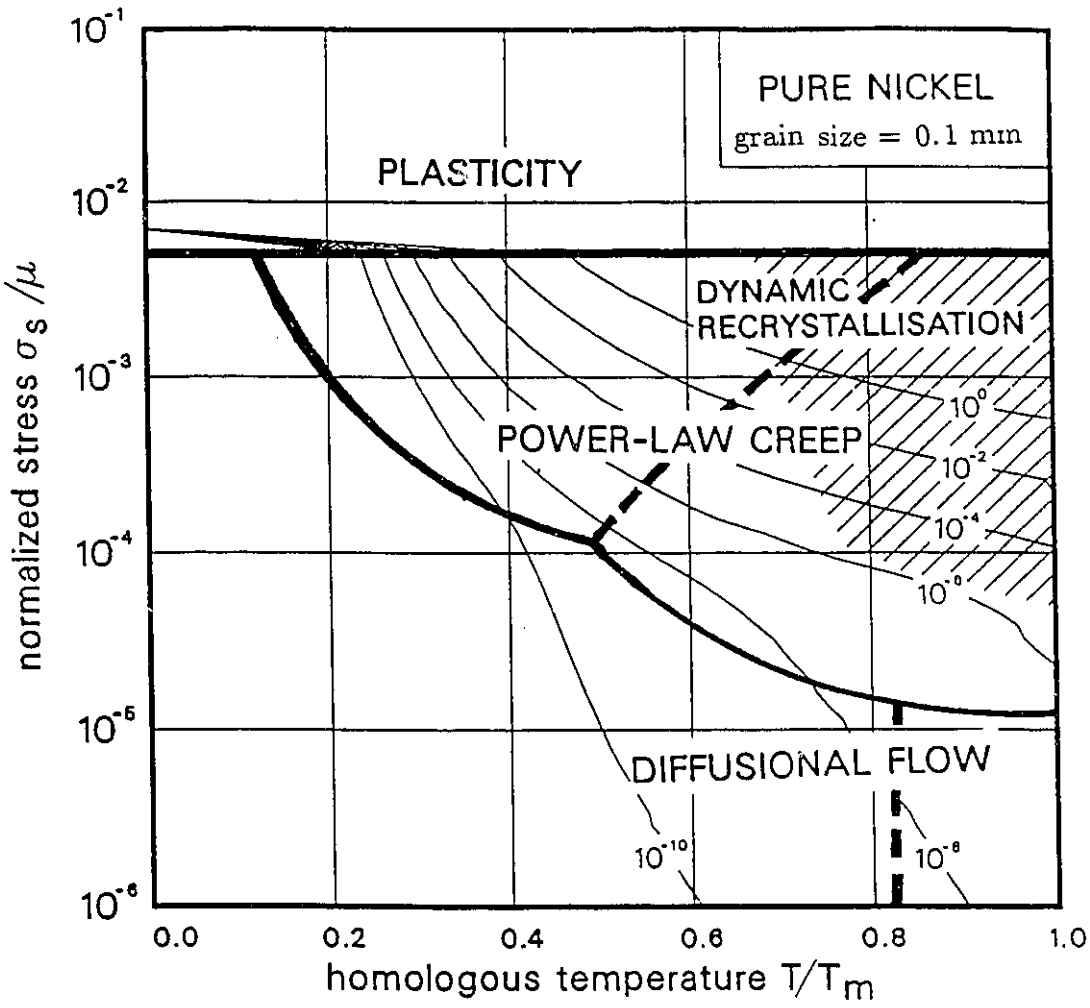

Figure 2.1. The deformation-mechanism map for pure Nickel [4].

a single energy barrier were critically reviewed by Hirth and Nix [14]; their analysis is now widely accepted. Further, it was shown by Krausz and Eyring that mechanisms of dislocation motion can be represented by multi-energy-barrier systems [15]; the theory of deformation kinetics is now well established. A further development will be in the establishment of theoretical deformation maps which should be the graphic representation of physically based constitutive laws that are rigorously derived from the first principles of physics.

2.2 Environment Assisted Fatigue

Environment assisted fatigue generally refers to the fatigue process enhanced by environmental effects. In principle, there could be as many different types of environment assisted fatigue as there are metal/environment combinations, since each will interact chemically and eletrochemically in different ways. The object of this review is to identify those common threads running through the experimental observations that enable us to deduce worthwhile generalizations and to develop constitutive laws from the fundamental physics of the deformation and crack growth processes. Such laws are indispensable for theoretical developments, for the guidance of experimental studies, and are critical for engineering design and maintenance applications.

2.2.1 Phenomenological Characterization

In the study of fatigue crack growth, an important observation was first made by Paris in the early 60's that fatigue crack growth rate (FCGR), da/dN (a is the crack length, N is the number of cycles), depends upon the range of stress intensity factor,ΔK, associated with the cyclic stress ($\Delta K = Y\Delta\sigma\sqrt{\pi a}$) [16,17]:

$$\frac{da}{dN} = C(\Delta K)^n \tag{2.2}$$

which is the well-known Paris equation. It is an empirical relation based on the experimental observation that fatigue crack growth rate under different loading configurations

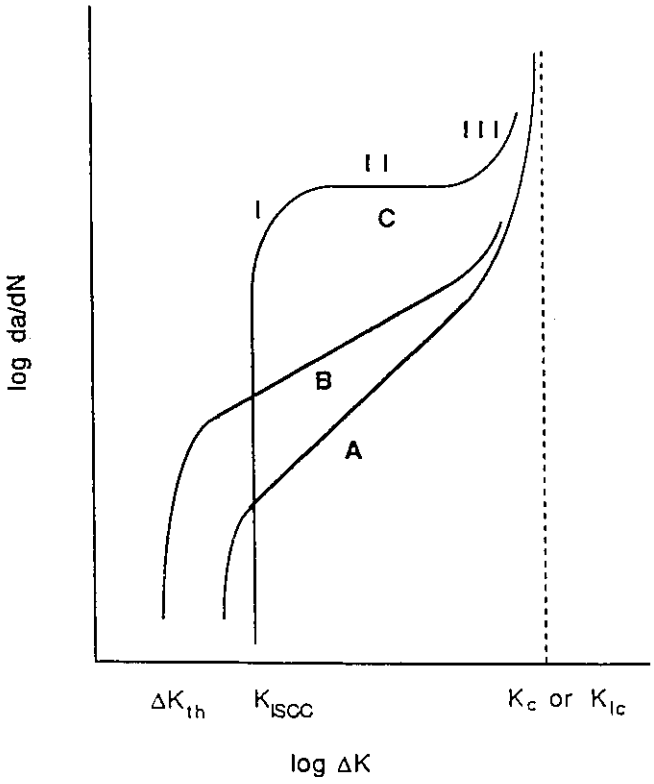

Figure 2.1. The deformation-mechanism map for pure Nickel [4].

may be uniquely represented by a straight line in the log da/dN vs logΔK coordinates. C and n are purely empirical parameters which represent the intercept and slope respectively.

Classes of Fatigue Crack Growth

For a wide range of stress intensity and with the presence of environmental effects, more complicated crack growth behavior (non-linearity in the double logarithm representation) is observed, where falls behavior largely into three typical patterns as schematically shown in Figure 2.2 [18,19].

The first type, curve A, represents fatigue in a vacuum or inert, harmless environment. This is often referred as "reference fatigue" or "mechanical fatigue", which signifies crack growth that is due to purely mechanical effects. In a wide range of ΔK, mechanical

fatigue is represented by a sigmoidal curve [20]. The intermediate range of crack growth is described by the Paris equation (1.1) and therefore is called "Paris regime". Crack growth in this regime is associated with striation formation on crack surfaces, which is evidence of alternating slip. Above the Paris regime, crack growth rate increases rapidly with ΔK and it eventually leads to catastrophic fracture as ΔK approaches K_{Ic}. Crack growth in this region is often associated with ductile dimple formation, which is a static mode of fracture and virtually depends on K_{max}. Below the Paris regime, crack growth rate vanishes asymptotically at a low ΔK value called "threshold". The threshold behavior is believed to be caused by crack closure (this will be discussed later) Various empirical or semi-empirical equations (estimated to be about 100 [21,22]) have been proposed for the representation of the sigmoidal variation in mechanical fatigue.

The second type, curve B, represents those material-environment systems in which the environmental effect results from the synergistic actions of fatigue and corrosion. This is often referred as "true corrosion fatigue" (CF). The environmental effect is evidenced by a reduction in the apparent threshold for crack growth and increases in the rate of crack growth at given ΔK levels. As ΔK approaches either K_c or K_{Ic}, the environmental influences are diminished as a result of either the rate-limiting nature of transport processes or other mechanical-chemical interactions.

The third type of behavior, curve C, typified by hydrogen-steel systems, represents those systems where there is a substantial environmentally enhanced sustained load crack growth component, which is usually referred to as stress corrosion cracking (SCC). Stress corrosion cracking typically consists of three stages of crack growth (stage I, II, III), as indicated in Figure 1.1. Above K_{ISCC}, at stage I, crack growth is strongly stress-dependent, which is then followed by stress-independent, transport/diffusion controlled crack growth, stage II; and in region III, the crack growth rate curve becomes coincident with that of mechanical fatigue.

Effects of Critical Variables

A plethora of interactive variables influence the da/dN–ΔK relationship. Among them are mechanical variables such as mean stress, frequency, waveform, and overloads; metallurgical variables including impurity, composition and microstructure (grain size, precitipate size and shape); and environment chemistry variables (viz., temperature;

gas pressure and impurity content; electrolyte pH, potential, conductivity; and halogen or sulfide ion content). Detailed analysis of each effect is beyond the purposes of this thesis, the following discussion illustrates typical effects of the more important variables.

mean stress. Increasing mean stress, as characterized by the stress ratio ($R = K_{min}/K_{max}$), generally increases the rates of fatigue crack growth, since it may include an increasingly severe static loading effect. This effect can be significant for crack growth by static mode of fracture, such as crack growth in brittle materials like polymers and ceramics, or ΔK range crack growth in high strength alloys, but insignificant or even negligible for low strength alloys and mild steels [23,24]. The R dependence of crack growth in the Paris regime and high ΔK range is often found to be described by the empirical Forman equation [25]:

$$\frac{da}{dN} = \frac{C'(\Delta K)^n}{(1-R)K_c - \Delta K}.$$

frequency. Environment assisted fatigue is a time dependent process. Therefore, the crack growth rate depends on the cyclic loading frequency (f). The general notion is that da/dN increases with decreasing frequency, because of increasing time per cycle available for increased chemical reactions and mass transport. In the limiting case where environmental effects are absent (type A), the frequency effect is diminished and fatigue crack growth is cycle dependent. In the material-environment system where K_{ISCC} is high (type B), corrosion fatigue crack growth is also largely cycle dependent [26,27,28] and is called "true corrosion fatigue". Above K_{ISCC} where stress corrosion cracking becomes a dominant mode (type C), da/dN due to environment is inversely proportional to f [26,28,29]. Figure 2.3 shows the frequency dependence behavior of fatigue crack growth in 4340M steel exposed to vacuum and water [26].

microstructure and material properties. It is believed that microstructure (grain size, precipitates, etc.) and material properties (e.g. yield strength) have significant effects on fatigue crack growth. However, the examination of these effects has been hindered by the difficulty of isolating them in experimental data since different microstructures are often associated with different yield strengths; hence their individual effects are not well understood. Although lacking a theoretical basis, Paris [17] and Speidel [26] reported that fatigue crack growth rate data of many materials tested in

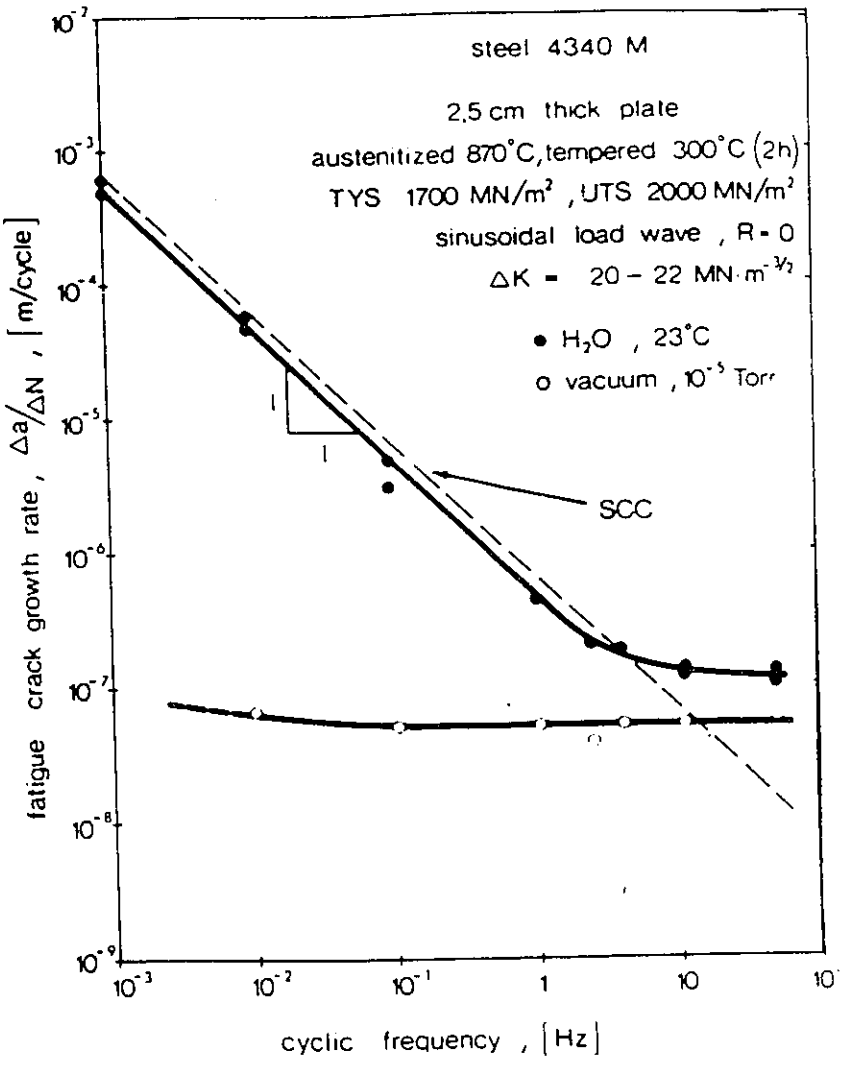

Figure 2.3. Effect of frequency on the rate of fatigue crack growth in 4340M steel exposed to vacuum and water; after Speidel [26].

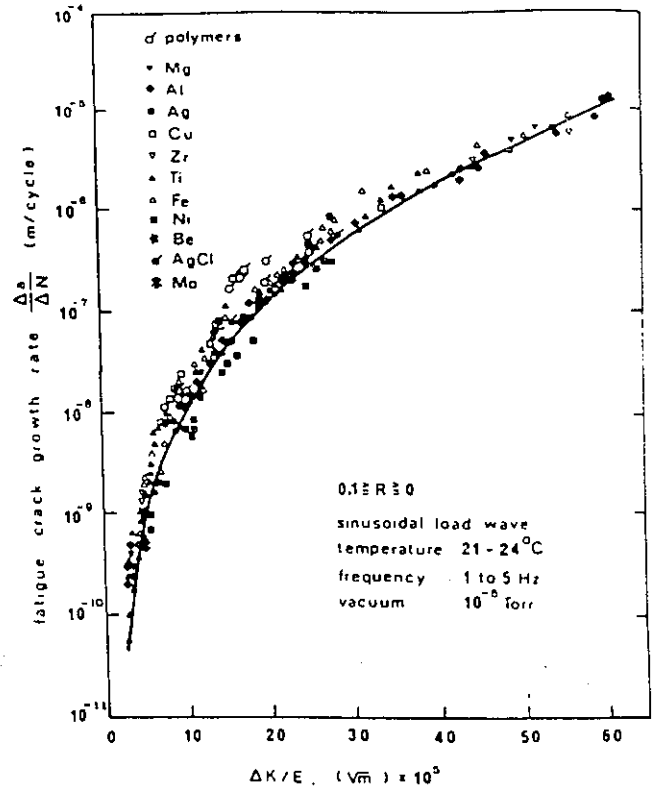

Figure 2.4. Fatigue crack growth rate as a function of modulus normalized stress intensity range; after Speidel [26].

vacuum or inert environments, when normalizing ΔK with the elastic modulus E, may be represented by one curve in the log da/dN vs $\Delta K/E$ plot [17,26], as shown in Figure 2.4 [26]. This choice of normalization was fortunate until it was applied to the aluminum alloy systems, when comparisons were made between conventional aluminum alloys and an Al-Li alloy, 2090-T8E41 [30]. The latter shows uncommonly good fatigue crack growth resistance, and this cannot be solely accounted for by the increase in elastic modulus of this Al-Li alloy, as demonstrated in Figure 2.5 [30]. Aluminum-lithium alloys contain ordered, shearable, coherent δ' (Al_3Li) precipitates and has a strong texture which is developed during mill processing. Such a microstructure increases the propensity to highly planar slip [31,32], and its role in increasing the resistance to fatigue crack growth has not been characterized quantitatively.

environment chemistry. Material-environment interactions may induce complicated mechanisms of crack growth such as film growth and rupture [33,34], slip-dissolution

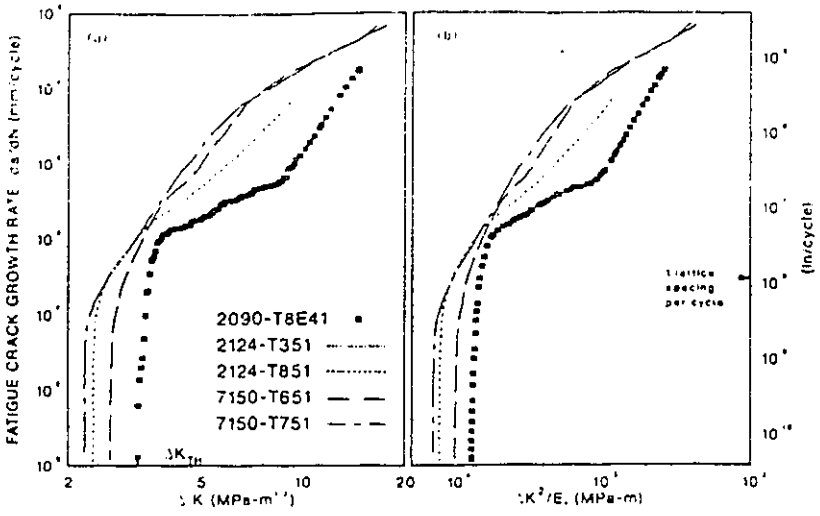

Figure 2.5. Fatigue crack growth rate as a function of (a) ΔK and (b) $\Delta K^2/E$ in aluminum alloys, after Yu and Ritchie [30].

[35,36] and hydrogen embrittlement [37,38]. Environment chemistry variables that may affect subcritical crack growth include water vapor or gas pressure; solution composition; electrode potential and pH. Understanding of these effects requires that a specific chemical variable be considered within each of the three ΔK regimes: the near-threshold region, the Paris regime and the near K_{IC} region. The scope of this study limits the author to discuss these effects in detail any further. Interested readers can see reference [28]. However, temperature is also an environmental variable, and due to its importance, the temperature dependence will be discussed in a separate paragraph.

temperature. Corrosion fatigue, being thermally activated, is by the very essence of the physical process sensitive to temperature. Usually increasing temperature increases crack growth rates. Some Arrhenius-type equations have been proposed to describe this temperature dependence [39,40,41], for example,

$$\frac{da}{dN} = B \exp\left(-\frac{\Delta G^{\ddagger}}{kT}\right) \Delta K^n$$

where $\Delta G^{\ddagger}$ is the activation energy; B and n are experimental constants. Occasionally,

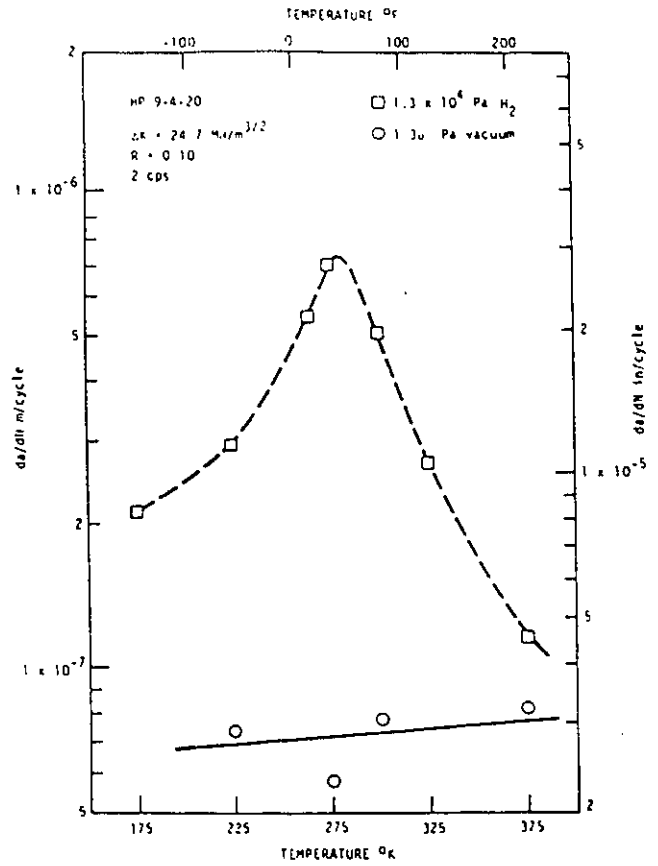

Figure 2.6. Temperature dependence fatigue crack growth in high strength HP-9-4-20 steel in vacuum (o) and gaseous hydrogen (□); after Marcus et. al. [42].

unusual crack behavior which exhibits the positive-negative temperature dependence has also been observed, as shown in Figure 2.6 [42]. It is interesting to note that mechanical fatigue exhibits less temperature dependence, as represented by the solid line in Figure 2.6. This is due to the nature of cyclic plastic deformation. High-temperature fatigue crack growth that involves creep deformation are beyond the scope of this project and its discussion is not included here. Interested readers can see reference [43].

crack closure. Crack closure, first observed by Elber [44], has received a great deal of attention [45,46,47,48,49,50,51] because it plays an important role in the threshold of fatigue crack growth. It was suspected by Beevers that the threshold in corrosion fatigue may occur partly as an intrinsic property of the material-environment system and partly as the result of crack face interferences [46]. The mechanisms of crack face interference are usually classified into a) plasticity-induced crack closure which is caused by the elastic constraint of material surrounding the plastic zone enclave

in the wake of the crack tip, on material elements previously plastically stretched at the tip [44]; and b) roughness-induced crack closure which is caused by the wedging actions arised from the misfitting of surface roughness; and c) oxide-induced crack closure caused by corrosion debris on the fracture surfaces [45,48]. All these closure actions may play a role in reducing the effective stress intensity range experienced by the crack tip. Two rate-dependent closure mechanisms, thermodynamic bond healing and work-promoted closure, were also suggested by Krausz [19,50,51], based on the reaction rate concept. In both of these two processes, the crack re-heals by the re-establishment of atomic bonds that have been broken along the crack front during crack propagation; the thermodynamic healing occurs against mechanical work, while the work-promoted closure is promoted by the residual stress on the contacting crack surfaces during unloading.

2.2.2 Modeling of Fatigue Crack Growth

Early crack propagation models (1960-1980) were largely developed on the basis of continuum mechanics principles in which the analysis of crack-tip plasticity was coupled with critical damage criteria to formulate crack growth rate equations [52]-[55]. These damage criteria were defined in terms of either accumulated plastic work (hysteresis energy), accumulated plastic deformation (fracture strain) or balance of total energy input into the system. A plastic blunting model was also proposed [56,57] in which crack growth rate was related to the crack tip opening displacement by taking account of the effect of geometrical factors ahead of the crack tip. None of these models was developed on the basis of the underlying physics of the deformation and fracture processes.

The kinetics approach was initially developed in the 1970s for the study of stress corrosion cracking, which was based on linear fracture mechanics and was predicated on the recognition that environmentally assisted cracking is the result of sequential rate-controlling steps (transport, surface reactions, diffusion, embrittlement, bond breaking etc.) and is limited by the slowest step in this sequence [37,38,58,59,60,61,62]. Particularly, atomistic crack growth models were developed by Krausz and Krausz [19], recognizing that crack growth involves atomic bond breaking and bond healing along the crack front. The fracture kinetics analysis was also extended to corrosion fatigue by Krausz and co-workers [50,51,63]-[67] based on the bond breaking-healing kinetics.

For general environment assisted fatigue, a linear superposition model was proposed by Wei [68] in which the crack growth rate in a deleterious environment, $(da/dN)_e$, was decomposed into two components: mechanical fatigue, $(da/dN)_m$, and corrosion fatigue, $(da/dN)_c$, each weighted by a fractional parameter; i.e.,

$$\left(\frac{da}{dN}\right)_e = \left(\frac{da}{dN}\right)_m \theta + \left(\frac{da}{dN}\right)_c \phi \tag{2.3}$$

where θ is the fraction of the crack surface formed by mechanical fatigue and ϕ is the fraction of the crack surface formed by corrosion fatigue. Equation (2.3) is only qualitative since the fractional parameters, θ and ϕ are not given quantitatively and the description of mechanical fatigue remains empirical.

2.3 Deformation/Fracture Kinetics Theory

Atoms in condensed phases occupy equilibrium positions and are vibrating about the minimum of the free energy well. Under the combined effect of mechanical forces and thermal vibrations, any atom will move into a new equilibrium valley while breaking the previous bonds and establishing new bonds.

2.3.1 Deformation and Crack Growth Processes

Crystalline materials contain lattice defects such as dislocations, voids, solute atoms, precipitate particles and grain boundaries etc.. These atomic disorders possess higher energy than the ordinary atoms. Therefore, the breaking and rearrangement of atomic bonds are likely to occur by thermal activation at such defect sites, which will result in plastic deformation and crack growth.

Dislocation Motion

The bond breaking process in crystalline materials at low temperature occurs with high probability at line defects–the dislocations. It was already recognized that thermal

fluctuation can facilitate the displacement of dislocations in the direction favored by the shear stress. The effect of an applied stress on the potential energy along a dislocation slip plane is shown in Figure 2.7 [70]. The gliding of many dislocations results in slip, which is the most common manifestation of plastic deformation. This mode of deformation can be depicted by Polanyi's salami [71] as shown in Figure 2.8. The plastic strain rate, $\dot{\gamma}_p$, is given by the Orowan equation [72] as

$$\dot{\gamma}_p = b\rho_m v \tag{2.4}$$

where b is the Burgers vector, ρ_m is the mobile dislocation density and v is the mean dislocation velocity.

Crack Growth Processes

The concept of crack growth was initiated by A.A. Griffith in the 1920's [73,74]. His argument was based on energy considerations: crack growth is accompanied by the formation of new surfaces and the strain energy released from crack propagation should be equal to the newly-formed surface energy.

Since the total energy change ΔU, due to the formation of a crack of length $2a$, is the sum of the elastic stain energy change ($\Delta U_e = -(\pi\sigma^2 a^2)/E$) and the surface energy change ($\Delta U_s = 4\Gamma_s a$):

$$\begin{aligned} \Delta U &= \Delta U_e + \Delta U_s \\ &= -\frac{\pi\sigma^2 a^2}{E} + 4\Gamma_s a \end{aligned}$$

where Γ_s is the specific surface energy, the equilibrium condition is defined by:

$$\frac{d}{da}\left(-\frac{\pi\sigma^2 a^2}{E} + 4\Gamma_s a\right) = 0$$

which leads to

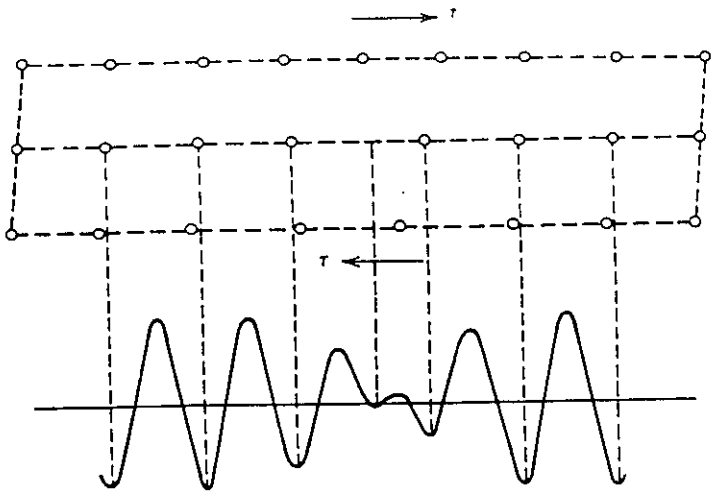

Figure 2.7. The effect of a shear stress on the potential energy along a dislocation slip plane; after Taylor [70].

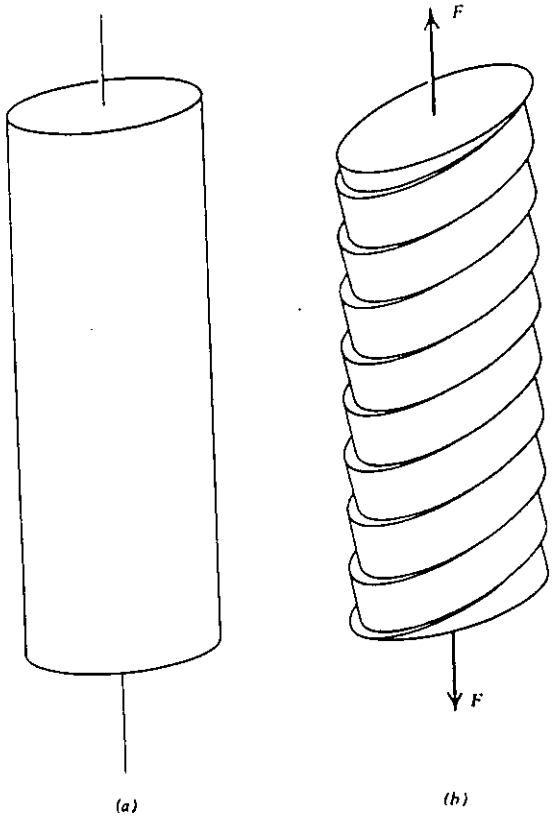

Figure 2.8. The deformation of Zn single crystal in tension. (a) illustrates the specimen before and (b), during tensile test [71].

$$G = 2\Gamma_s \tag{2.5}$$

where $G = (\pi\sigma^2 a)/E$ is the strain energy release rate.

Equation (2.5) lays the foundation of modern fracture mechanics. It sets a critical criterion for crack growth: either crack growth occurs catastrophically (when $G > 2\Gamma_s$) or crack growth does not occur at all (when $G < 2\Gamma_s$).

Extending the Griffith's concept, Krausz and Krausz [19] further considered that a subcritical crack may grow by thermally activated atomic bond breaking along the crack front, as illustrated in Figure 2.9. At some instant of time, the crack front is defined by the solid line linking atoms on the crack surface. Atoms at some distance from the crack tip vibrate about their equilibrium positions; near the crack tip the atoms are displaced from equilibrium by mechanical work. Due to thermal vibration, the interatomic distance between the pair of atoms just ahead of the crack tip fluctuates, as shown by the cross-hatched cycles in Figure 2.9. As changes in amplitude sweep through the solid with a wavelike motion, at some instant a crest will arrive that is large enough to separate the atoms to the extent that the "spring", or atomic interaction, breaks. Then, crack advances a few atomic distances. Occasionally, also due to thermal vibration, some previously broken bonds may be re-established between the pair of atoms to partially close the crack. The crack growth rate is thus controlled by net activation rate k times the activation distance na_0 (n is the number of activated atoms and a_0 is the interatomic distance):

$$\frac{da}{dt} = na_0 k \tag{2.6}$$

The above crack growth model depicts the "opening mode" crack growth, i.e. crack extension by bond breaking along the main crack plane. In mechanical fatigue processes, alternating slip may produce partially reversible slip steps that lead to crack extension. The role of alternating slip in inducing fatigue damage (crack initiation and propagation) was first noted by E. Orowan [75]. He assumed that crack initiation occurs by alternating microscopic slips. In his description,

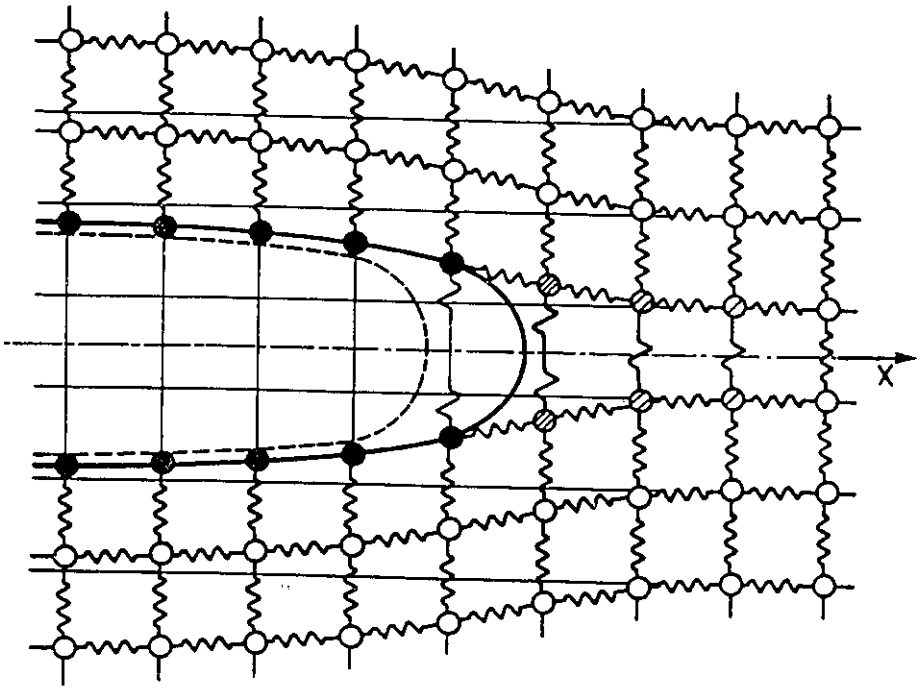

Figure 2.9. Schematic representation of crack-tip region [19]. The model allows the vibrational motion of atoms. Springs indicate that atoms are interacting; missing springs indicate loss of interaction – broken bonds. The region without 'springs' is equivalent to the free surface – that is, the crack surface – and is shown by the heavy line.

> the slipping "surfaces" become increasingly abraded in the course of the alternating straining, and their cohesion diminishes until finally a crack appears.

This recognition was verified overwhelmingly by later experiments [76]-[82]. Laird and Smith [79] and Newmann [80] even made direct observations of crack opening profile and related crack propagation to the crack tip opening by alternating slip. The concept was further extended by Fong [83,84] to the restricted slip reversibility (RSR) model. The description of this "shear mode" crack growth was not included in the original fracture kinetics theory [19]. As a distinguished mode of crack growth, the restricted slip reversibility must be recognized here.

2.3.2 Deformation/Fracture Kinetics

Plastic deformation and crack growth, as well as chemical reaction, are essentially identical processes in the sense that, in the microscopic scale, they are all the result of the breaking and re-establishment of atomic bonds which occur by thermal activation. The rearrangement of atomic configuration takes place either by replacing one (or more) atoms with a different kind (e.g. chemical reactions, diffusion) or by changing "neighbors" in plastic deformation or by separation of "neighbors" in crack initiation and growth. It follows from the axioms of statistical mechanics that all thermally activated processes proceed by the dual occurrences of forward and reverse steps [10]-[13]. In chemical reactions this is recognized as the dual activity of reactant-to-product and product-to-reactant reactions. In diffusion and in dislocation glide it is conventional to label them as "forward" and "backward" steps, the first being the one that promotes the macroscopically observed direction of plastic deformation while the second is in the opposite direction. Crack growth is also recognized as the concurrent processes of bond breaking and bond healing [19]. The threshold represents the set of stress conditions where forward and reverse activation are in equilibrium [13].

For all thermally activated processes the rate of each activation step is rigorously described by the elementary rate constant expressed as (Appendix A):

$$\mathsf{k} = \nu \exp\left(-\frac{\Delta G^{\ddagger}(W)}{kT}\right) \tag{2.7}$$

where $k = 1.38 \times 10^{-23}\mathrm{JK}^{-1}$ is the Boltzmann constant; T is the absolute temperature; ν is the pre-exponential frequency factor defined by the absolute rate theory; $\Delta G^{\ddagger}(W)$ is the apparent activation energy (average thermal energy).

The apparent activation energy is defined by the energy condition necessary to rearrange atoms into the configuration that exist after one activation step. For forward activation steps it is defined as

$$\Delta G_f^{\ddagger}(W) = \Delta G_f^{\ddagger} - W_f, \tag{2.8}$$

where $\Delta G_f^{\ddagger}$ is the true activation energy for forward activation and W_f is the mechanical work input by the applied force system; and for reverse activation steps as

$$\Delta G_r^{\ddagger}(W) = \Delta G_r^{\ddagger} + W_r, \tag{2.9}$$

where $\Delta G_r^{\ddagger}$ is the true activation energy for reverse activation and W_r is the mechanical work to be overcome for reverse activation to occur.

Generally, thermally activated deformation and crack growth processes consists of diverse activation steps, and therefore can be represented by various combinations of rate constants. Deformation/fracture kinetics recognize three basic kinetic systems (i) single energy barrier; (ii) parallel barrier system; and (iii) consecutive barrier system. More complicated systems can be represented by the combination of the above three.

Single Energy-Barrier

The simplest kinetics represent the activation event controlled by a single energy barrier, as shown in Figure 2.10. The forward activation rate is defined by k_f and the reverse rate is defined by k_r. Such forward-reverse twin processes are recognized, for instance, in diffusion as forward-backward diffusion, in crack growth as atomic bond breaking-healing, in fatigue as forward slip-slip reversal. The overall rate, v, is the result of the

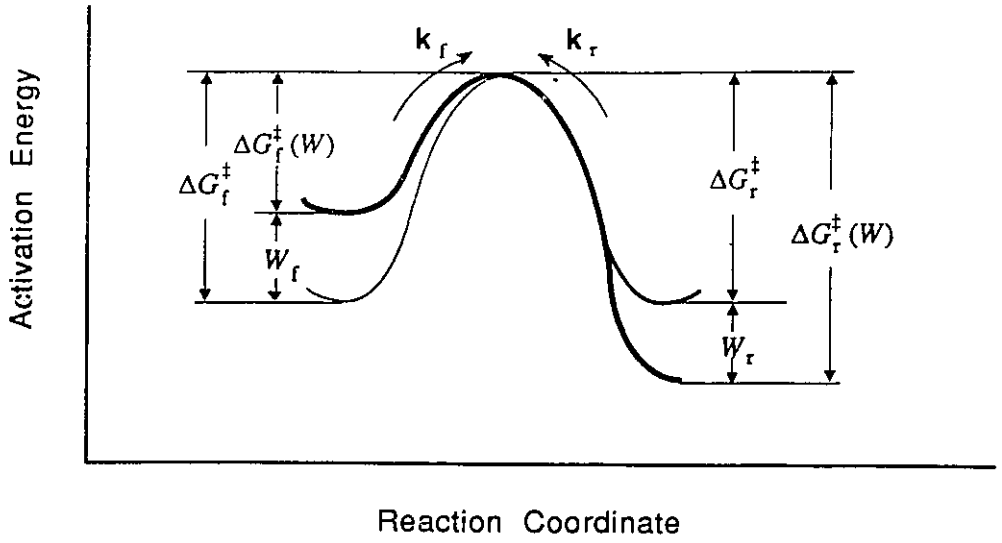

Figure 2.10. Single-energy-barrier kinetics: k_f represents the forward activation rate; k_r represents the reverse activation rate.

competition between forward and reverse steps [15,19]:

$$v = (l)(k_f - k_r) \tag{2.10}$$

where l is the activation distance.

In application to deformation processes, expressing $W = V\tau$ (V is the activation volume, τ is effective stress), equation (2.10) can be written as [15]

$$v = l_f \nu \exp\left(-\frac{\Delta G_f^{\ddagger} - V_r \tau}{kT}\right) - l_r \nu \exp\left(-\frac{\Delta G_r^{\ddagger} + V_r \tau}{kT}\right). \tag{2.11}$$

Equation (2.11) was found to describe well the dislocation velocity in many crystalline materials [15].

In application to crack growth, following equation (2.6) and expressing $W = \alpha K$ (α is the work factor, K is stress intensity factor), the crack growth rate can be expressed as

$$v = l_b \nu \exp\left(-\frac{\Delta G_b^{\ddagger} - \alpha_b K}{kT}\right) - l_h \nu \exp\left(-\frac{\Delta G_h^{\ddagger} + \alpha_h K}{kT}\right). \tag{2.12}$$

Here, the subscripts "b" and "h" signify bond breaking and healing respectively. Equation (2.12) was found to describe well the stress corrosion cracking of a variety of ceramics and glass materials exposed to various environments [19]. Sometimes, the energy release rate G was also used to formulate the work dependence of crack growth processes [19,40]. Under cyclic loading with triangular wave form it was shown by Krausz and co-workers that corrosion crack growth rate, da/dN, can be obtained by integration of equation (2.12) over one load cycle as [50]:

$$\begin{aligned}\frac{da}{dN} &= \frac{\delta_b kT \mathsf{k}_b^{\ddagger}}{2f\alpha_b \Delta K}\left\{\exp\left[\frac{\alpha_b \Delta K}{kT(1-R)}\right] - \exp\left[\frac{\alpha_b R \Delta K}{kT(1-R)}\right]\right\} \\ &\quad \mp \frac{\delta_h kT \mathsf{k}_h^{\ddagger}}{2f\alpha_h \Delta K}\left\{\exp\left[\pm\frac{\alpha_h \Delta K}{kT(1-R)}\right] - \exp\left[\pm\frac{\alpha_h R \Delta K}{kT(1-R)}\right]\right\}\end{aligned} \tag{2.13}$$

where δ is the activation distance and $\mathsf{k}^{\ddagger}$ is defined as the rate constant at zero stress intensity. The $\pm$ sign indicate that two healing mechanisms—thermodynamic and closure type—may operate in the case of corrosion fatigue.

Parallel Energy-Barrier System

When several independent steps occur concurrently to promote deformation or crack growth, that is, when activations proceed along different paths on the potential surface, the process can be represented by a parallel energy-barrier system. In such an event, each activation proceeds independently and makes its individual contribution to the overall rate. Therefore, the process is controlled by the fastest step. For a parallel system with two energy barriers, Figure 2.11, the rate equation is expressed as:

$$v = l_1(\mathsf{k}_f - \mathsf{k}_r)_1 + l_2(\mathsf{k}_f - \mathsf{k}_r)_2 \tag{2.14}$$

Consecutive Energy-Barrier System

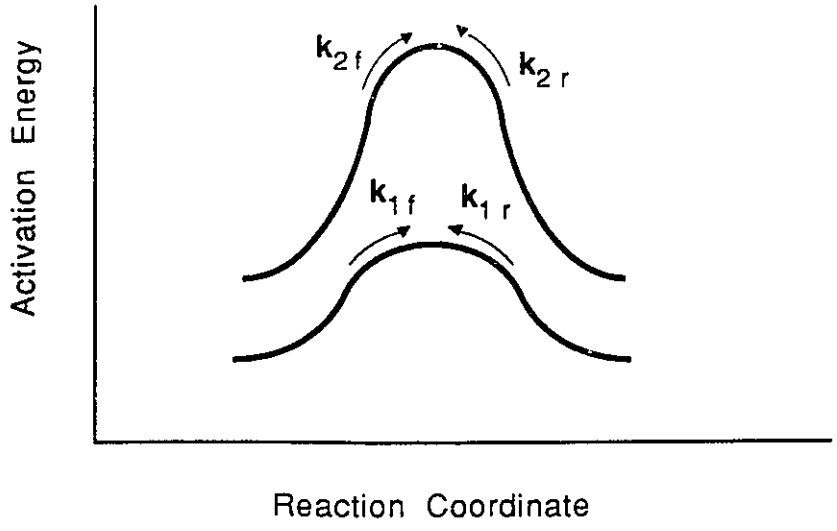

Figure 2.11. Kinetics of two energy-barriers in parallel.

When a deformation or crack growth process occurs as the result of several sequential steps, that is, the overall activation consists of a series of dependent steps, the process can be represented by a consecutive energy-barrier system. In such a system, the continuation of any step depends on the outcome of the previous step. Therefore, the overall process is limited by the slowest step in the sequence. The rate equation for a consecutive system with two energy barriers (Figure 2.12) takes the form [15,19]:

$$v = (l)\frac{k_{If}k_{IIf} - k_{Ir}k_{IIr}}{k_{If} + k_{IIf} + k_{Ir} + k_{IIr}}. \tag{2.15}$$

Equation (2.15) was found to describe well stress corrosion cracking processes [19,61].

2.3.3 Work Dependence

As shown above, the rate of a thermally activated process is controlled by the apparent activation energy, its content depends on the mechanical work input which is a function

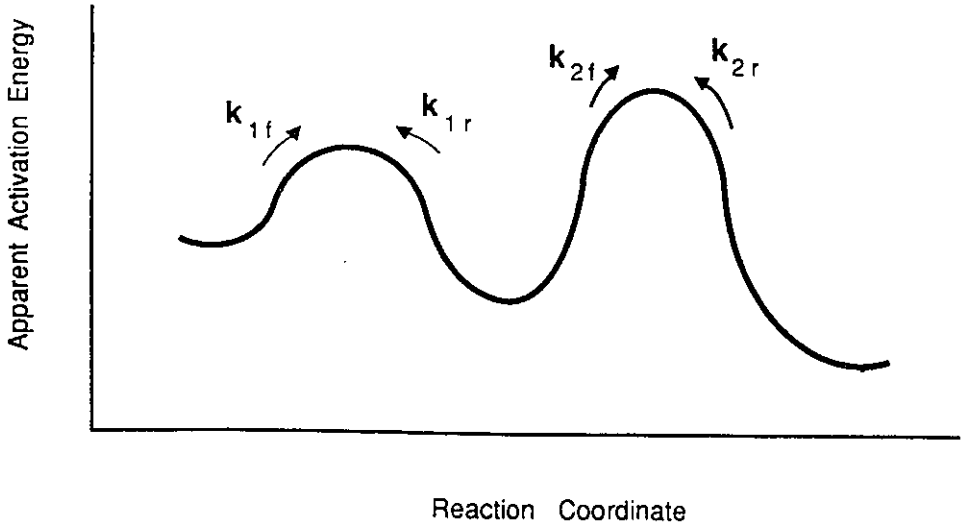

Figure 2.12. Kinetics of two energy-barriers in sequence.

of stress. The true stress dependence of activation energy is often not known from basic physics, because even the construction of one theoretical potential surface is a formidable task for a real deformation/crack growth process that involves the motion of millions of atoms. However, the activation energy, $\Delta G^{\ddagger}(W)$, can be measured experimentally. For example, for a single-rate-constant controlled deformation process the rate equation takes the form (Arrhenius equation)

$$\dot{\gamma} = \dot{\gamma}_0 \exp\left(-\frac{\Delta G^{\ddagger}(W)}{kT}\right), \tag{2.16}$$

and the apparent activation energy can be determined as follows:

$$\Delta G^{\ddagger}(W) = -k\frac{\partial \ln \dot{\gamma}}{\partial(1/T)}|_{\tau}. \tag{2.17}$$

For processes that are represented by combinations of rate constants, the evaluation of $\Delta G^{\ddagger}(W)$ can be done by a step-by-step procedure as illustrated in references [15,19].

Once the relation of $\Delta G^{\ddagger}(W)$ vs τ is determined, the stress dependence of the process is also determined. This is a standard, well-established procedure of kinetics analysis for chemical reactions, plastic deformation as well as crack growth. Of course, the so-obtained relationship can only be valid for the particular mechanism under consideration. As a single mechanism may be rate controlling only over limited stress and temperature ranges, the associated activation parameters cannot be measured outside this regime. Within it, the stress dependence of the activation energy may be linearized:

$$\Delta G^{\ddagger}(\tau) = \Delta G^{\ddagger}(\tau_0) + (\tau - \tau_0)\frac{\partial \Delta G^{\ddagger}}{\partial \tau}|_{\tau_0} + ..., \tag{2.18}$$

where τ_0 is a constant, reference, stress within the range. Defining the activation volume V as

$$V = -\frac{\partial \Delta G^{\ddagger}}{\partial \tau}|_{\tau_0}$$

and writing

$$\Delta G_0^{\ddagger} = \Delta G^{\ddagger}(\tau_0) + V\tau_0,$$

equation (2.18) becomes

$$\Delta G^{\ddagger}(\tau) = \Delta G_0^{\ddagger} - V\tau \tag{2.19}$$

The activation energy $\Delta G_0^{\ddagger}$ may be different from the activation energy at zero stress, $\Delta G^{\ddagger}$; it is, however, the only value experimentally determinable, unless the true stress dependence of the activation energy is known *a priori*. Nevertheless, the stress dependence relation (2.19) has been widely used in the kinetics description of plastic deformation [15]. Alefeld [85] showed that even with constant activation volume equation (2.16) could describe adequately some experimental results.

In fracture kinetics, the work dependence is often expressed as a function of the controlling fracture quantity such as stress intensity factor K, energy release rate G, or J-integral or C^* [19]:

$$W = g(K, \text{ or } \mathsf{G}, \text{ or } J, \text{ or } C^*).$$

The stress intensity factor K is defined as a stress function that characterizes the intensity of the elastic near-tip stress field, while G, J and C^* are stress functions defined by energy considerations. The J-integral and C^* are often related to large scale yielding condition and time dependent creep fracture respectively, which are beyond the scope of this study and will not be discussed further.

Activation energy dependence on K or G implies that either the stress or the energy release is the driving force of crack growth. Within the constraints of linear elastic fracture mechanics (LEFM), both concepts may apply [19,40]. It is customary to express the work as the linear function of stress intensity factor K or the energy release rate G [19]. The exact and physically approved expression for the fracture work, W, is still needed.

2.3.4 Internal Stress

Lattice distortion due to the presence of defects represents an internal stress field within the solid. Only the effective stress which is the difference between the applied stress, τ, and the internal stress, τ_i, does work when a dislocation surmounts an obstacle by thermal activation, i.e. [15],

$$W(\tau) = V\tau_{eff} = V(\tau - \tau_i) \tag{2.20}$$

Equation (2.20) suggests that at zero effective stress, the activation work is zero and, therefore, the plastic strain rate must be zero. This principle renders the measurement of internal stress by stress relaxation tests [15]. Figure 2.13 illustrates the method of hunting for the internal stress in the combined positive and negative stress relaxation test.

Generally, the internal stress τ_i depends on the work hardening rate and recovery rate

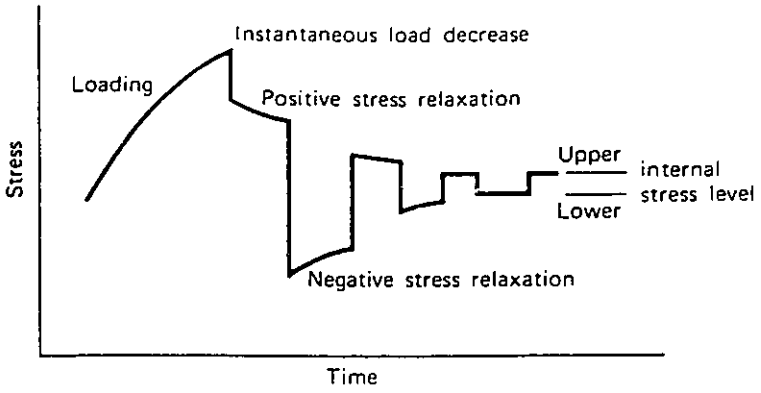

Figure 2.13. Schematic representation of the testing procedure used in the positive-negative stress relaxation method of internal stress measurement [15].

of the material. Following the Bailey-Orowan equation [137,138], it can be expressed as

$$\frac{d\tau_i}{dt} = H\dot{\gamma} - R^*(\tau, \tau_i, T, t) \tag{2.21}$$

where H is the work hardening coefficient and R^* the recovery rate. This concept has been used extensively in the constitutive modelling of plastic deformation [88,89].

The role of internal stress in fracture processes has been addressed by Krausz and Krausz [19], but the analysis has not been applied to particular crack growth processes.

2.3.5 Comments

Deformation/fracture kinetics, together with rate theory, constitute the physical framework for the building of constitutive models. The theory is coherent with the description of transport/diffusion and chemical reactions. Thermally activated processes are controlled by the atomic-level energy content, $\Delta G^{\ddagger}(W)$. This common aspect of atomic bond breaking, dislocation motion, diffusion and chemical reactions is the essence of

plastic deformation and environment assisted fracture. In modeling of a deformation/crack growth process, the rate controlling steps have to be identified from the underlying physical mechanism. For fatigue crack growth in metals, the restricted slip reversal is an indispensable part of the mechanism. Fracture kinetics description should be extended to this distinct mode of fatigue crack growth.

Chapter 3

Transgranular Fatigue Crack Growth in Metals

3.1 Restricted Slip Reversibility (RSR)

Slip occurs as a result of dislocation motion (glide), which is a thermally activated process. It proceeds by the dual occurrences of forward and reverse activation steps over a single rate-controlling energy barrier where the barrier arises as a result of lattice resistance or defect obstacles [4,15].

The role of alternating slip processes in inducing fatigue damage (crack initiation and propagation) has long been recognized [76]-[78]. Particularly, the slip reversal has been found to be responsible for sharpening the vertex of the crack [80]. The forward slip and slip reversal processes also lead to the formation of striations during fatigue crack propagation. This concept is consistent with experimental observations and explains many essential features of fatigue fracture [80,81,82]. These considerations were extended by Fong [83,84] to a restricted slip reversibility (RSR) model for depicting the events at a propagating crack tip, as shown schematically in Figure 3.1. The model explains transgranular crack propagation events as follows.

(i) Upon loading, slip systems on two favorably oriented parallel slip planes S1 and S2

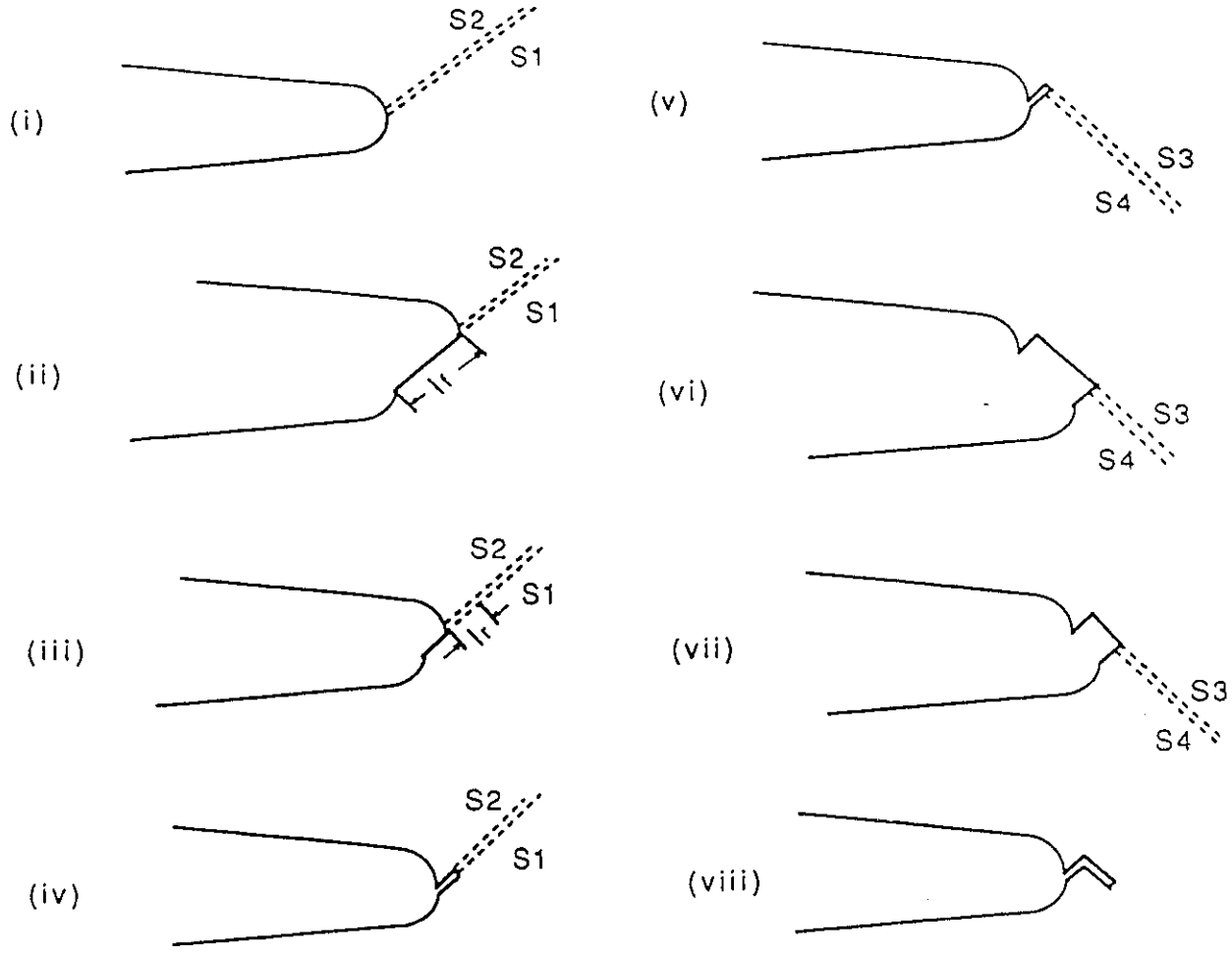

Figure 3.1. Schematic diagram of fatigue crack growth by restricted slip reversibility (RSR) [83].

are activated. (ii) Forward slip occurs predominantly on S1 during the rising load cycle, producing a slip step of length l_f. (iii) During the decreasing load cycle, an increment of slip reversal l_r occurs on S1. (iv)A final slip reversal occurs on S2, producing a sharp crack tip. This process may be repeated over several or many load cycles (N) to produce a final crack length (a) increment, after which a similar process may occur on another (conjugate) favorably oriented slip system variant along another pair of parallel slip planes, S3 and S4, as shown in the schematics (v) to (viii) of Figure 3.1.

3.2 The Proposed Crack Propagation Model

In a deforming crystalline material, plastic deformation accumulates by crystallographic slip that occurs in local stress concentration regions. Figure 3.2 (a) illustrates the situation of crack initiation at a slip offset location. In the case of a growing crack, it is well established that plastic strain accumulates in the form of a plastic zone ahead of the crack tip and the slip activity is limited to this plastic zone. Figure 3.2 (b) shows a schematic of slip activity in the plastic zone in conformity with the RSR model for crack growth. According to the RSR model (Figure 3.1), the fatigue crack growth rate can be expressed as [90]:

$$\frac{da}{dN} = (l_f - l_r)\cos\theta, \tag{3.1}$$

where θ represents the favorably oriented slip direction within the plastic zone in Figure 3.2 (b).

Each slip step occurs by dislocation glide with the slip step length l equal to the total dislocation glide distance, and this distance is given by:

$$l = n\bar{\lambda}, \tag{3.2}$$

where $\bar{\lambda}$ is the average distance moved by individual dislocation and n is the number of mobile dislocations on the favorably oriented slip plane. The number n can be counted

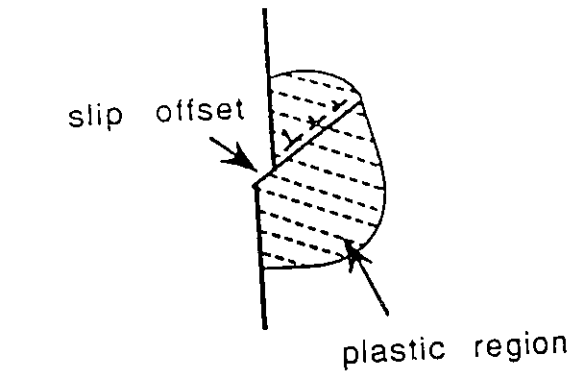

(a)

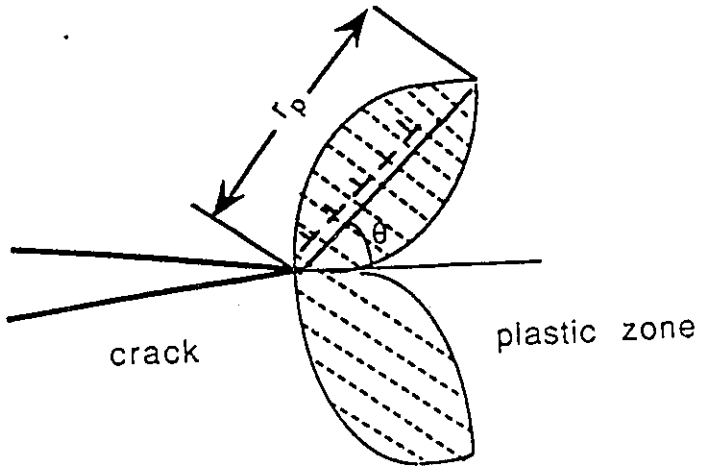

(b)

Figure 3.2. (a) Crack initiation at a slip offset location; (b) Schematic of slip activity in the case of fatigue crack propagation.

by multiplying the mobile dislocation density (the number of mobile dislocations per unit area), rho, with Burgers vector, b, and the plastic zone size, r_p, as

$$n = b\rho r_p, \tag{3.3}$$

Substituting (3.2) and (3.3) into (3.1):

$$\frac{da}{dN} = b(\rho_f \bar{\lambda}_f - \rho_r \bar{\lambda}_r) r_p \cos\theta. \tag{3.4}$$

Here and in the following text, the subscripts "f" and "r" signifies the physical quantities for forward slip and slip reversal respectively.

The mean dislocation free path components in equation (3.4) can be translated into shear strain (γ) components associated with forward slip (γ_f) and slip reverseal (γ_r) by using Orowan's [72] equation:

$$\gamma = b\rho\bar{\lambda}$$

Equation (3.4) can therefore be written in the form:

$$\frac{da}{dN} = (\gamma_f - \gamma_r) r_p \cos\theta. \tag{3.5}$$

Equation (3.5) expresses fatigue response of a growing crack in terms of the net strain ahead of the crack tip. This equation agrees in principle with Laird and Smith's [79] early conclusion that plastic deformation is responsible for crack propagation in ductile metals. When dealing with crack initiation, r_p represents the size of a localized yield zone. In the case of fatigue crack growth under small scale yielding condition, from the analysis of linear fracture mechanics [91]:

$$r_x = r_p \cos\theta = \frac{1}{3\pi}\left(\frac{\Delta K}{2\sigma_y}\right)^2. \tag{3.6}$$

Upon substituting for $r_p \cos\theta$ in equation (3.5), crack growth rate can be expressed by:

$$\frac{da}{dN} = \frac{1}{12\pi}(\gamma_f - \gamma_r)\left(\frac{\Delta K}{\sigma_y}\right)^2 \tag{3.7}$$

The description of plastic deformation at the crack tip follows the theory of deformation kinetics and in the case of dislocation-glide mechanism, shear strain rate, $\dot{\gamma}$, can be expressed as [4,15]:

$$\dot{\gamma} = \dot{\gamma}_o \exp\left(-\frac{\Delta G^{\ddagger} - V\tau_{eff}}{kT}\right) \tag{3.8}$$

where $\dot{\gamma}_o$ is a pre-exponential factor, $\Delta G^{\ddagger}$ is the activation energy, V is the activation volume. τ_{eff} is the effective stress experienced by the dislocation at the activation sites, and τ_{eff} is the difference between the applied stress and the internal stress. The internal stress in turn depends on the material properties such as work hardening and softening rate and can be expressed as a complex function of stress, strain, temperature and time. For simplicity, a linear strain-hardening rule is used to express the effective stress [15,92]:

$$\tau_{eff} = \tau - H\gamma - \tau_o,$$

where τ is the applied stress, H is the strain hardening coefficient, γ is the plastic shear strain, and τ_o is the initial internal stress.

Substituting the expression of effective stress into equation (3.8),

$$\dot{\gamma} = \dot{\gamma}_o \exp\left[-\frac{\Delta G^{\ddagger} - (V\tau - VH\gamma - V\tau_o)}{kT}\right]. \tag{3.9}$$

According to linear elastic fracture mechanics, the shear stress at the crack tip along the θ direction is expressed as (Appendix B)

$$\tau = \frac{K}{2\sqrt{2\pi r}} \sin\theta \cos\frac{\theta}{2}.$$

where r is the distance from the crack tip.

The average plastic strain rate within the plastic zone can be computed through the summation of local strain rate $\dot{\gamma}(r,\theta)$ over the length of plastic zone along the crystallographic direction θ:

$$(\dot{\gamma})_{\text{average}} = \frac{1}{r_p}\int_b^{r_p} \dot{\gamma}(r,\theta)dr$$

Upon using the mean value theorem for integrals [93] and equation (3.9), the average plastic strain rate can be represented by

$$\dot{\gamma} = \dot{\gamma}_o \exp\left[-\frac{\Delta G^{\ddagger} - (\alpha K - VH\gamma - V\tau_o)}{kT}\right] \tag{3.10}$$

where

$$\alpha = \frac{V}{2\sqrt{2\pi L}}\sin\theta\cos\frac{\theta}{2}$$

is the work factor and L is the characteristic length of activated distance defined by the mean-value theorem. Since the stress decreases rapidly away from the crack tip, the plastic strain rate is mainly influenced by thermally activated glide that occurs with a short distance of the crack tip. The parameter L depends largely on the microstructure and defect density near the crack tip and is less relevant to the actual length of the entire plastic zone over which the average is taken. Therefore, α can be considered as a material constant which is independent of the plastic zone size and the stress intensity factor.

It will be recognized that forward slip occurs during rising load in a fatigue cycle and slip reversal occurs during the decreasing part of the load cycle. The mechanisms controlling the forward slip and slip reversal processes are the same in mechanical fatigue, but these mechanisms will be different in corrosion fatigue where for example the oxide film formation on fresh metal surface may affect the slip reversal. For generality, we first consider that two separate slip mechanisms operate in alternating slip processes.

In the case of a triangular wave form during fatigue, Figure 3.3, the stress intensity varies with time as:

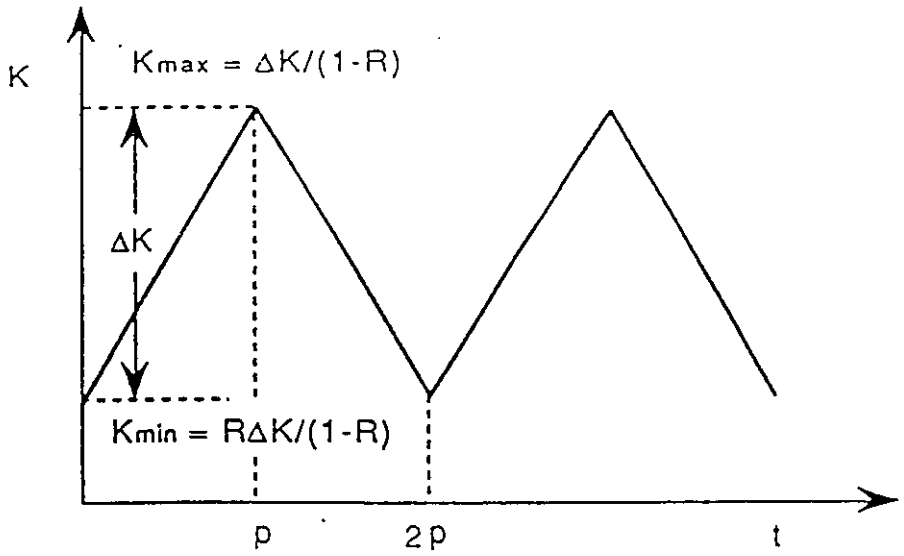

Figure 3.3. The schematic of triangular loading profile in fatigue, where R is the stress ratio.

$$\dot{K}(t) = \begin{cases} (\frac{R}{1-R} + \frac{t}{p})\Delta\dot{K} & 0 \le t \le p \\ (\frac{1}{1-R} + 1 - \frac{t}{p})\Delta\dot{K} & p \le t \le 2p, \end{cases} \tag{3.11}$$

where t is the time, p is the half cycle period, $\Delta K = K_{max} - K_{min}$ is the stress intensity range, $R = K_{min}/K_{max}$ is the stress ratio.

The forward strain γ_f can be obtained by integrating equation (3.10) over the rising load cycle,

$$\begin{aligned} \int_0^{\gamma_f} \exp\left(\frac{V_f H\gamma}{kT}\right) d\gamma &= \dot{\gamma}_{of} \exp\left(-\frac{\Delta G_f^{\ddagger} + V_f \tau_{of}}{kT}\right) \int_0^p \exp\left(\frac{\alpha_f \dot{K}}{kT}\right) dt \\ &= \dot{\gamma}_{of} \exp\left(-\frac{\Delta G_f^{\ddagger} + V_f \tau_{of}}{kT}\right) \int_0^p \exp\left[\frac{\alpha_f \Delta\dot{K}}{kT}\left(\frac{R}{1-R} + \frac{t}{p}\right)\right] dt \end{aligned}$$

and the result is

$$\frac{kT}{V_f H}\left[\exp\left(\frac{V_f H\gamma_f}{kT}\right)-1\right]$$
$$=\frac{\dot{\gamma}_{of}kT}{2f\alpha_f\Delta K}\exp\left(-\frac{\Delta G_f^{\ddagger}+V_f\tau_{of}}{kT}\right)\exp\left(\frac{\alpha_f R\Delta K}{(1-R)kT}\right)\left[\exp\left(\frac{\alpha_f\Delta K}{kT}\right)-1\right] \tag{3.12}$$

where the test frequency $f = 1/2p$, as defined in Figure 3.3.

Over the decreasing load cycle, the reverse plastic strain is obtained by

$$\int_0^{\gamma_r}\exp\left(\frac{V_r H\gamma}{kT}\right)d\gamma=\dot{\gamma}_{or}\exp\left(-\frac{\Delta G_r^{\ddagger}+V_r\tau_{or}}{kT}\right)\int_p^{2p}\exp\left(\frac{\alpha_r K}{kT}\right)dt$$
$$=\dot{\gamma}_{or}\exp\left(-\frac{\Delta G_r^{\ddagger}+V_r\tau_{or}}{kT}\right)\int_p^{2p}\exp\left[\frac{\alpha_r\Delta K}{kT}\left(\frac{1}{1-R}+1-\frac{t}{p}\right)\right]dt$$

and the result is

$$\frac{kT}{V_r H}\left[\exp\left(\frac{V_r H\gamma_r}{kT}\right)-1\right]$$
$$=\frac{\dot{\gamma}_{or}kT}{2f\alpha_r\Delta K}\exp\left(-\frac{\Delta G_r^{\ddagger}+V_r\tau_{or}}{kT}\right)\exp\left(\frac{\alpha_r R\Delta K}{(1-R)kT}\right)\left[\exp\left(\frac{\alpha_r\Delta K}{kT}\right)-1\right]. \tag{3.13}$$

Often for a ductile material at low temperature ($T < 0.3T_m$, T_m is the absolute melting temperature), the condition:

$$\exp\left(\frac{VH\gamma}{kT}\right)\gg 1 \quad \text{and} \quad \exp\left(\frac{\alpha\Delta K}{kT}\right)\gg 1 \tag{3.14}$$

is satisfied. For example, for a typical value of the activation volume of $80b^3$, $b = 2.5\times10^{-10}$m, and a work hardening coefficient of 1000 MPa, if the ductility is taken as 20%, the magnitude of the term $\exp\left(\frac{VH\gamma}{kT}\right)$ approximates e^{60} which is much greater than

unity. For mechanically assisted thermal activation, the activation work, $\alpha\Delta K - V H\gamma - \tau_o$, is positive. Hence, $\alpha\Delta K > V H\gamma$ and $\exp\left(\frac{\alpha\Delta K}{kT}\right) \gg 1$. Therefore, condition (3.14) is valid for most test and service conditions. Then the forward slip plastic strain in equation (3.12) can be approximated by:

$$\gamma_f = \frac{kT}{V_f H} \ln\left[\frac{V_f H \dot{\gamma}_{of}}{2f\alpha_f \Delta K} \exp\left(-\frac{\Delta G_f^{\ddagger} + V_f \tau_{of}}{kT}\right)\right] + \frac{\alpha_f \Delta K}{(1-R)V_f H}. \tag{3.15}$$

and, similarly, the reverse slip plastic strain can be depicted by:

$$\gamma_r = \frac{kT}{V_r H} \ln\left[\frac{V_r H \dot{\gamma}_{or}}{2f\alpha_r \Delta K} \exp\left(-\frac{\Delta G_r^{\ddagger} + V_r \tau_{or}}{kT}\right)\right] + \frac{\alpha_r \Delta K}{(1-R)V_r H}. \tag{3.16}$$

The net cyclic plastic strain range ahead of the crack tip can be calculated as:

$$\gamma_f - \gamma_r = \ln\left[\frac{\left(\frac{V_f H \dot{\gamma}_{of}}{2f\alpha_f \Delta K}\right)^{\frac{kT}{V_f H}} \exp\left(-\frac{\Delta G_f^{\ddagger} + V_f \tau_{of}}{V_f H}\right)}{\left(\frac{V_r H \dot{\gamma}_{or}}{2f\alpha_r \Delta K}\right)^{\frac{kT}{V_r H}} \exp\left(-\frac{\Delta G_r^{\ddagger} + V_r \tau_{or}}{V_r H}\right)}\right] + \left(\frac{\alpha_f}{V_f H} - \frac{\alpha_r}{V_r H}\right) \frac{\Delta K}{1-R}. \tag{3.17}$$

Then, the crack growth rate according to equation (3.7) can be expressed as:

$$\frac{da}{dN} = \frac{(\alpha_f V_r - \alpha_r V_f)}{12\pi(1-R)V_f V_r H} (\Delta K - \Delta K_{th}) \left(\frac{\Delta K}{\sigma_y}\right)^2 \tag{3.18}$$

where

$$\Delta K_{th} = \frac{(1-R)HV_f V_r}{\alpha_f V_r - \alpha_r V_f} \left[\frac{1}{H}\left(\tau_{of} - \tau_{or} + \frac{\Delta G_f^{\ddagger}}{V_f} - \frac{\Delta G_r^{\ddagger}}{V_r}\right) - \ln \frac{\left(\frac{V_f H \dot{\gamma}_{of}}{2f\alpha_f \Delta K}\right)^{\frac{kT}{V_f H}}}{\left(\frac{V_r H \dot{\gamma}_{or}}{2f\alpha_r \Delta K}\right)^{\frac{kT}{V_r H}}}\right] \tag{3.19}$$

Equation (3.19) defines the fatigue threshold condition in terms of a complex function of temperature, frequency, and stress ratio. The ΔK_{th} value is a microstructure – environment sensitive variable because it is controlled by activation energies, activation volumes and activation work factors.

In mechanical fatigue, where microstructure is stable and where environmental effects are absent, α_f and α_r are in the same order of magnitude, and both forward slip and slip reversal occur by the same mechanism so that $\Delta G_f^{\ddagger} = \Delta G_r^{\ddagger}$, $V_f = V_r = V$, $\tau_{of} = \tau_{or}$ and $\dot{\gamma}_{of} = \dot{\gamma}_{or}$, ΔK_{th} vanishes to zero because $kT/VH \ll 1$. Hence for pure mechanical fatigue:

$$\frac{da}{dN} = \frac{(\alpha_f - \alpha_r)\Delta K^3}{12\pi(1-R)VH\sigma_y^2}. \tag{3.20}$$

Equation (3.20) is similar to the Paris relationship (equation (2.2)) with a physically defined proportional factor and power law exponent.

3.3 Experimental Verification of The Proposed Model

Transgranular fatigue crack growth data for a variety of alloys, tested at room temperature in vacuum, over a frequency range of 1 to 5 Hz, are shown in Figure 3.4 [26], where crack growth rates vary as a power law function of ΔK with an exponent value of 3 within the Paris regime. The alloy designations and yield strength values are given in Table 3.1, and the values of the proportional constant variable $(\alpha_f - \alpha_r)/VH$, which are estimated by fitting to test data [26], are also listed. Fatigue crack growth in certain engineering alloys, tested at room temperature in low humidity air, also exhibits a similar behavior [94], as demonstrated in Figure 3.5. In addition to this, experiments have also shown that in a large number of alloys the power law exponent falls within the range of $2.7 \sim 3.4$ [95]-[101], as listed in Table 3.2. The power law exponent values are found to be closer to 3 than 2 or 4, which are the values predicted by other models [52]-[57].

Outside of the Paris regime, in Figure 3.4, the fatigue crack growth rate data deviates from the fitted lines with the slope of 3 in Zr, Ti and Fe at ΔK values lower than 10MPa$\sqrt{\text{m}}$ whereas at very high ΔK values, the slopes are considerably greater than 3 in all cases. The derivation at low ΔK values may be caused by crack closure which is not included in the present crack propagation model. The deviation in the predicted and the observed slopes at very high ΔK values is not totally unexpected because the "static

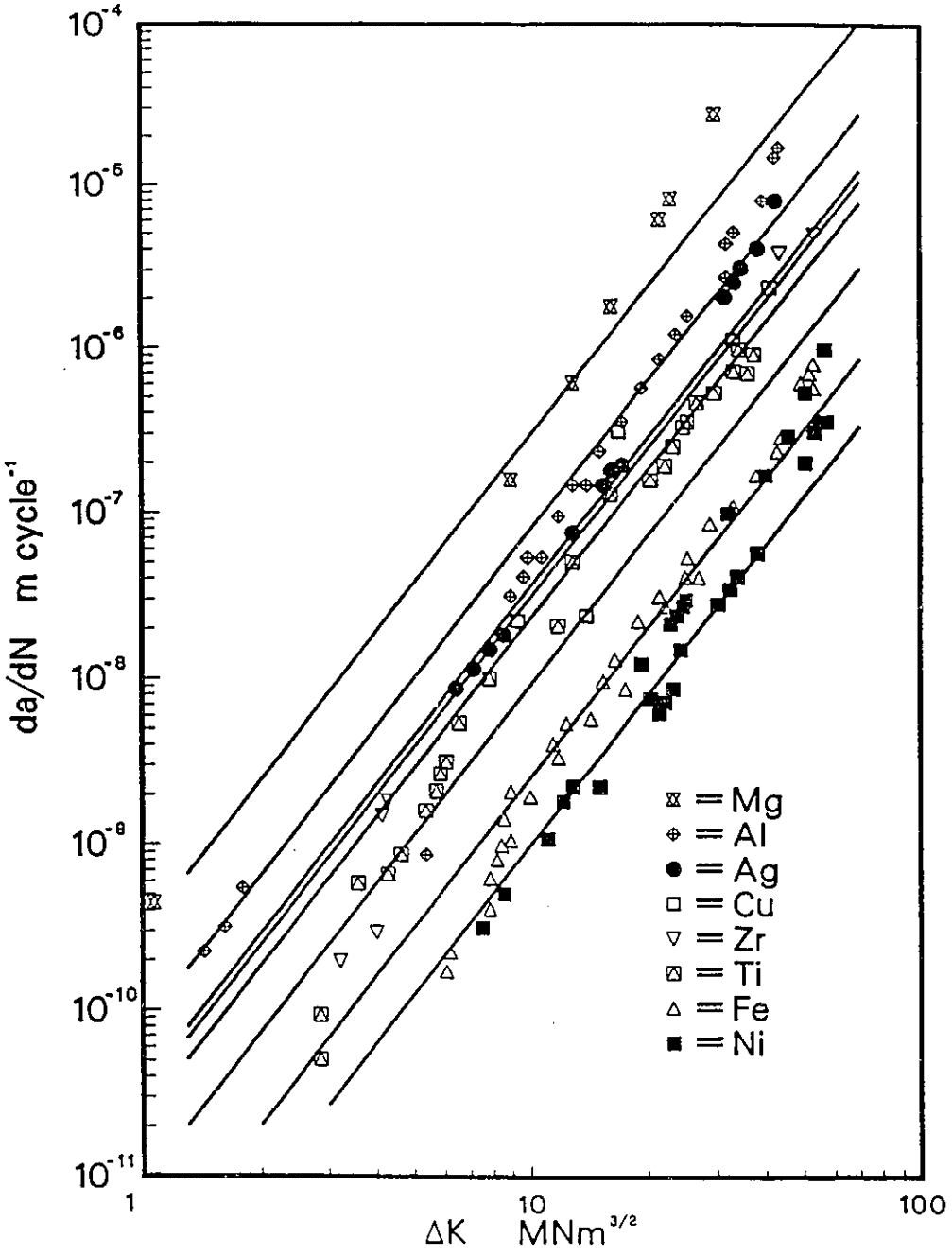

Figure 3.4. Fatigue crack growth rate versus stress intensity for a series of metals, tested at room temperature in vacuum. Symbols represent the observed behavior [26], the lines represent equation (3.20).

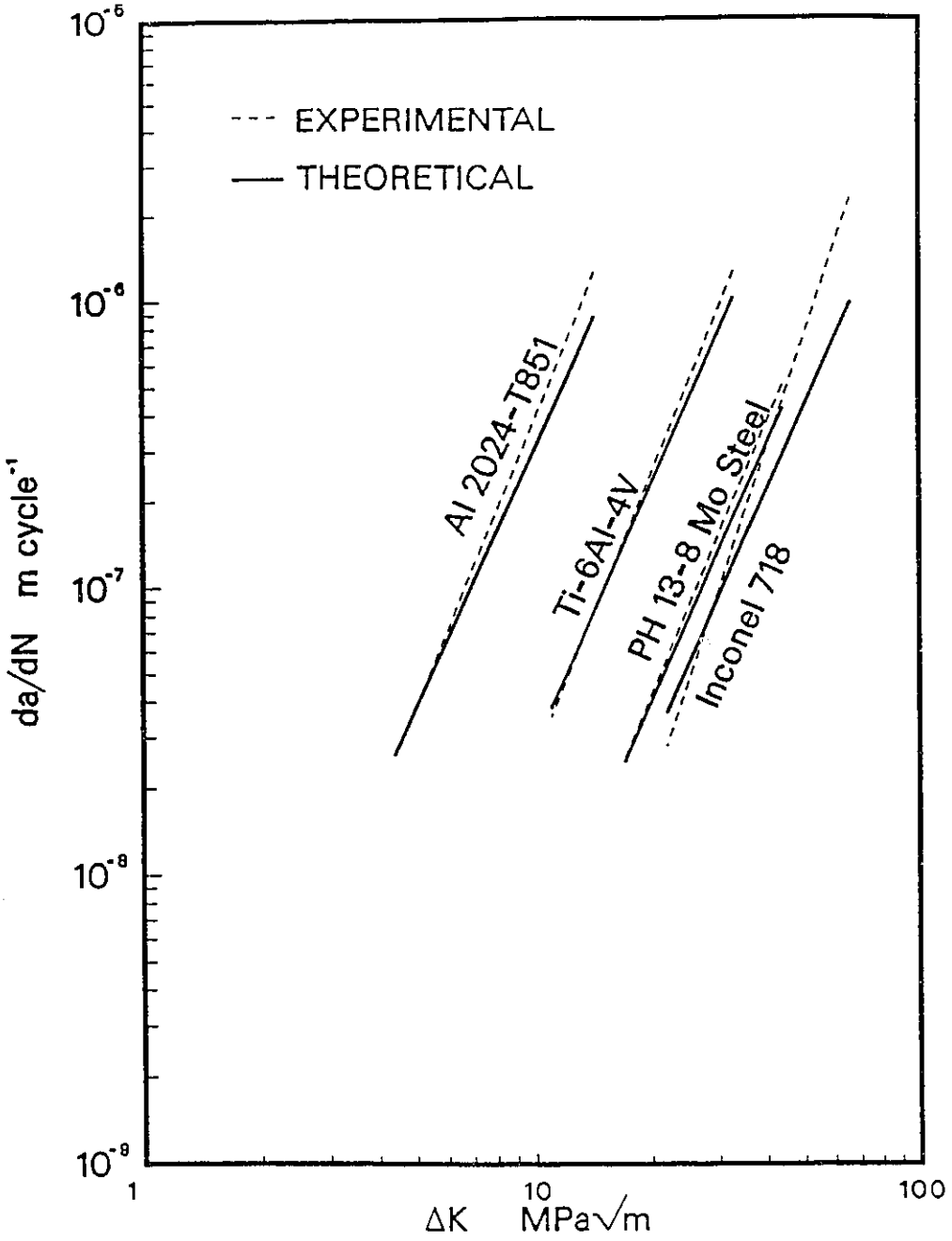

Figure 3.5. Fatigue crack growth rate versus stress intensity for a number of alloys, tested at room temperature in low humidity air. The dashed lines represent experimental observations [94], the solid lines represent equation (3.20).

mode" fracture (such as void growth and ductile dimple formation) occurs concurrently with the RSR process [20,102] and this would obviously increase the crack growth rate. It is thus evident that the agreement between theory and experiments is quite good in the Paris regime.

3.4 Discussion

The restricted slip reversal (RSR) model provides a physical description for crack initiation and growth processes that result in transgranular fracture. The model also provides a physical basis for striation formation during fatigue crack growth, a feature that has been verified through numerous experimental observations. The fatigue crack growth rate is shown to be dependent on microstructure (activation volume and work factor), material properties (yield stress and work hardening coefficient) as well as test conditions (ΔK and R). The relationship between these parameters takes the same form as the Paris equation (2.2) with the power law exponent of 3:

$$\frac{da}{dN} = C(\Delta K)^3 \tag{3.21}$$

where

$$C = \frac{(\alpha_f - \alpha_r)}{12\pi(1-R)VH\sigma_y^2}$$

It is interesting to note that if ΔK_{th} in equation (3.18) is negligible, the test environment and material mirostructure only affect the constant C in equation (3.21) rather than the power law exponent.

3.4.1 The effects of R, σ_y and H

In equation (3.21), the proportional constant C is expressed as a function of microstructure (α_f, α_r, V), material properties (σ_y, H) and stress ratio, R. For microstructurally stable alloys where the microstructure does not change with the mean stress, the R

dependence predicted by equation (3.21) is similar to the Forman equation (2.3). In the Paris regime where $\Delta K \ll K_c$, the Forman equation,

$$\frac{da}{dN} = \frac{C'\Delta K^3}{(1-R)K_c - \Delta K},$$

can be correlated to equation (3.21) with $C' = C(1-R)K_c$ and $n = 3$. Figure 3.6 shows the R-dependence of fatigue crack growth in 7075-T651 aluminum alloy. Close agreement was found between the theoretical description and the observed behavior.

Different materials have different microstructures which will affect their mechanical properties and the slip behavior. It is difficult to isolate their individual effects on crack growth rate because they vary with each other. Benson examined the effect of yield strength on fatigue crack growth rate using $\frac{1}{2}$Cr-$\frac{1}{2}$Mo-$\frac{1}{4}$V steel transformed (after austenitization) at different temperatures [105]. The corresponding mechanical properties are given in Table 3.3 [105]. From these, the work hardening coefficients are roughly estimated by

$$H = (\text{UTS-YS})/\text{El.}$$

where El. = 13%, typical for this class of steels (Metals Handbook Vol. I).

Plotting the fatigue crack growth rate data against $H\sigma_y^2$, as shown in Figure 3.7, it can be seen that the crack growth rate, da/dN, is indeed inversely proportional to the mechanical factor $H\sigma_y^2$.

3.4.2 Threshold

Equation (3.19) further predicts that the intrinsic threshold of fatigue crack growth does not occur in the absence of any microstructural change and environmental effects ahead of the crack tip such as in the case of pure mechanical fatigue. This also implies that, for stable microstructure, the intrinsic fatigue threshold solely occurs as a result of environmental interactions. The model, in its basic expression in the context

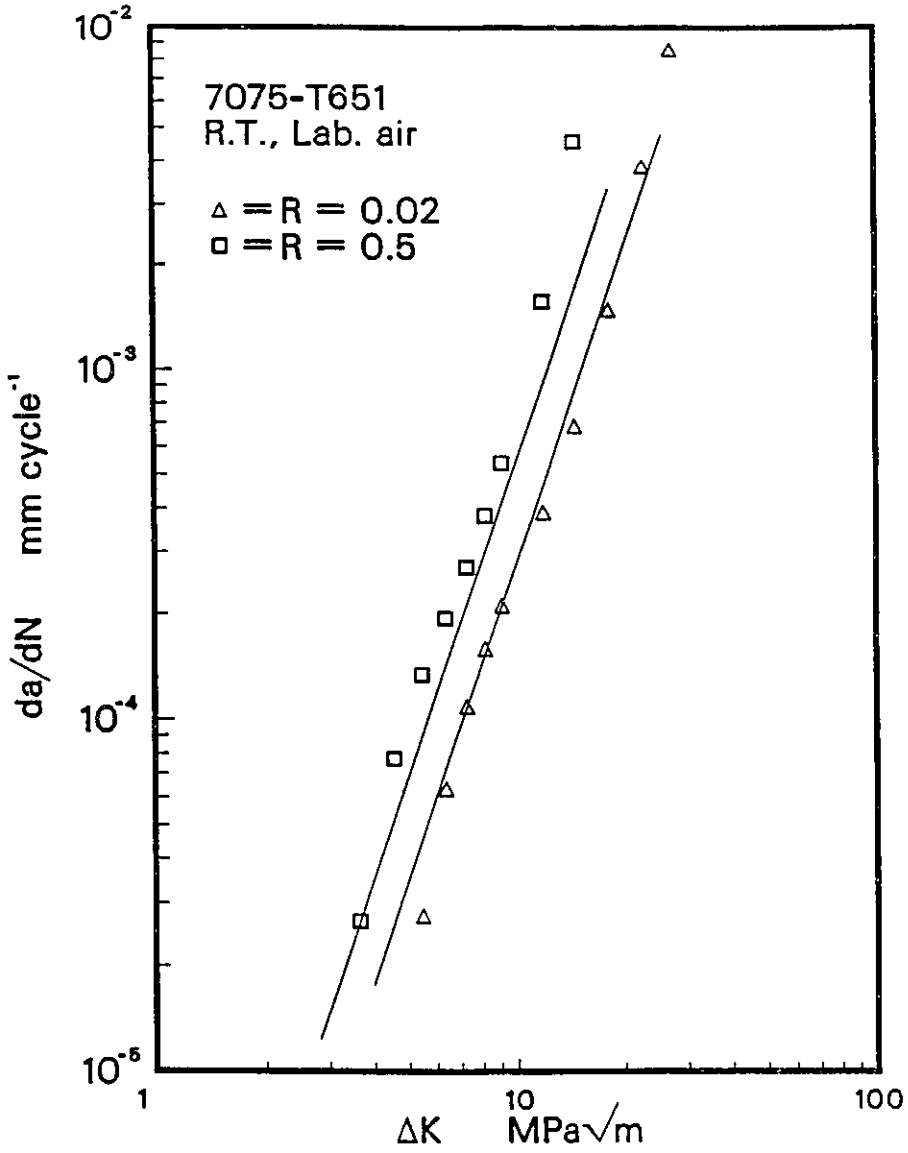

Figure 3.6 The R effect on fatigue crack growth in 7075-T651 alminum alloy. Symbols represent the observed behavior [94]; the lines were obtained from equation (3.21) with the proportional constant variable $(\alpha_f - \alpha_r)/[12\pi HV\sigma_y^2] = 2.75 \times 10^{-7}$ mm $(\mathrm{MPa}\sqrt{\mathrm{m}})^{-3}$.

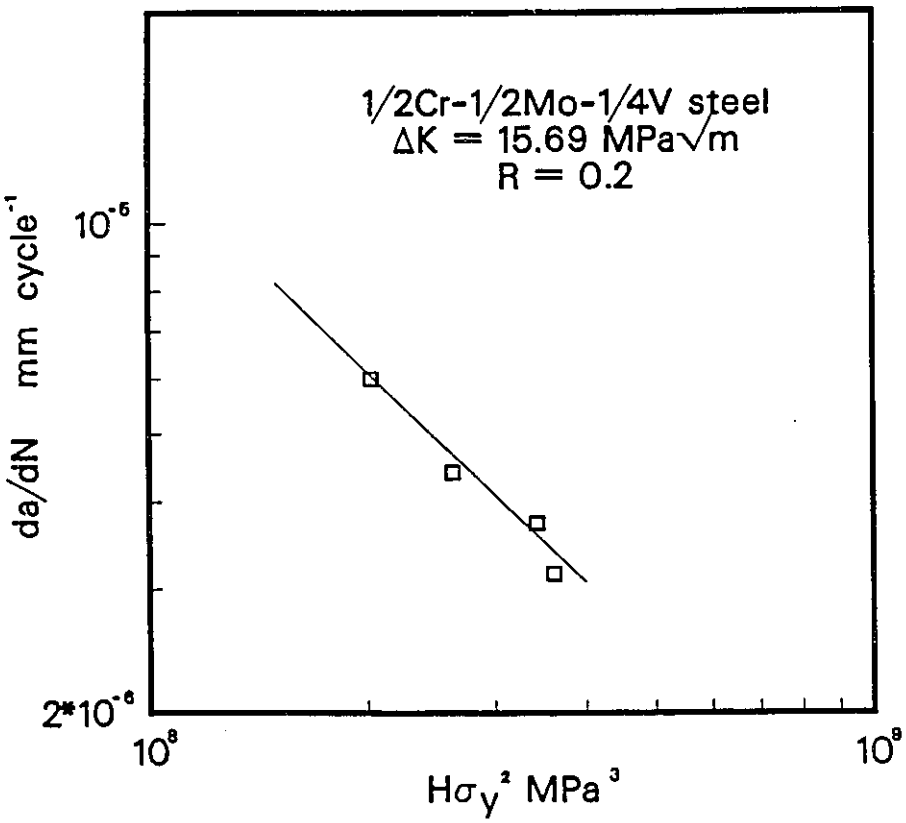

Figure 3.7 Variation of fatigue crack growth rate with $H\sigma_y^2$ in $\frac{1}{2}$Cr-$\frac{1}{2}$Mo-$\frac{1}{4}$V steel transformed at 450°, 550°, 750° and quenched and tempered; test data after Benson [105].

of equations (3.18) and (3.19), describes this environmental effect by assuming that the environment influences the characteristic activation quantities ($\Delta G^{\ddagger}$, α, V) in both forward slip and slip reversal processes. Quantitatively, ΔK_{th} will only become significant in equation (3.19) if τ_{of} is greater than τ_{or}, $\Delta G_r^{\ddagger}$ is smaller than $\Delta G_f^{\ddagger}$ and/or V_r is considerably greater than V_f. In practical terms, this may happen when environmental effects weaken the point defect obstacles after the new crack surface exposure, which will result in a decrease of both $\Delta G_r^{\ddagger}$ and τ_{or}, or when some weak point obstacles are cut by dislocations during the forward slip and do not act as obstacles in the slip reversal, which will result in an increase of V_r. Indeed, corrosion fatigue is a complex process and detailed kinetics need to be specified when considering other mechanisms such as corrosion debris formation [106]. However, fatigue threshold may occur as the result of extrinsic shielding (viz. roughness-induced crack closure, etc.). Crack closure is often quantified by a measured stress intenssity level, K_{cl}, below which the crack does not propagate and above which the crack is in the opening mode. It is reasonable to assume that alternating slip processes only operate in the range from K_{cl} to K_{max}. Then, the effective stress intensity range $\Delta K_{eff} = K_{max} - K_{cl}$ and the revised stress ratio $R' = K_{cl}/K_{max}$ should be used to substitute for ΔK and R in equation (3.21) to take account of crack closure effects.

In conclusion, the proposed model correlates transgranular fatigue crack growth with the plastic deformation accommodation ahead of the crack tip. Its formulation through equation (3.5) comes out of a rationale based on the physically realistic RSR model, although the subsequent theoretical treatment deals primarily with positive R values and small scale yielding conditions, where stress intensity factor is believed to control the near-tip stress field. The model could be further modified to incorporate cyclic hardening or softening and large scale yielding effects but it is beyond the scope of the present study to digress on these issues any further.

Table 3.1 Materials Tested in Vacuum [26]

Designation	Material	σ_y MPa	$(\alpha_f - \alpha_r)/HV$ $(\text{MPa}\sqrt{\text{m}})^{-}1$
Mg	ZK60A-T5	296	9.9×10^{-4}
Al	7079-T6	463	6.46×10^{-4}
Ag	pure silver	300	1.22×10^{-4}
Zr	Zircaloy 4	470	1.91×10^{-4}
Cu	70/30 Brass	560	3.66×10^{-4}
Ti	Ti-6Al-4V	990	3.38×10^{-4}
Fe	300M	1700	2.77×10^{-4}
Fe	12% St 12T	690	4.56×10^{-5}
Fe	460 TS	590	3.33×10^{-5}
Fe	Type 304	270	6.98×10^{-6}
Ni	pure nickel 201	165	1.03×10^{-6}
Ni	Inconel 600	340	4.36×10^{-6}
Ni	Inconel 738	930	3.26×10^{-5}
Ni	Nimonic 80 A	448	7.56×10^{-6}

Table 3.2 Experimental Values of Power Law Exponent for Alloys

Alloys	Power law exponent	Temperature	reference
Type 316 steel	3.4	25°C	[95]
AISI 301 & 302	2.73	25°C	[96]
Ti-6Al-4V	3.3	24°C	[97]
Alloy 718	3.0 ~ 3.4	24° ~ 427°C	[98,99,100]
Inconel X-750 forging	3.0	24°C	[101]
3.5 Ni steel	3.2	24°C	[101]
9 Ni steel	2.7	24°C	[101]
Type 304 annealed plate	3.0	24° ~ −269°C	[101]
Type 310S annealed plate	3.0	24°C	[101]
A-286 forging, STA	3.0	24°C	[101]
A-286 plate, STA	2.7	24°C	[101]

Table 3.3 Mechanical Properties of $\frac{1}{2}$Cr-$\frac{1}{2}$Mo-$\frac{1}{4}$V steel

$\frac{1}{2}$Cr-$\frac{1}{2}$Mo-$\frac{1}{4}$V	YS, MPa	UTS, MPa	RA, %
Transformed at 750°C	466	638	38
Transformed at 550°C	609	736	47
Transformed at 450°C	597	722	46
Quenched and Tempered	834	872	43

Chapter 4

Transgranular Fatigue Crack Growth in Al-Li Alloys

The development of aluminum-lithium (Al-Li) alloys has been motivated primarily by their potential for use in the next generation aerospace structures. Interest lies in their high modulus-to-weight ratio and superior performance, as compared with traditional high strength aluminum alloys.

It is now well known that aluminum-lithium alloys exhibit uncommonly good resistance to the growth of fatigue cracks and show extremely marked anisotropy in their mechanical properties and fracture behavior. Such performance is believed to be the consequence of strong textures developed during mill processing and the highly planar slip behavior of these alloys [111]. The unusual crack growth behavior of Al-li alloys has been noticed by many laboratories [107]-[110]. Particularly, it has been found that growing fatigue cracks in compact tension specimens may deflect from the plane of symmetry to follow sharply inclined crack planes. It is believed that the crystallographic crack growth may be related to the crystallographic texture in the material and the point of transition from "symmetrical crack" growth to crystallographic crack growth may be related to a "transition" stress intensity range under ΔK increasing conditions. While these fatigue crack growth phenomena in aluminum-lithium alloys are thought to be understood in qualitative terms, a complete understanding in physically rigorous, quantitative terms has not been provided. In addition, the practical implications of these fatigue phe-

nomena have not been considered. For example crack growth rates during the period of crystallographic cracking, in comparison to symmetrical crack growth rates, are not known.

In the study of this chapter, a series of tests has been run to demonstate the general feature of fatigue crack growth in Al-Li alloys and to generate experimental data on an alloy of current practical interest. Based on the information obtained from these tests, a FCGR model is developed which extends the concept of restricted slip reversibility to include the effect of texture (preferred orientation).

4.1 FCGR Testing

A series of FCGR tests (4 tests) has been carried out in this study to determine da/dN in a 8090 Al-Li alloy as a function of ΔK and specimen orientation with respect to the rolling direction. Variations in da/dN with specimen orientation would reflect the effect of texture on the FCGRs of the alloy.

4.1.1 Experimental Procedures

Material

The material studied was 8090-T8771 Al-Li alloy, in the form of 12.5 mm plate, provided by Dr. J. Morrison of the Defence Research Establishment Pacific. The nominal composition of the alloy is given in Table 4.1. Its mechanical properties in the longitudinal (L) direction are listed in Table 4.2. Four compact tension (CT) specimens, Figure 4.1, were cut from the original plate ($20 \times 20''$) such that the loading direction was a) parallel to the rolling direction (LT specimen), b) inclined at 15° (L+15° specimen), c) inclined at 30° (L+30° specimen) and d) inclined at 45° to the rolling direction (L+45° specimen). The CT specimens used conformed to ASTM E-647 specifications.

Table 4.1 Nominal Alloy Composition

Element (wt. %)						
Li	Cu	Mg	Zr	Fe	Si	Al
2.37	1.13	0.74	0.11	0.05	0.03	Bal.

Table 4.2 Mechanical Properties

Orientation	σ_y (MPa)	σ_u (MPa)	El. (%)
L	471	546	5.6

Instrumentation

FCGR testing was performed on a MTS 810 testing system at the SML-IAR, NRC. Measurements of crack opening displacement (COD) were obtained using a clip-on gage (MTS 632.02c-20) placed between knife edges mounted on the front face of the specimen on either side of the machined notch. A traveling microscope was used to measure crack length on either side of the specimen. The traversing stage of the microscope was readable to 0.01 mm.

Test Conditions and Procedures

All CT specimens were precracked in fatigue at a maximum load of 8 kN and a minimum load of -0.0125 kN at a frequency of 20 Hz. The precracked length $a_o > 1.4$ mm. Constant amplitude FCGR tests were conducted under the following conditions:

Test Frequency:	f = 20 Hz;
Maximum Load:	$P_{max} = 8$ kN;
Stress Ratio:	$R = P_{min}/P_{max} = K_{min}/K_{max} = 0.1$;
Environment:	laboratory air;
Wave Form:	sine wave;
Test Temperature:	RT.

The maximum load was chosen to yield ΔK values in the range of 10-30 MPa$\sqrt{\text{m}}$. At

these ΔK values, the size of the plastic zone ahead of the crack tip was presumed to be small compared to the crack length such that linear elastic fracture mechanics could be applied in accordance with ASTM E-647 specifications.

At selected cycle intervals, fatigue cycling was stopped, then the load vs COD relation was recorded and, at the maximum load, crack length was measured. This test sequence was repeated until the specimens fractured.

4.1.2 Results and Discussion

It was observed that crystallographic crack growth occurred in all specimens, exhibiting meandering crack path profiles. In the LT, L+15° and L+30° specimens, the macroscopic crack propagates along the direction normal to the rolling direction but the catastrophic fracture occur slantingly. In the L+45° specimen, fatigue crack propagates in the notch direction but the catastropic fracture occurs along the plane normal to the rolling direction. Pictures of the broken specimens are shown in Figure 4.2. It appears that LT and L+45° planes are the planes of microstructural symmetry in 8090 Al-Li plate.

Compliance data for LT, L+15°, L+30°, L+45° specimens are plotted against the crack geometry parameter a/W as shown in Figure 4.3, where the projected crack length is used for a and CEB represents the normalized compliance (B×E× COD/P, where B is the specimen thickness and E is the elastic modulus, COD is the crack opening displacement measured from the crack mouth and P is the load). It can be seen from Figure 4.3 that the normalized compliance varies slightly with the specimen orientation.

It was observed that catastrophic fracture occurred at different crack lengths in different specimens. Crack length vs number of cycles cycle data for the four specimen are shown in Figure 4.4. Since the final crack length can be related to the fracture toughness, the results indicate that fracture toughness, K_c, is also a function of specimen orientation. Statistically significant data base will have to be generated to determine whether these results represent a general trend.

Since, in all the specimens, the macroscopic crack deflection is less than 30° with respect

to the notch direction, it is appropriate to use the projected crack length to calculate the stress intensity factor ΔK [112]. The fatigue crack growth rate, da/dN, is calculated from the crack length vs cycle number relation using the secant method, i.e.,

$$\frac{\Delta a}{\Delta N} = \frac{a_{i+1} - a_i}{N_{i+1} - N_i} \tag{4.1}$$

at $\bar{a} = (a_{i+1} + a_i)/2$. da/dN vs ΔK relations for LT, L+15°, L+30° and L+45° specimen orientations are shown in Figure 4.5, and all data are shown in Figure 4.6. It can be concluded from Figures 4.4 and 4.6 that LT orientation exhibits the best fatigue crack growth resistance and the fatigue crack growth resistance is increasingly reduced with an increase in the inclined angle with respect to the LT orientation. One exception to this trend was observed during crack growth in the L+30° specimen, which showed higher crack growth rates than the L+45° specimen at low ΔK values. This could be attributed to the presence of "cleavage like" fracture initiated during specimen precracking and continued to dominate the crack path in the early stage of crack growth up to a ΔK value of about 16 MPa$\sqrt{\text{m}}$. This "cleavage like" fracture formed a flat fracture surface. The same mode of crack growth was also observed in L+45° during precracking but not to the same extent as in the L+30° specimen. This may accounts for the earlier failure of the L+30° specimen than the L+45° specimen. The reasons for the occurrence of such an unexpected mode of fracture are not clear. It is recommended that further tests on L+30° and L+45° specimens be run at a lower load to avoid any "overload" effect.

The crack closure effect was also examined under the increasing ΔK condition in these four tests. As shown in Figure 4.7, for all the specimens, the COD vs P relation exhibits a good linear behavior over the full load range. From this, no significant crack closure level could be detected following the ASTM recommended procedures [113].

4.2 The Mathematical Model

It is well recognized that planar slip is operative during fatigue crack growth in Al-Li alloys. Marked slip planarity results in faceted fatigue crack growth along intersecting slip bands and leads to periodic deflection in the direction of crack growth Figure 4.8

shows the fracture surface morphology which is comprised of intersecting slip band facets. Slip, i.e. dislocation glide, occurs in definite crystallographic directions and along definite crystallographic planes, usually the closely packed planes. The preferred slip system is thus defined by the preferred direction and the preferred plane. Slip bands in a face centered cubic (f.c.c.) system, such as an Al-Li-Cu alloy during fatigue, are anticipated to form along the (111) plane. In f.c.c. ploycrystalline materials with strong textures, the (111) pole is often displaced from the stress axis, and as a consequence, slip occurs along the preferred crystallographic planes which lie at angles of θ and ϕ with respect to the specimen width and thickness axes respectively. A three dimensional and a two dimensional view of such a deformation and fracture mechanism are shown schematically in Figure 4.9 and Figure 4.10 respectively. According to the concept of restricted slip reversibility, the net fatigue crack growth rate represents the difference between the distances travelled by dislocations within the plastic zone during forward slip (l_f) and slip reversal (l_r) in one load cycle. In the RSR model, the fatigue crack growth rate (FCGR) has been found to be equal to the product of the net plastic strain ahead of the crack tip and the plastic zone size, and this is expressed by the relationship [90] (equation (3.5)):

$$\frac{da}{dN} = (\gamma_f - \gamma_r) r_p \cos\theta. \tag{4.2}$$

where γ_f and γ_r are the plastic strain associated with the forward slip and slip reversal respectively, r_p is the plastic zone size and θ is the preferred slip direction (Figure 4.10).

The accumulation of plastic strain during dislocation glide is governed by the rate equation

$$\dot{\gamma} = \dot{\gamma}_o \exp\left[-\frac{\Delta G^{\ddagger} - (V\tau_{\phi\theta} - VH\gamma - V\tau_o)}{kT}\right]. \tag{4.3}$$

where $\tau_{\phi\theta}$ is the shear stress on the inclined slip plane (Figures 4.9 and 4.10). Upon resolving the applied stress onto this inclined plane, the shear stress is obtain, using the LEFM approach (see Appendix C for detail), as

$$\tau_{\phi\theta} = \tau_\theta \cos^2\phi$$

where τ_θ is the shear stress in θ-direction provided that the crack surface is perpendicular to the rolling plane, and according to LEFM (Appendix B),

$$\tau_\theta = \frac{K}{2\sqrt{2\pi r}} \sin\theta \cos\frac{\theta}{2}.$$

Taking the average of plastic strain rate (equation (4.3)) over the plastic zone (following the same procedure in section 3.2), the average crack-tip strain rate can be obtained as

$$\dot{\gamma} = \dot{\gamma}_o \exp\left[-\frac{\Delta G^\ddagger - (\alpha K \cos^2\phi - VH\gamma - V\tau_o)}{kT}\right] \tag{4.4}$$

where

$$\alpha = \frac{V}{2\sqrt{2\pi L}} \sin\theta \cos\frac{\theta}{2}.$$

Defining the stress intensity factor for an inclined crack plane as

$$K_\phi = K\cos^2\phi \quad \text{and} \quad \Delta K_\phi = \Delta K \cos^2\phi, \tag{4.5}$$

following the same procedures in section 3.2, the net plastic strain can be obtained by integration of equation (4.4) over the increasing load period for γ_f and over the decreasing load period for γ_r.

$$\gamma_f - \gamma_r = \ln\left[\frac{\left(\frac{V_f H\dot{\gamma}_{of}}{2f\alpha_f \Delta K_\phi}\right)^{\frac{kT}{V_f H}} \exp\left(-\frac{\Delta G_f^\ddagger + V_f \tau_{of}}{V_f H}\right)}{\left(\frac{V_r H\dot{\gamma}_{or}}{2f\alpha_r \Delta K_\phi}\right)^{\frac{kT}{V_r H}} \exp\left(-\frac{\Delta G_r^\ddagger + V_r \tau_{or}}{V_r H}\right)}\right] + \left(\frac{\alpha_f}{V_f H} - \frac{\alpha_r}{V_r H}\right)\frac{\Delta K_\phi}{1-R}. \tag{4.6}$$

Substituting equation (4.6) for $(\gamma_f - \gamma_r)$, equation (3.6) for $r_p \cos\theta$ into equation (4.2), the crack growth rate can be expressed as:

$$\frac{da}{dN} = \frac{(\alpha_f V_r - \alpha_r V_f)\cos^2\phi}{12\pi(1-R)V_f V_r H}(\Delta K - \Delta K_{th})(\frac{\Delta K}{\sigma_y})^2 \tag{4.7}$$

where

$$\Delta K_{th} = \frac{(1-R)HV_fV_r}{(\alpha_f V_r - \alpha_r V_f)\cos^2\phi} \ln \left[\frac{\left(\frac{V_r H \dot{\gamma}_{or}}{2f\alpha_r \cos^2\phi \Delta K}\right)^{\frac{kT}{V_r H}} \exp\left(-\frac{\Delta G_r^{\ddagger} + V_r \tau_{or}}{V_r H}\right)}{\left(\frac{V_f H \dot{\gamma}_{of}}{2f\alpha_f \cos^2\phi \Delta K}\right)^{\frac{kT}{V_f H}} \exp\left(-\frac{\Delta G_f^{\ddagger} + V_f \tau_{of}}{V_f H}\right)} \right] \tag{4.8}$$

In mechanical fatigue, where microstructure is stable and where environmental effects are absent, α_f and α_r are in the same order of magnitude, and both forward slip and slip reversal occur by the same mechanism so that $\Delta G_f^{\ddagger} = \Delta G_r^{\ddagger}$, $V_f = V_r = V$, $\tau_{of} = \tau_{or}$ and $\dot{\gamma}_{of} = \dot{\gamma}_{or}$, and as a result, the ΔK_{th} term in equation (4.7) vanishes to zero because $kT/VH \ll 1$. Hence, in highly textured materials, the FCGR under pure mechanical fatigue condition is given by

$$\frac{da}{dN} = \frac{(\alpha_f - \alpha_r)\cos^2\phi}{12\pi(1-R)VH\sigma_y^2}(\Delta K)^3. \tag{4.9}$$

Here the proportionality constant would change with specimen orientation because the work factors, as in equation (4.4), the yield strength and work hardening coefficient of this 8090 Al-Li alloy are all directionality-dependent variables. The quantitative analysis of these individual effects will be examined in future works.

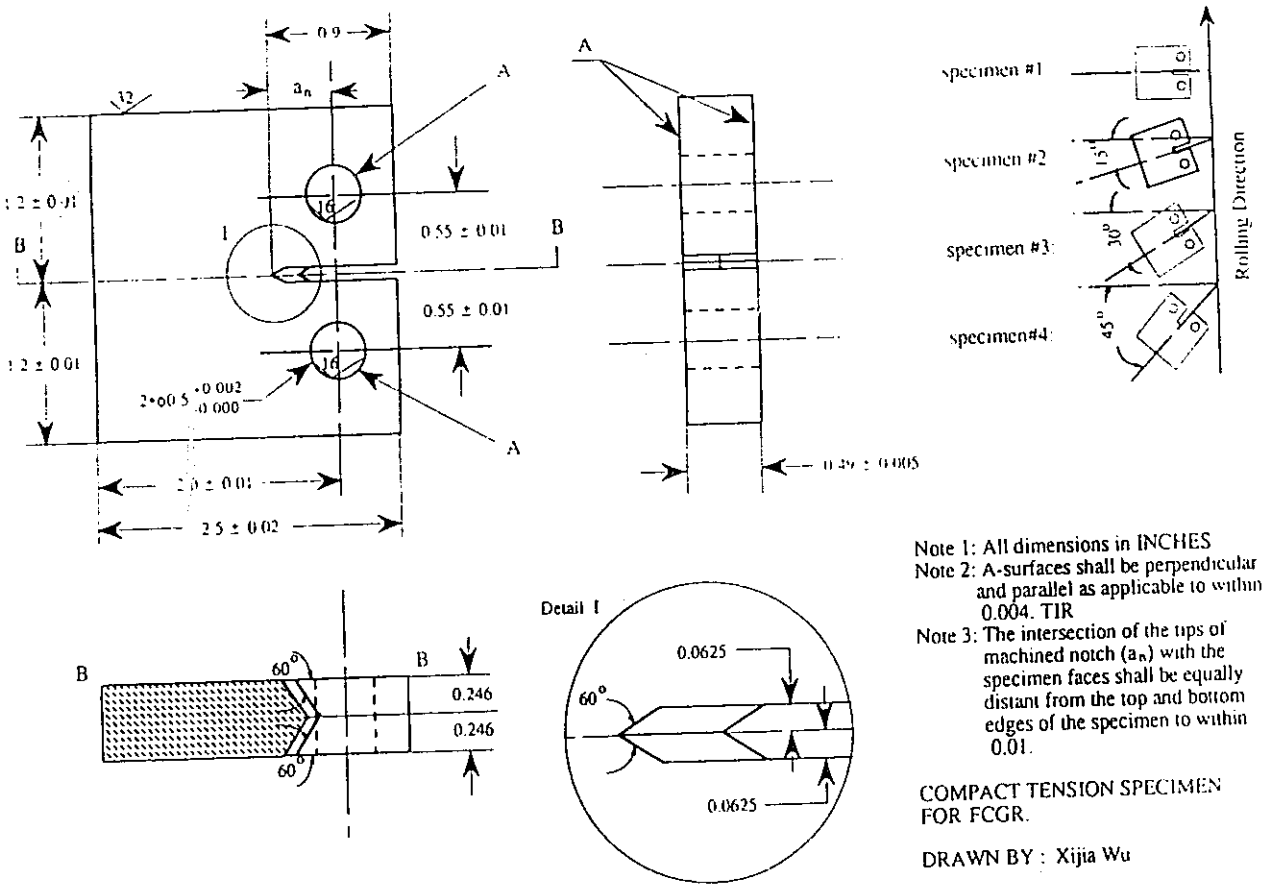

Figure 4.1. Dimensions of the C(T) specimen and their orientation with respect to the rolling direction.

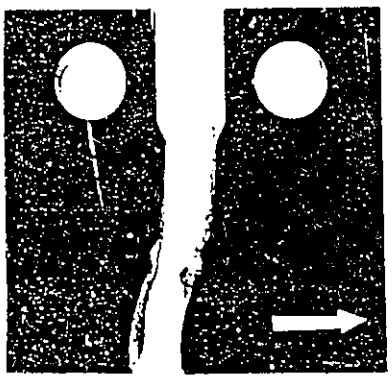

a) LT

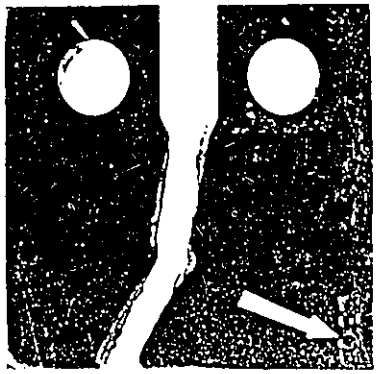

c) L+30°

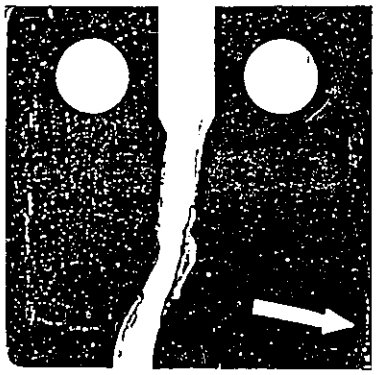

b) L+15°

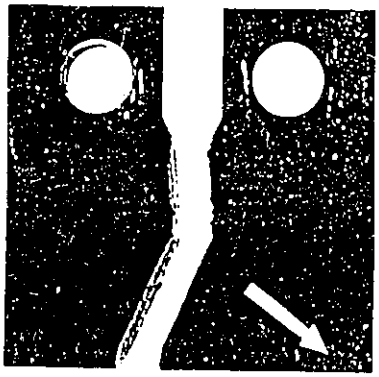

d) L+45°

Figure 4.2. Pictures of broken specimens: a) LT; b) L+15°; c) L+30°; and d) L+45° specimen. Arrows indicate the rolling direction.

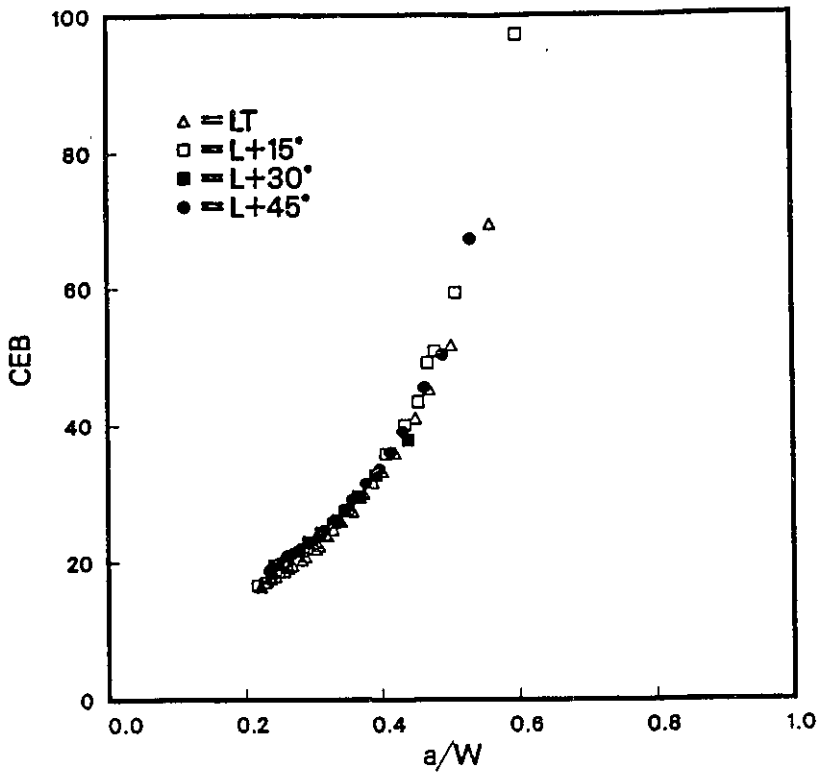

Figure 4.3. Compliance vs a/W relations for a) LT; b) L+15°; c) L+30°; and d) L+45° specimen.

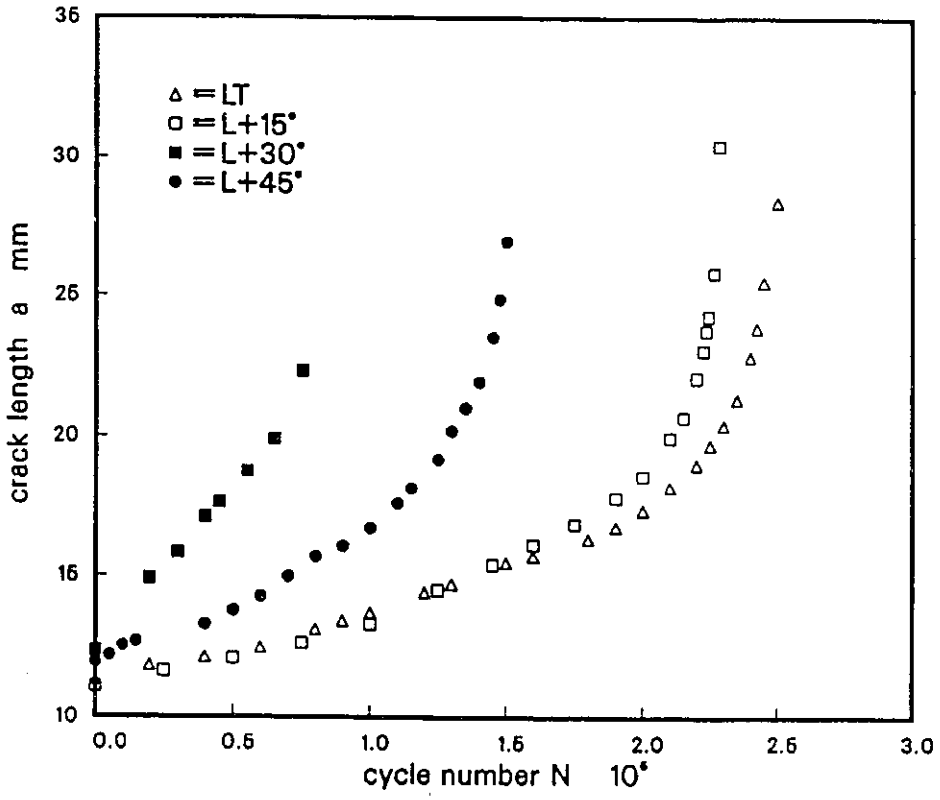

Figure 4.4. Crack length vs cycle number relations.

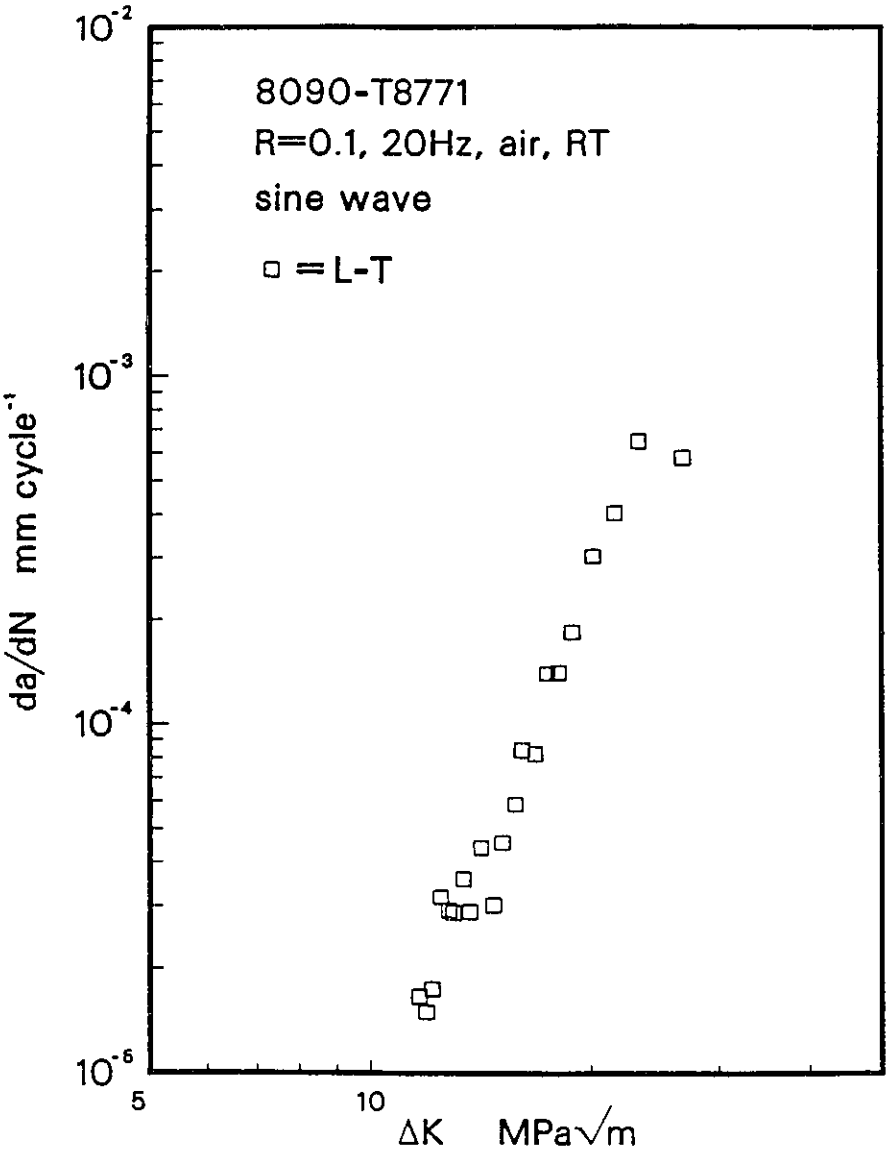

Figure 4.5. fatigue crack growth rate in a) LT;

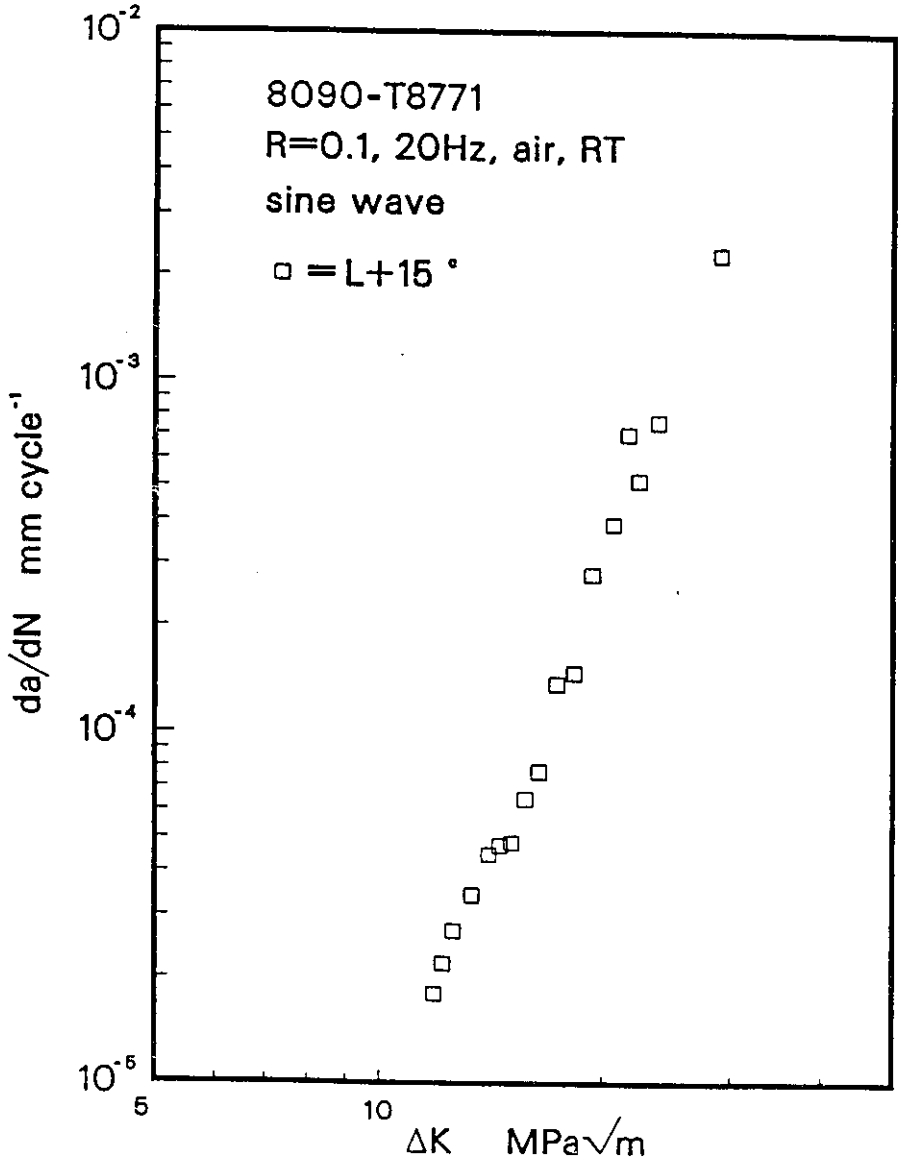
8090-T8771
R=0.1, 20Hz, air, RT
sine wave
□ =L+15 °
da/dN mm cycle⁻¹
10⁻²
10⁻³
10⁻⁴
10⁻⁵
5
10
ΔK MPa√m

b) L+15°;

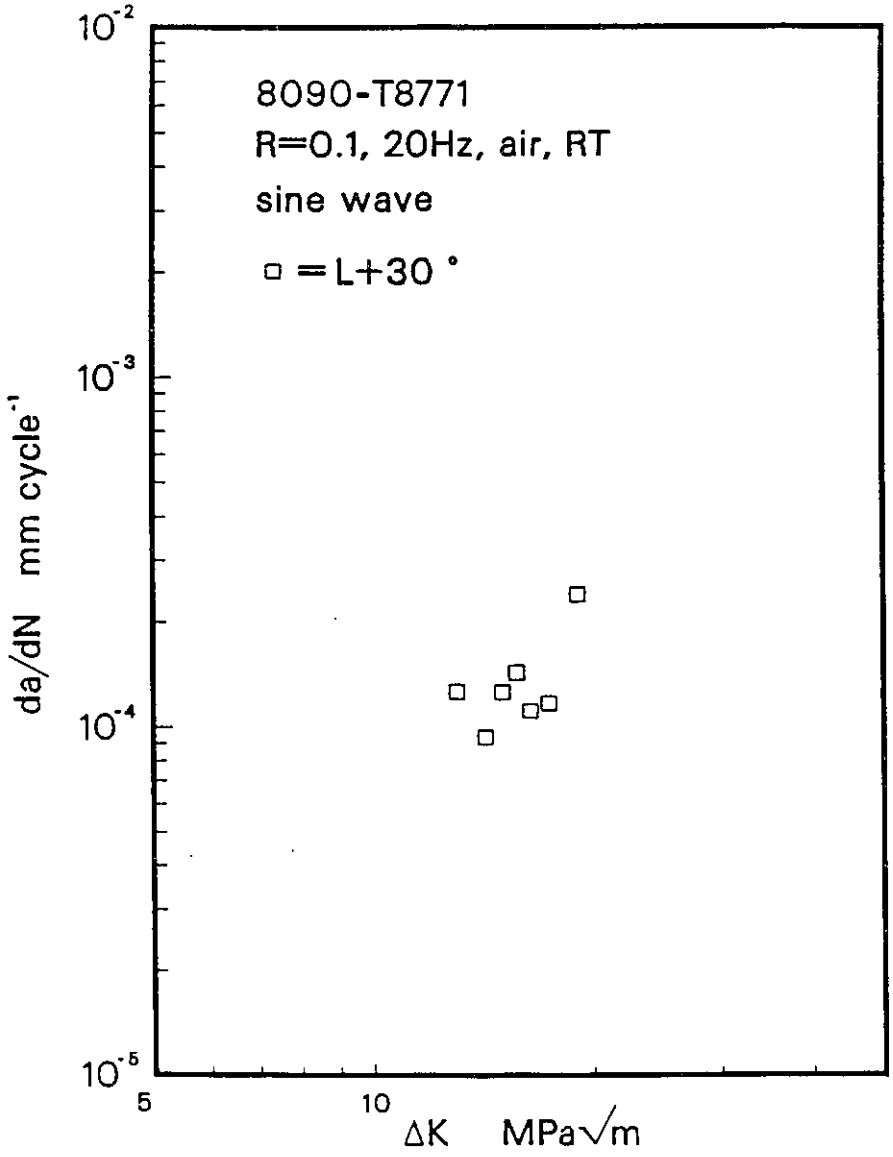
8090-T8771
R=0.1, 20Hz, air, RT
sine wave
□ =L+30 °
da/dN mm cycle⁻¹
10⁻²
10⁻³
10⁻⁴
10⁻⁵
5
10
ΔK MPa√m

c) L+30°;

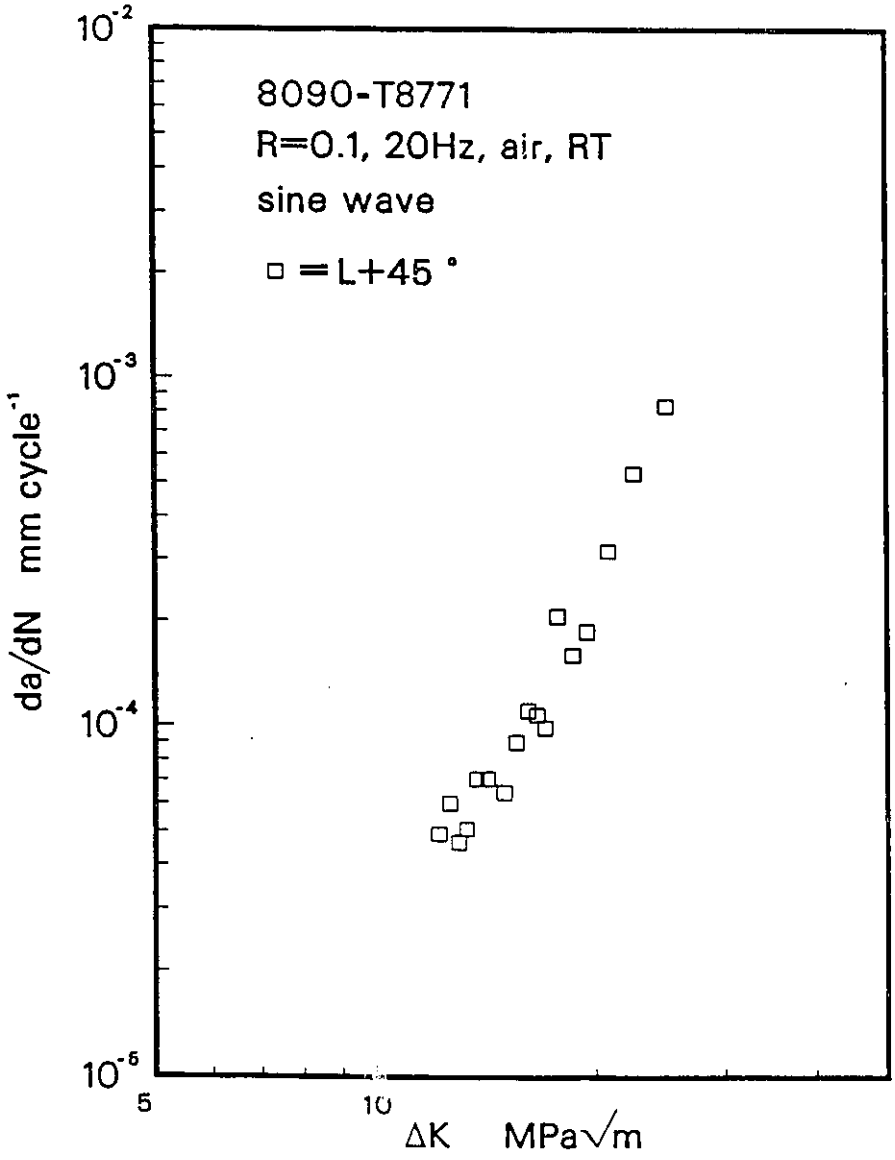

and d) L+45° specimen.

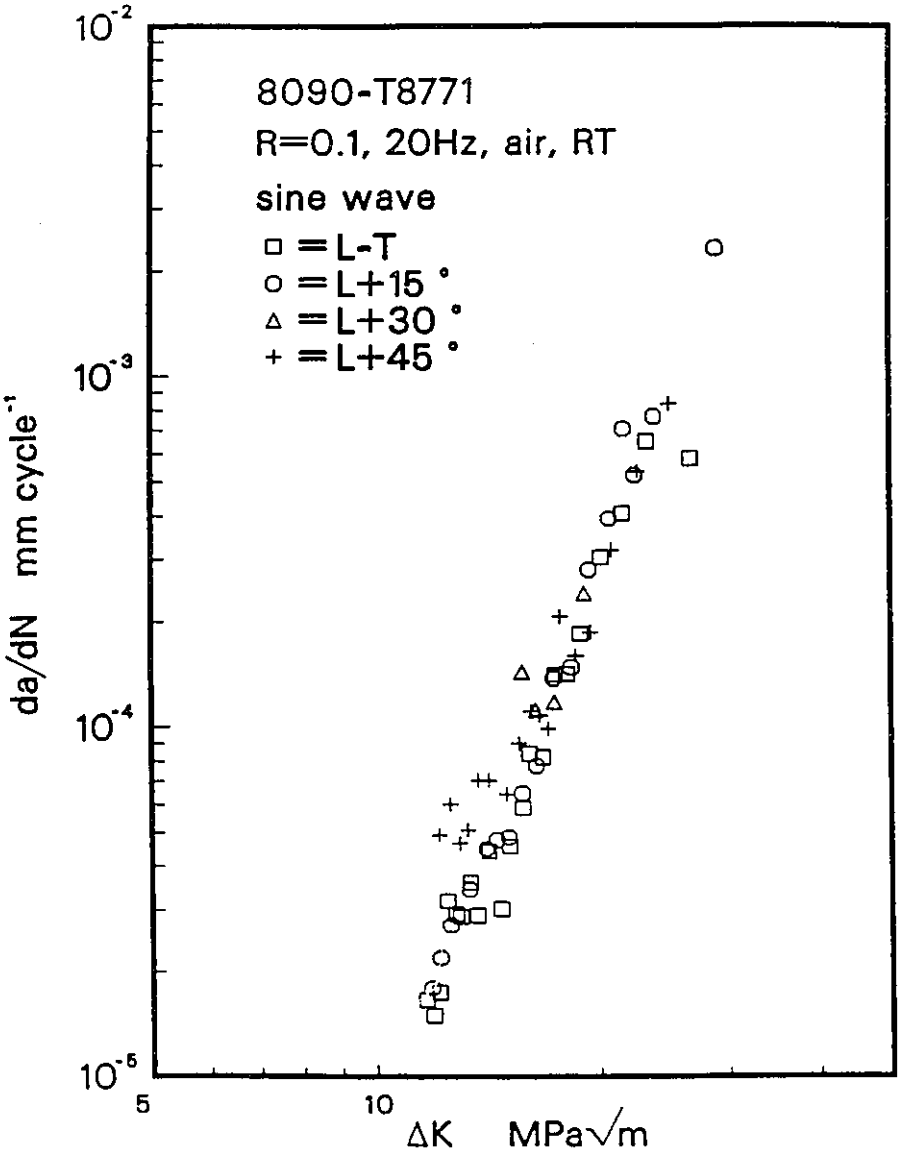

Figure 4.6. Comparison of da/dN along different orientations.

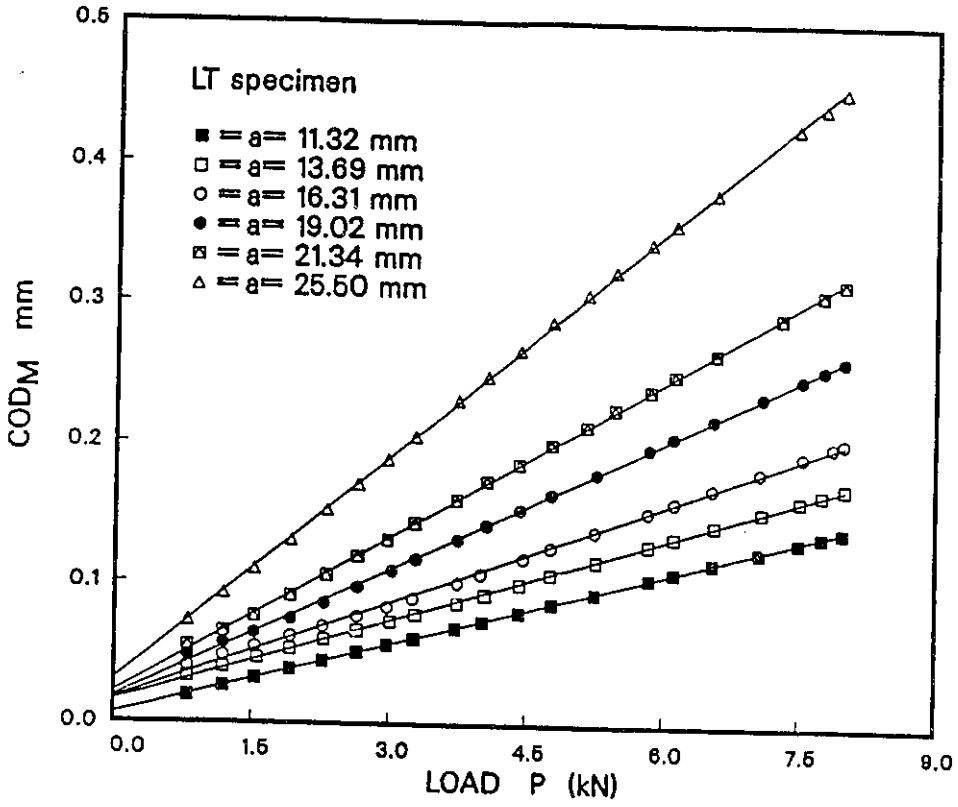

Figure 4.7. Crack opening displacement (COD) vs load (P) relations for a) LT;

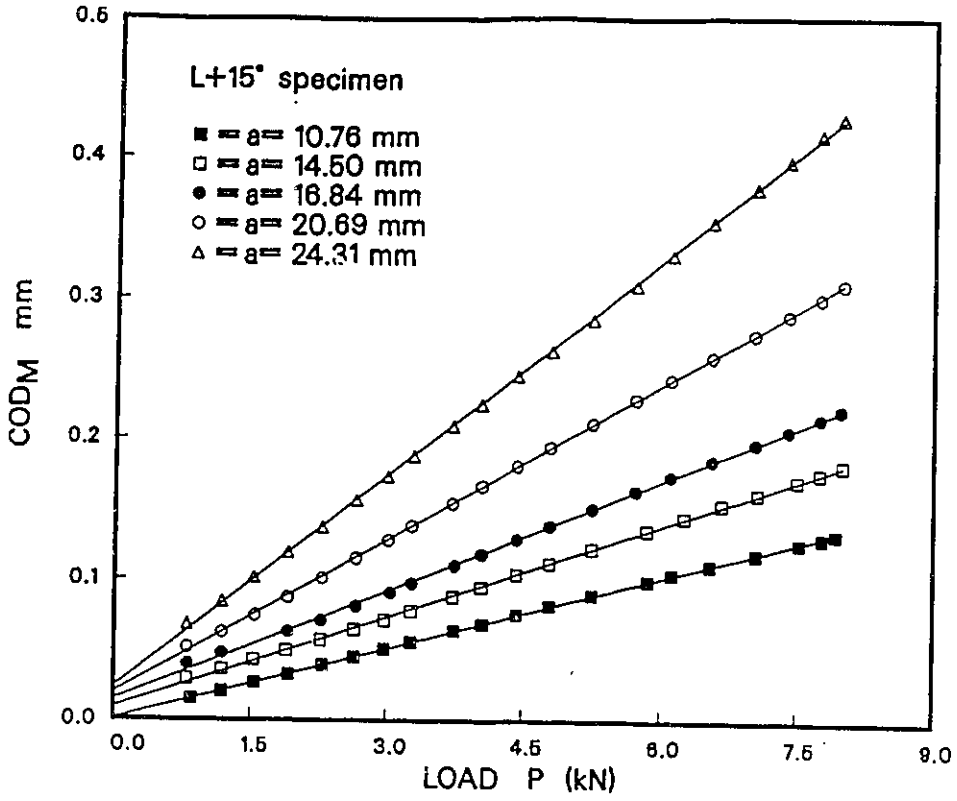
L+15° specimen
■ = a= 10.76 mm
□ = a= 14.50 mm
● = a= 16.84 mm
○ = a= 20.69 mm
△ = a= 24.31 mm
COD_M mm
LOAD P (kN)
0.0
0.1
0.2
0.3
0.4
0.5
1.5
3.0
4.5
6.0
7.5
9.0

b) L+15°;

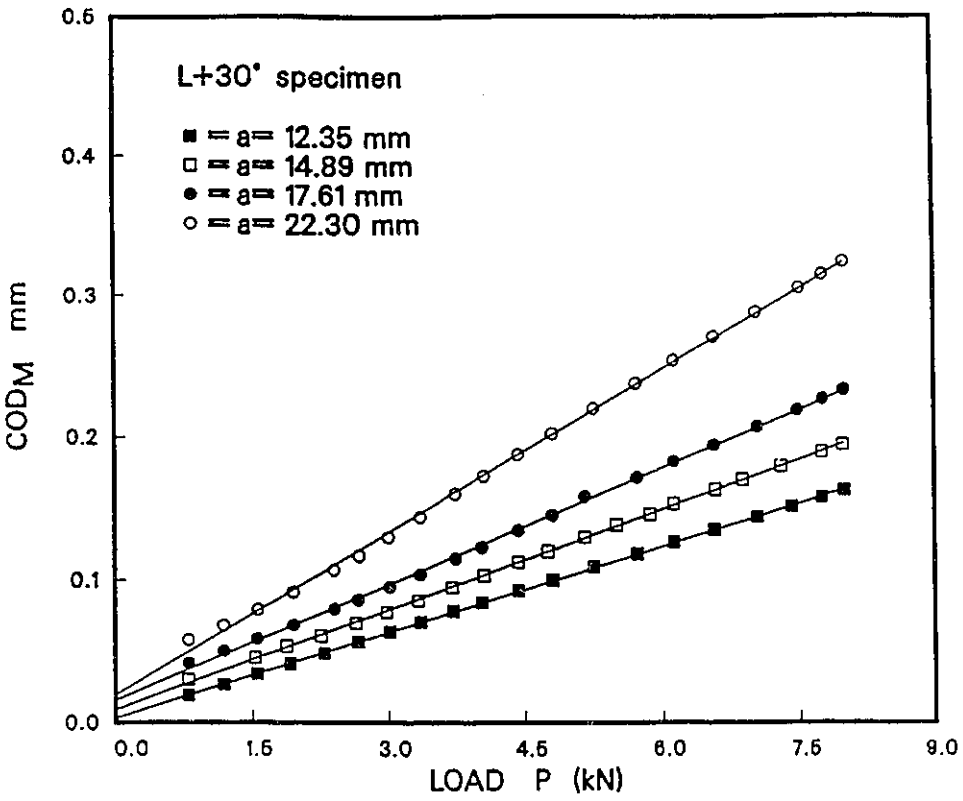
L+30° specimen
■ = a = 12.35 mm
□ = a = 14.89 mm
● = a = 17.61 mm
○ = a = 22.30 mm
COD_M mm
LOAD P (kN)
0.0
0.1
0.2
0.3
0.4
0.6
1.5
3.0
4.5
6.0
7.5
9.0

c) L+30°;

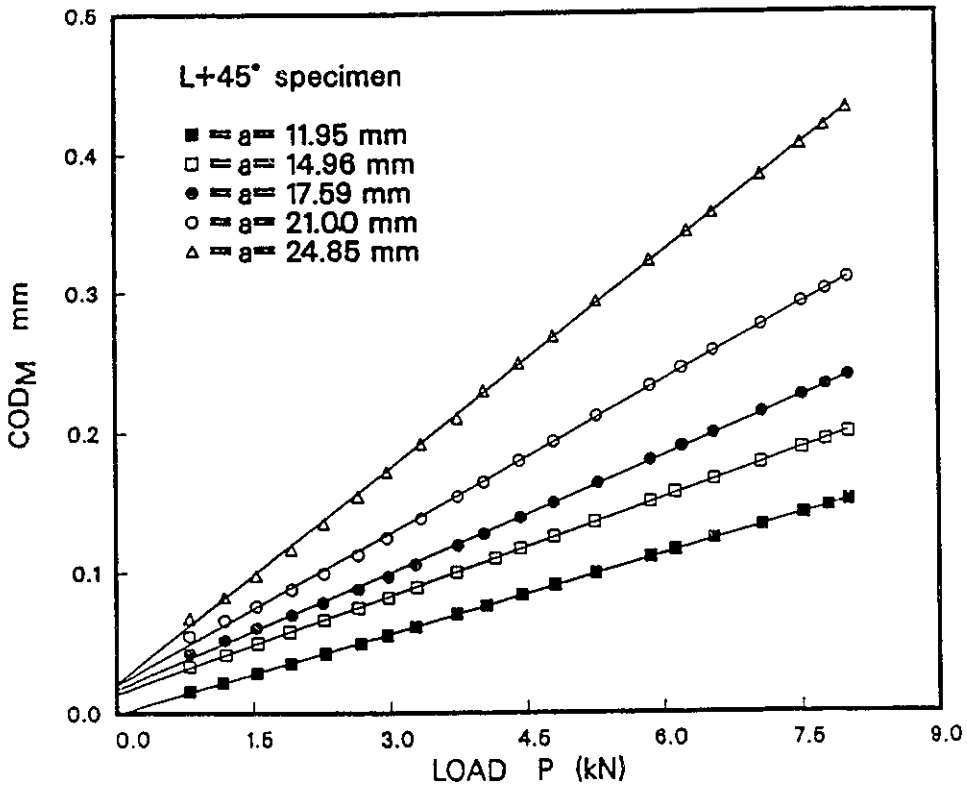

and d) L+45° specimen.

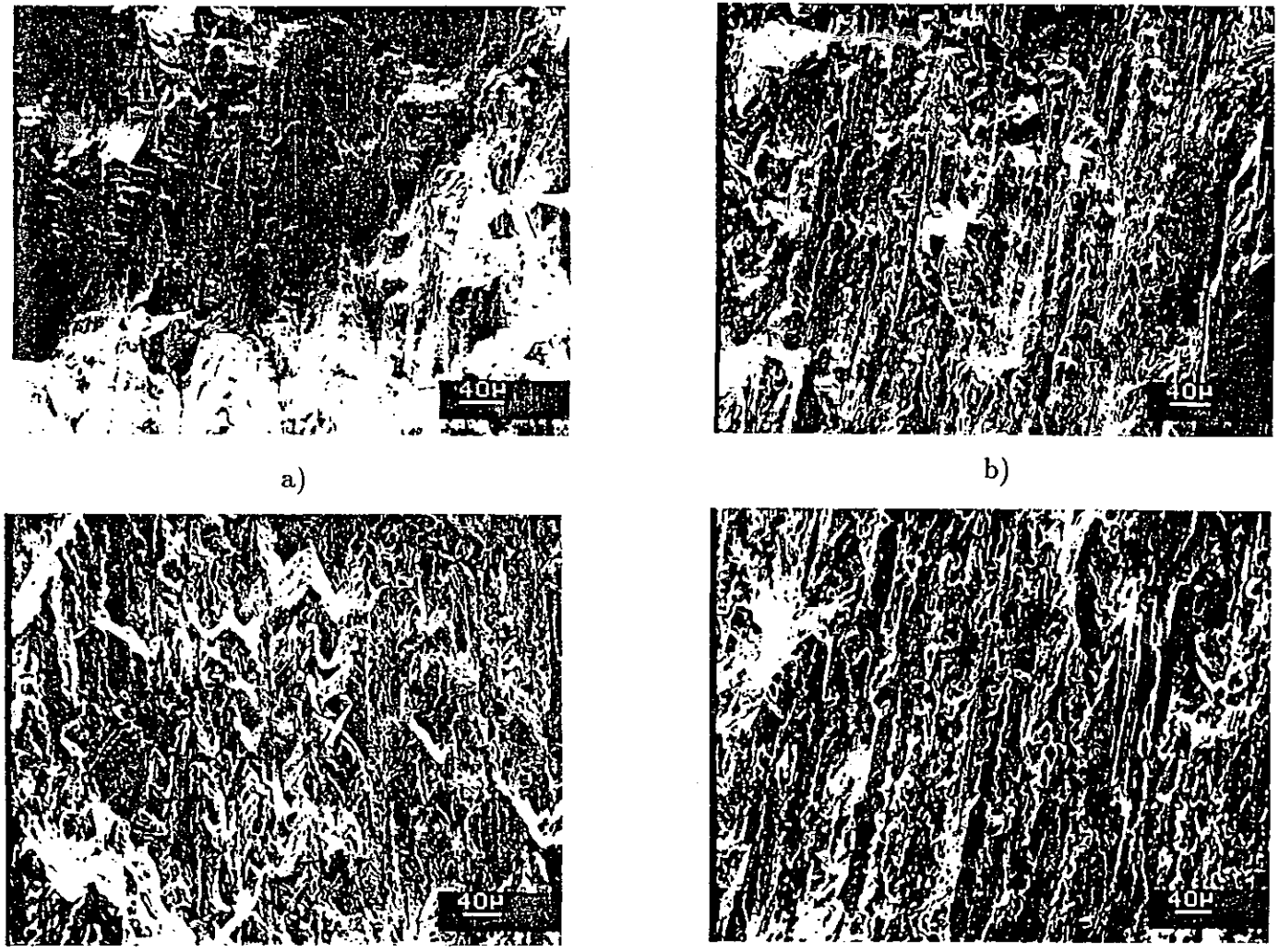

Figure 4.8. Fracture surface morphology for a) LT; b) L+15°; c) L+30°; and d) L+45° specimen.

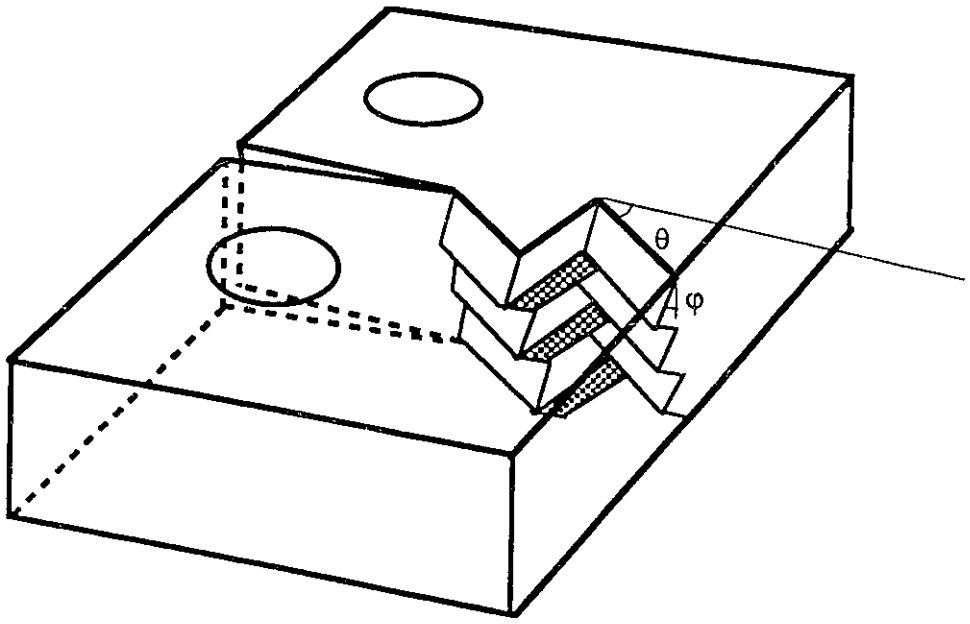

Figure 4.9. A three dimensional view of fatigue crack growth mode in highly textured materials.

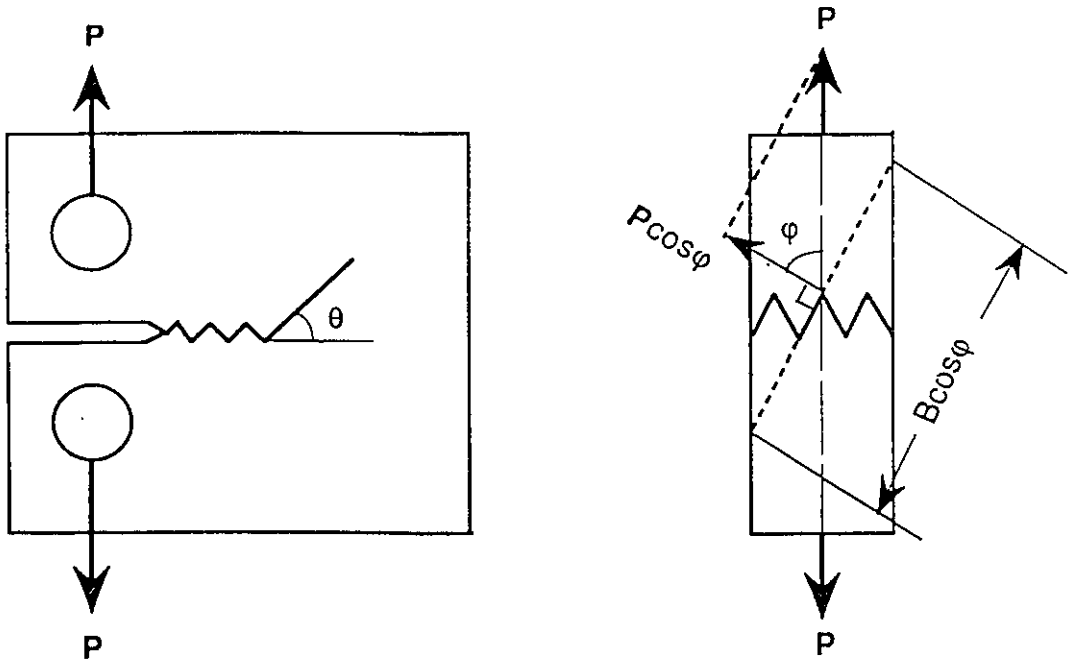

Figure 4.10. Schematic diagram of fatigue crack profiles for Al-Li alloys: a) in C(T) specimen width direction; b) in thickness direction.

Chapter 5

Extension of RSR Model To Environment Assisted Fatigue

5.1 The Slip-Rupture Model

With the presence of a reactive environment, corrosion will affect the material within a localized zone around the crack tip. The corrosion product may accumulate in the form of an oxide film [114] - [116], or hydrogen embrittlement, or dissolution may occur [37,117,118]. The actual process depends on the mechanism of crack growth enhancement, namely, oxide film rupture, active path dissolution or hydrogen embrittlement. For a dissolution mechanism, crack growth is controlled by the combination of transport of the deleterious environment to the crack tip and surface reaction to affect localized dissolution. On the other hand, if hydrogen embrittlement is the dominant mechanism, the internal and external hydrogen diffusion and embrittlement reactions are rate-determining. The corroded material is usually embrittled and may fail by rupture (atomic bond breaking). It will be appreciated that no matter by what mechanism(s) the corrosion damage zone accumulates, it is the rupture of this brittle layer that contributes to crack growth in addition to the component promoted by incomplete slip reversal. Therefore, the characteristic dimension of the corrosion damage, d (which can be either the film thickness or the size of the embrittlement zone), is an important quantity in determining the rate of crack growth in deleterious environments. Incorpo-

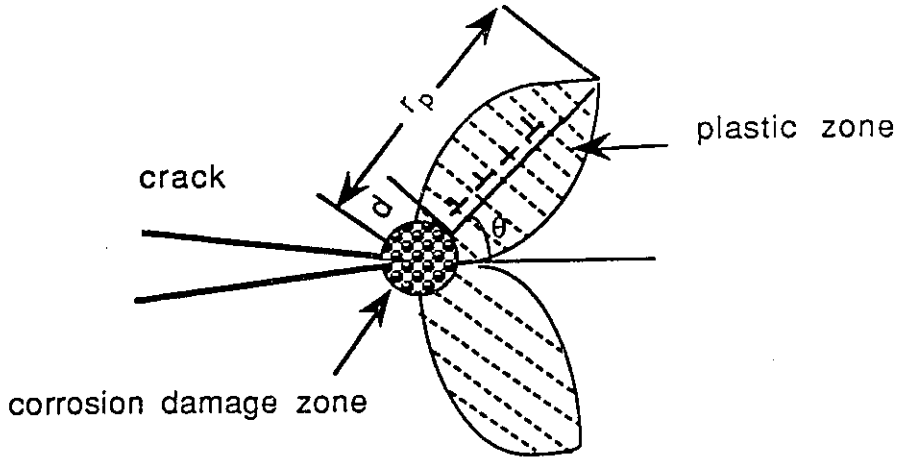

Figure 5.1. The schematic of a corrosion damage zone incorporated in the RSR model.

rating this corrosion-damage zone into the restricted slip reversibility model, as shown schematically in Figure 5.1, a physical description (the slip-rupture model) of general environment assisted fatigue may be obtained as follows.

It has been show in chapter 3 that fatigue crack growth rate, $(da/dN)_m$ (the subscript "m" signifies mechanical fatigue), is related to plastic deformation accommodation ahead of the crack tip by the following relation [90]:

$$\left(\frac{da}{dN}\right)_m = (\gamma_f - \gamma_r) r_p \cos\theta = \frac{(\alpha_f - \alpha_r)\Delta K^3}{12\pi(1-R)VH\sigma_y^2}. \tag{5.1}$$

Considering that the corrosion layer d ruptures during the rising load period, then the crack increment associated with forward slip can be expressed as:

$$\Delta a_f = \left[\frac{d}{1+\varepsilon_c} + \gamma_f(r_p - d)\right]\cos\theta. \tag{5.2}$$

The first term in equation (5.2) is the amount of crack growth due to the rupture of the corrosion damage layer, the factor $1/(1+\varepsilon_c)$ (ε_c is the fracture strain of the corroded material) takes account of the effect of deformation of this layer, the second term is the contribution of the forward slip process. In the decreasing load period, the crack shrinks in association with slip reversal by an amount of

$$\Delta a_r = \gamma_r(r_p - d)\cos\theta. \tag{5.3}$$

Thus, the corrosion fatigue crack growth rate is formulated as

$$\frac{da}{dN} = \Delta a_f - \Delta a_r = \frac{d\cos\theta}{1+\varepsilon_c} + (\gamma_f - \gamma_r)(r_p - d)\cos\theta,$$

which can be rearranged into the form:

$$\frac{da}{dN} = \Delta\gamma\, r_p\cos\theta + \left(\frac{1}{1+\varepsilon_c} - \Delta\gamma\right) d\cos\theta \tag{5.4}$$

where $\Delta\gamma = \gamma_f - \gamma_r$ is the cyclic plastic strain range as depicted by equation (3.17).

5.2 Discussion

According to the slip-rupture model, environment assisted fatigue crack growth rate consists of components, as expressed by equation (5.4). The first term in equation (5.4) is the component of pure mechanical fatigue that results from the restricted slip reversal, as defined by equation (5.1); the second term is the enhancement of crack growth by environmental effects, defined by

$$\left(\frac{da}{dN}\right)_c = \left(\frac{1}{1+\varepsilon_c} - \Delta\gamma\right) d\cos\theta. \tag{5.5}$$

Equation (5.4) has two limiting cases: i) when the reactive environment is absent so that $d = 0$, or the plastic deformation is dominant so that $\Delta\gamma = 1/(1+\varepsilon_c)\cos\theta$, equation (5.4) reduces to equation (5.1) and the crack growth process is purely mechanical fatigue; ii) when corrosion reactions are so active as to prevail through out the plastic zone, that is, $d = r_p$, then

$$\left(\frac{da}{dN}\right)_{CF} = \frac{d\cos\theta}{1+\varepsilon_c} \tag{5.6}$$

which states that the crack growth process is true corrosion fatigue.

For most material-environment systems, crack growth proceeds by the occurrence of both components. Following equation (5.4), environment assisted fatigue crack growth rate, $(da/dN)_e$, can be expressed as

$$\left(\frac{da}{dN}\right)_e = \left(\frac{da}{dN}\right)_m + \left(\frac{da}{dN}\right)_{CF} \xi, \tag{5.7}$$

where $\xi = [1 - \Delta\gamma(1 + \varepsilon_c)]$ is the weight function for corrosion fatigue. Equation (5.7) predicts that corrosion fatigue may predominate in the low or intermediate stress intensity ranges where plastic deformation remains small but the environmental effects will be diminished as ξ approaches 0 (at high stress intensities near K_{IC}). This feature of corrosion fatigue has been established by many experiments and concluded by Ritchie [45]. Figure 5.2 shows the corrosion fatigue behavior of 4130 steel in moist air [119]. Figure 5.3 shows the corrosion fatigue behavior of 4340 M steel in distilled water at different frequencies [26]. Fatigue crack growth behaviors of these two steels in vacua are depicted by equation (5.1), as represented by the dashed lines in Figures 5.2 and 5.3.

Equation (5.7) renders quantitative evaluation of the environmental effects by FCGR testing in a deleterious environment. Since the component of mechanical fatigue, $(da/dN)_m$,

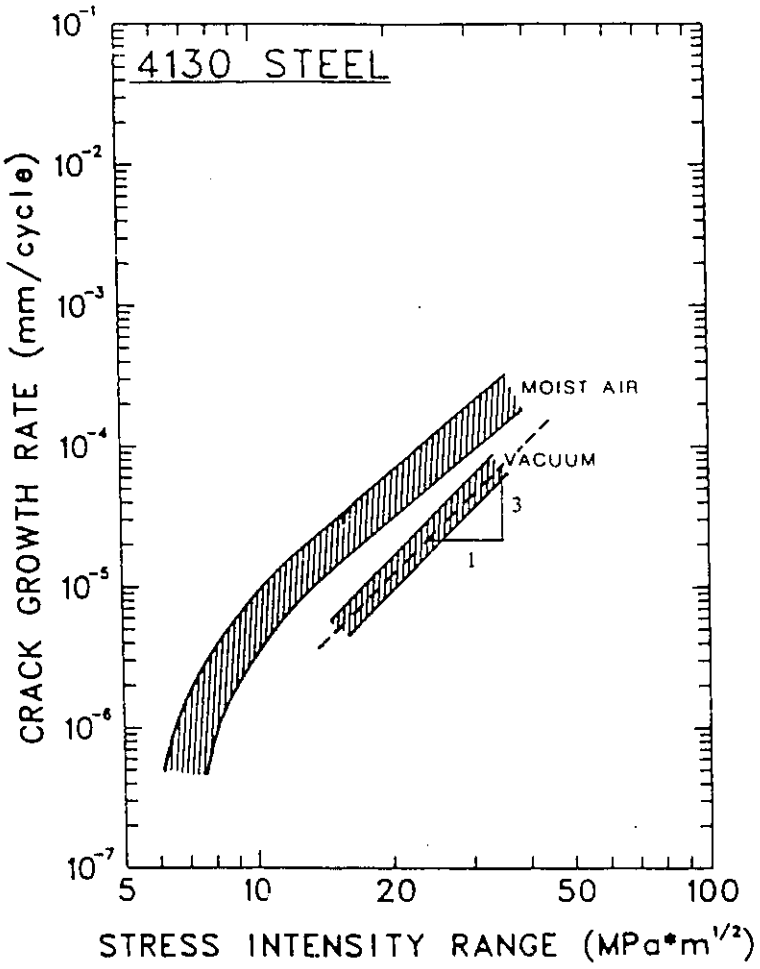

Figure 5.2. Fatigue crack growth behaviors of 4130 steel in vacuum and in moist air [119]. The dashed line represents equation (5.1).

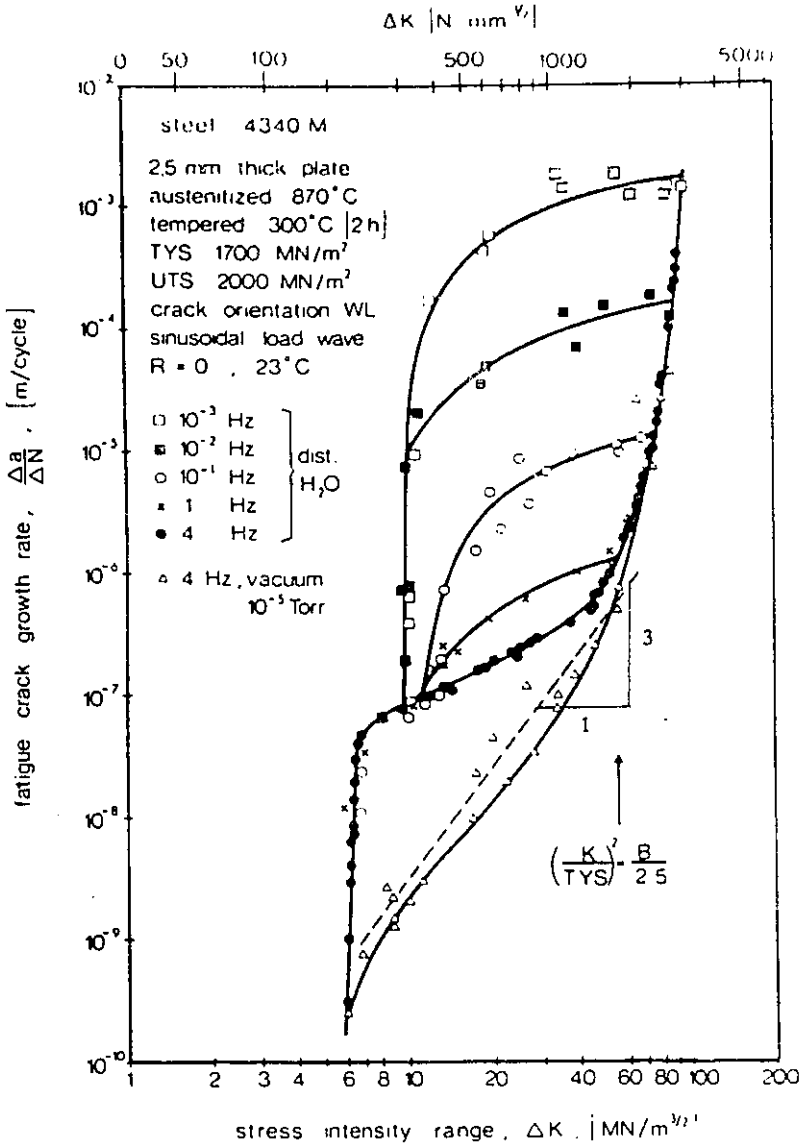

Figure 5.3. Fatigue crack growth behaviors of 4340 M steel in vacuum and distilted water [26]. The dashed line represents equation (5.1).

and the weight function, $\xi = 1 - (1 + \varepsilon_c)\Delta\gamma$ where $\Delta\gamma \cos\theta = (da/dN)_m/r_p$, can be determined in an inert environment, the environmental enhancement of crack growth can be determined by

$$d\cos\theta = \frac{\left(\frac{da}{dN}\right)_e - \left(\frac{da}{dN}\right)_m}{\frac{1}{1+\varepsilon_c} - \frac{1}{r_p}\left(\frac{da}{dN}\right)_m} \tag{5.8}$$

The quantitative determination of the chemistry effects in corrosion fatigue follows the mathematical formulation of reaction kinetics. The corrosion damage zone size, d, being an indicator of how far the reaction goes in the material, depends on the rate of surface reaction, transport/diffusion and embrittlement reactions. Each of these processes is understood to a significant extent [13,15,19,37,117,120], but none fully. Because they are all thermally activated, their individual description and combined effects follow rigorously from the principles of statistical thermodynamics and are integral parts of the framework reported in this thesis. The general constitutive law of corrosion fatigue was derived in the reports [50,51]. Specific chemical processes have to be incorporated in detailed corrosion fatigue models.

Chapter 6

Kinetics of Cross-Over Behavior in Stress Corrosion Cracking

The conventional, usually observed material behavior is increasing crack growth rate with increasing temperature. Occasional observations of unusual material response to temperature effects have also been reported. It was found that near threshold the higher the temperature the slower the crack growth rate [121]-[130]. In the early models of stress corrosion cracking [122,123,125,131,132], it was considered that the crack growth process is controlled by the absorption-desorption of hydrogen at the metal interface. These models over-simplified stress corrosion cracking to a single-energy-barrier controlled process. Based on multi-reaction rate concept, a "hydrogen partitioning" model [133] was proposed to account for hydrogen/microstructure interactions. In these models various mechanisms for the stage II crack growth were suggested, while the stress dependence over the full range of crack growth was not discussed.

It has been shown by Krausz and Krausz [134,135], using a synthesis approach, that the anomalous temperature-dependence behavior can result from the kinetics of atomic bond breaking and healing steps that control the crack growth.

In this chapter, fracture kinetics analysis is extended to the case where a transition from positive to negative temperature dependence results from the kinetics of a two-barrier consecutive system. A constitutive law is then derived for the cross-over behavior of

stress corrosion cracking. Quantitative assessments are applied to some stress corrosion cracking tests. This approach can provide an effective means to control environment assisted fracture.

6.1 Stress Corrosion Cracking

In brittle fracture such as stress corrosion cracking, crack growth may proceed by atomic bond breaking along the crack front, as illustrated in Figure 2.9. Under the combined effects of stress and thermal vibration, atomic bond breaking may occur in succession by thermal activation which results in crack propagation; occasionally, bond healing may also occur to partly close the crack. The crack growth rate is thus controlled by the activation rate times the activation distance na_o (n is the number of activated atoms and a_o is the interatomic distance).

It has been shown that crack growth in Regions I and II of stress corrosion cracking (Figure 2.2) can be represented by a consecutive system with two energy barriers [19,61]. The crack velocity, v, can then be expressed as a combination of rate constants in the form of (equation (2.15))

$$v = \frac{\kappa_{1f}\mathsf{k}_{1f}\kappa_{2f}\mathsf{k}_{2f} - \kappa_{1r}\mathsf{k}_{1r}\kappa_{2r}\mathsf{k}_{2r}}{\kappa_{1f}\mathsf{k}_{1f} + \kappa_{2f}\mathsf{k}_{2f} + \kappa_{1r}\mathsf{k}_{1r} + \kappa_{2r}\mathsf{k}_{2r}} \tag{6.1}$$

where k is the elementary rate constant defined in section 2.3 as

$$\mathsf{k} = \nu \exp\left(-\frac{\Delta G^{\ddagger}(W)}{kT}\right) = \nu \exp\left(-\frac{\Delta G^{\ddagger} \pm \alpha K}{kT}\right), \tag{6.2}$$

the minus sign applies to forward steps (such as bond breaking) denoted by the subscript "f", the plus sign applies to reverse steps (such as bond healing) denoted by the subscript "r"; κ combines the effects of activation distance and concentration of environmental species in a pre-exponential form and, as a first order approximation, is considered to be independent of stress and temperature; $\Delta G^{\ddagger}(W)$ is the apparent activation energy.

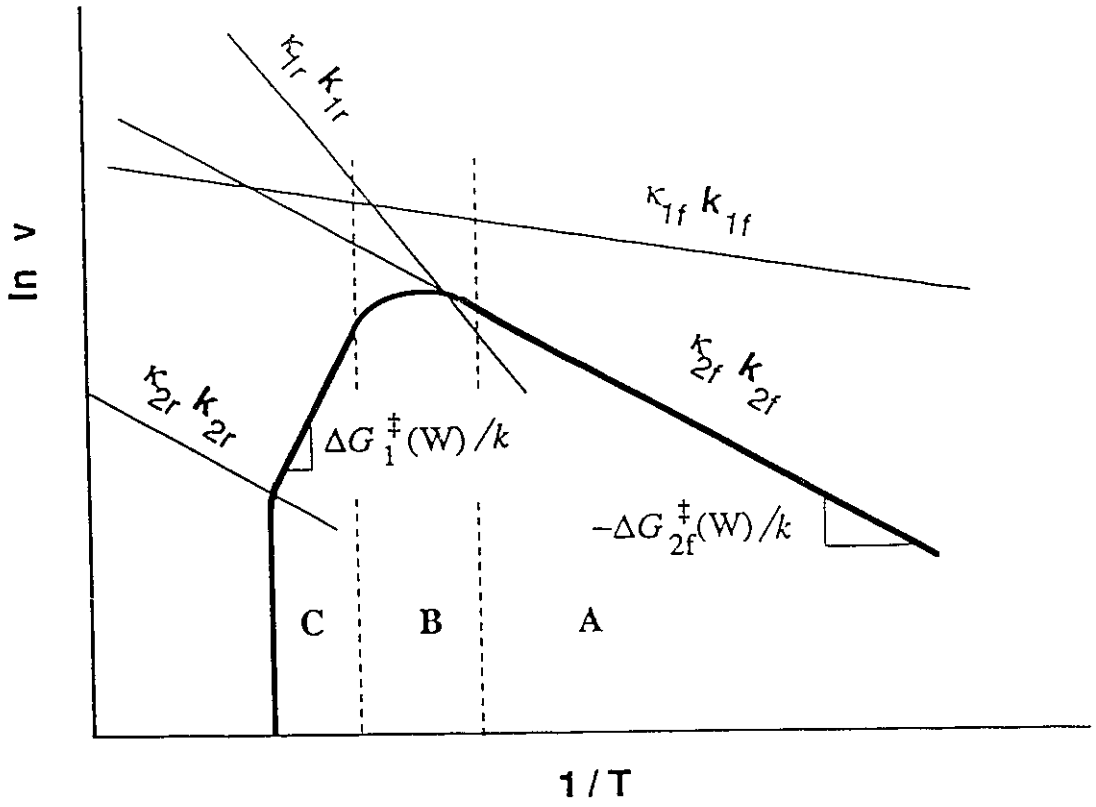

Figure 6.1. Schematic representation of equation (6.1) (heavy curve) and the rate constants (light lines).

6.2 Kinetics of Cross-Over Behavior

In an Arrhenius plot, Figure 6.1, each rate constant is represented by a straight line with the slope of $-\Delta G^{\ddagger}(W)/k$ and the intercept of $\kappa\nu$. The kinetics combination expressed by equation (6.1) results in the behavior represented by the heavy curve in Figure 6.1.

In region A (low temperature range), the fastest step is represented by $\kappa_{1f}\mathrm{k}_{1f}$, while all other rate constants are negligibly small, i.e., $\kappa_{1f}\mathrm{k}_{1f} \gg \kappa_{2f}\mathrm{k}_{2f}, \kappa_{1r}\mathrm{k}_{1r}, \kappa_{2r}\mathrm{k}_{2r}$. Then equation (6.1) reduces to

$$v = \kappa_{2f}\mathrm{k}_{2f} = \kappa_{2f}\nu \exp\left(-\frac{\Delta G_{2f}^{\ddagger}(W)}{kT}\right). \tag{6.3}$$

which coincides with the usual Arrhenius relation.

In region C (high temperature range), one of the healing terms, $\kappa_{1r}\mathsf{k}_{1r}$, is dominant, i.e., $\kappa_{1r}\mathsf{k}_{1r} \gg \kappa_{1f}\mathsf{k}_{1f}, \kappa_{2f}\mathsf{k}_{2f}, \kappa_{2r}\mathsf{k}_{2r}$. Then equation (6.1) reduces to

$$\begin{aligned} v &= \frac{\kappa_{1f}\mathsf{k}_{1f}\kappa_{2f}\mathsf{k}_{2f}}{\kappa_{1r}\mathsf{k}_{1r}} - \kappa_{2r}\mathsf{k}_{2r} \\ &= \kappa_1\nu \exp\left(\frac{\Delta G_1^{\ddagger}(W)}{kT}\right) - \kappa_{2r}\nu \exp\left(-\frac{\Delta G_{2r}^{\ddagger}(W)}{kT}\right) \\ &= \kappa_1\nu^2/\mathsf{k}_1 - \kappa_{2r}\mathsf{k}_{2r} \end{aligned} \tag{6.4}$$

where $\kappa_1 = \kappa_{1f}\kappa_{2f}/\kappa_{1r}$,

$$\mathsf{k}_1 = \nu \exp\left(-\frac{\Delta G_1^{\ddagger}(W)}{kT}\right)$$

and

$$\begin{aligned} \Delta G_1^{\ddagger}(W) &= \Delta G_{1r}^{\ddagger}(W) - \Delta G_{1f}^{\ddagger}(W) - \Delta G_{2f}^{\ddagger}(W) \\ &= (\Delta G_{1r}^{\ddagger} + \alpha_{1r}K) - (\Delta G_{1f}^{\ddagger} - \alpha_{1f}K) - (\Delta G_{2f}^{\ddagger} - \alpha_{2f}K) \\ &= (\Delta G_{1r}^{\ddagger} + \Delta G_{1f}^{\ddagger} + \Delta G_{2f}^{\ddagger}) + (\alpha_{1r} + \alpha_{1f} + \alpha_{2f})K \\ &= \Delta G_1^{\ddagger} + \alpha_1 K. \end{aligned}$$

For the present purpose, we limit our discussion on the condition where $\Delta G^{\ddagger}(W) > 0$. Then, equation (6.4) is represented by the heavy line in region C with a positive slope of $\Delta G_1^{\ddagger}(W)/k$. With increasing temperature, the healing term (or mechanism) $\kappa_{2r}\mathsf{k}_{2r}$ becomes significant, crack growth rate vanishes rapidly when the bond breaking and bond healing steps are balanced.

In conclusion, for an activation system where the sum of $\kappa_{1f}\mathsf{k}_{1f}$ and $\kappa_{1r}\mathsf{k}_{1r}$ is dominant over the full temperature range, as shown in Figure 6.1, equation (6.1) will reduces to

$$v \cong \frac{\kappa_{1f}\mathsf{k}_{1f}\kappa_{2f}\mathsf{k}_{2f} - \kappa_{1r}\mathsf{k}_{1r}\kappa_{2r}\mathsf{k}_{2r}}{\kappa_{1f}\mathsf{k}_{1f} + \kappa_{1r}\mathsf{k}_{1r}}.$$

The healing terms, $\kappa_{1r}\mathsf{k}_{1r}$ and $\kappa_{2r}\mathsf{k}_{2r}$, are negligible at low temperatures (region A), only

the term $\kappa_{2r}\mathsf{k}_{2r}$ will effectively promote crack healing at high temperatures (region C) where $\kappa_{1r}\mathsf{k}_{1r} \gg \kappa_{1f}\mathsf{k}_{1f}$. Then, the above rate equation can be further simplified to

$$\begin{aligned} v &\cong \frac{\kappa_{1f}\mathsf{k}_{1f}\kappa_{2f}\mathsf{k}_{2f}}{\kappa_{1f}\mathsf{k}_{1f} + \kappa_{1r}\mathsf{k}_{1r}} - \kappa_{2r}\mathsf{k}_{2r} \\ &= \left(\frac{\kappa_{1r}\mathsf{k}_{1r}}{\kappa_{1f}\mathsf{k}_{1f}\kappa_{2f}\mathsf{k}_{2f}} + \frac{1}{\kappa_{2f}\mathsf{k}_{2f}}\right)^{-1} - \kappa_{2r}\mathsf{k}_{2r}. \end{aligned}$$

Using the definitions of κ_1 and k_1, the rate equation can be written as

$$v = \left(\frac{\mathsf{k}_1}{\kappa_1 \nu^2} + \frac{1}{\kappa_{2f}\mathsf{k}_{2f}}\right)^{-1} - \kappa_{2r}\mathsf{k}_{2r} \tag{6.5}$$

In region A where $\kappa_1\nu^2/\mathsf{k}_1 \gg \kappa_{2f}\mathsf{k}_{2f}$, equation (6.5) reduces to equation (6.3); in region C where $\kappa_{2f}\mathsf{k}_{2f} \gg \kappa_1\nu^2/\mathsf{k}_1$, equation (6.5) reduces to equation (6.4).

In the transition region B, crack growth is described by equation (6.1) or equivalently equation (6.5). The transition from positive temperature-dependence to negative temperature-dependence occurs at the temperature where crack velocity is the maximum, i.e., at the condition

$$\kappa_1\nu^2/\mathsf{k}_1 = \kappa_{2f}\mathsf{k}_{2f}. \tag{6.6}$$

Substituting the expression of $\Delta G_1^{\ddagger}(W)$ into (6.6), the transition temperature is defined as

$$T_m = \frac{\Delta G_{1r}^{\ddagger}(W) - \Delta G_{1f}^{\ddagger}(W)}{k\ln(\kappa_{1r}/\kappa_{1f})}. \tag{6.7}$$

Example. The crack growth process under consideration is the stress corrosion cracking of AISI 4340 steel (tempered at 200°C) in gaseous hydrogen. The experimentally observed behavior is shown in Figures 6.2 and 6.3 where the symbols represent the crack

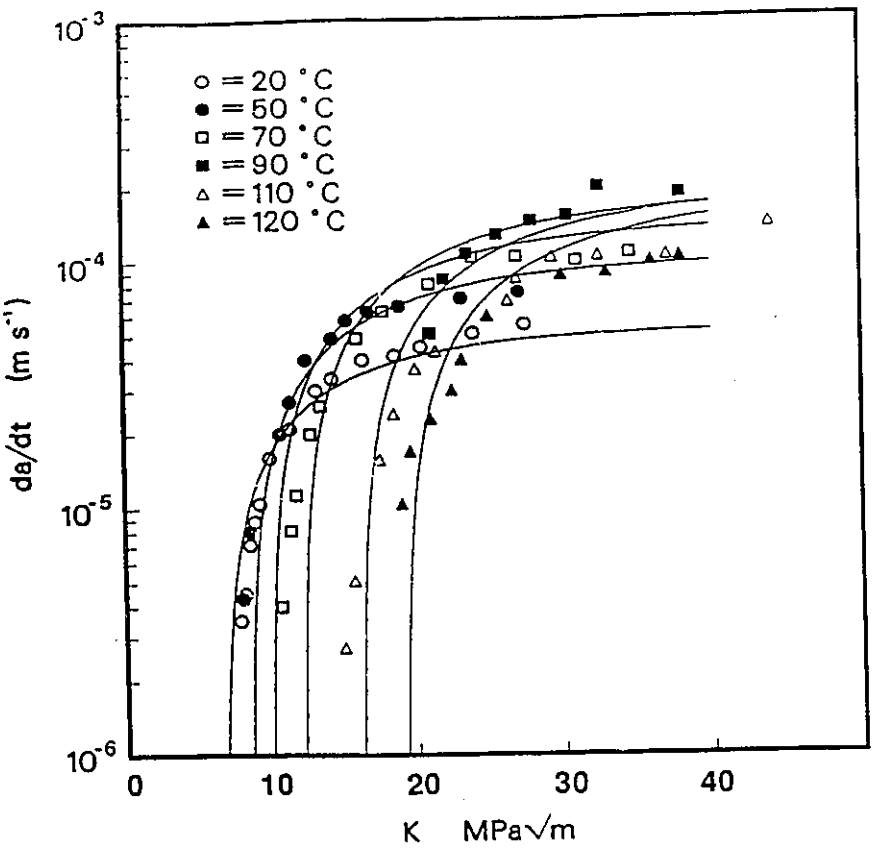

Figure 6.2. Cross-over behavior of stress corrosion cracking in 4340 steel (tempered at 200°C) under hydrogen pressure of 1.1×10^{-1} MPa. Symbols represent the test behavior[129]. The curves were obtained from equation (6.5).

growth rate data [129]. Equation (6.6) is used for the theoretical descriptions (solid lines) using the characteristic activation quantities listed in Table 6.1.

Table 6.1 Activation Parameters for AISI 4340 in Gaseous Hydrogen

subscript	$\Delta G^{\ddagger}$ J	α $m^{5/2}$	$\kappa\nu$ ms^{-1}
1	8.28×10^{-20}	0.0	1×10^{-10}
2f	2.88×10^{-20}	0.0	0.0666
2r	3.35×10^{-20}	4.55×10^{-16}	0.45

Figure 6.2 shows the cross-over pattern of crack growth at stages I and II. Figure 6.3 shows the corresponding positive-negative temperature dependence behavior. Good agreement was found between the theoretical descriptions and experimental results.

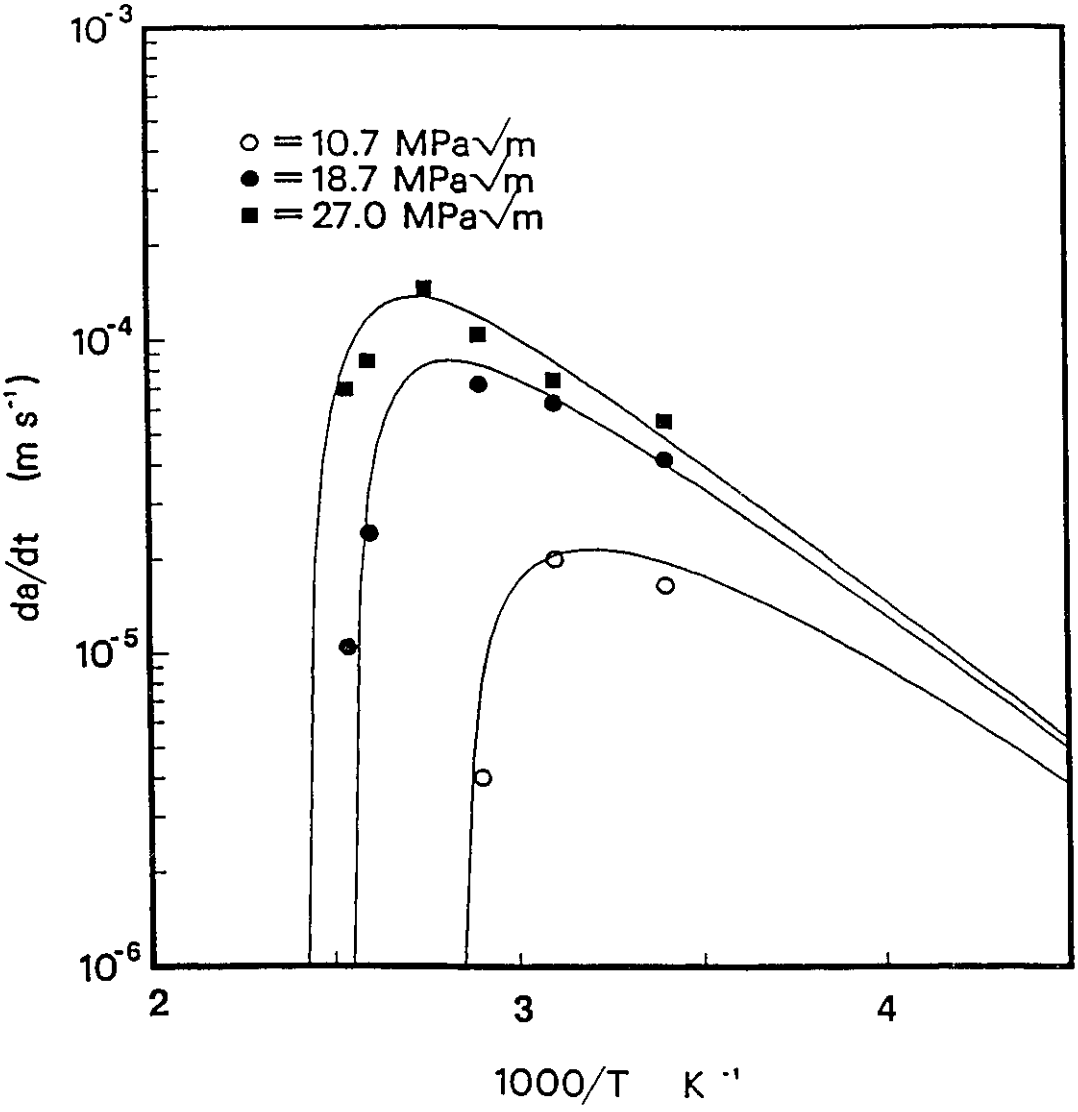

Figure 6.3. The temperature dependence of crack growth represented in Figure 6.2.

Chapter 7

Constitutive Laws of Plastic Deformation

Ashby [3,4] has distinquished five major groups of independent mechanisms by which a polycrystalline material can deform, and yet preserve its crystallinity. The mechanisms involving thermal activation include dislocation movement (dislocation glide and dislocation creep) and vacancy diffusion (Nabarro-Herring creep and Coble creep). In the following, the rate equation for each thermally activated deformation mechanism is derived, which consists of a set of differential equations governing the plastic strain rate and the evolution of the microstructural variables. The operational equations under different loading constraints are obtained by solving the governing differential equations. Neither the shear-collapse process nor twinning will be considered here, although both may lead to important effects in the plastic flow behavior [136].

7.1 Low Temperature Plasticity

7.1.1 The Rate Equation

The mechanism of low temperature plastic deformation (in the range of $T < 0.3T_m$, where T_m is the melting point) is controlled predominantly by the conservation motion

of dislocations–dislocation glide [71,72]. Dislocation glide occurs by thermal activation over the rate-controlling obstacles in its slip plane. These obstacles, following Dorn [139], may be classified as either linear or localized. Linear obstacles occur in, for example, the Peierls-Nabarro mechanism [140]-[144]. Localized obstacles result from the various kinds of point defects, and in the cutting of forest dislocations [4,145]. It has been shown that the plastic strain rate represents the net activation rate over a single energy barrier [15].

Combining equation (2.4) and (2.11), the plastic strain rate is expressed as [15]:

$$\dot{\gamma}_p = A_f \exp\left(\frac{V_f \tau}{kT}\right) - A_r \exp\left(-\frac{V_r \tau}{kT}\right) \tag{7.1}$$

where

$$A_f = \nu b l_f \rho_f \exp\left(-\frac{\Delta G_f^{\ddagger}}{kT}\right) \quad \text{and} \quad A_r = \nu b l_r \rho_r \exp\left(-\frac{\Delta G_r^{\ddagger}}{kT}\right).$$

Equation (7.1) has been widely used for the description of plastic deformation [15,147-150]. It expresses the most general condition that

- the dislocation density ρ,
- the activation energy $\Delta G^{\ddagger}$,
- the activation volume V

may not be the same in the forward and in the reverse direction. The rate constants, A_f and A_r usually vary with stress because the dislocation density changes during deformation [151,152]. Dislocation multiplication can affect significantly the yield drop and the time-delay of creep in low activation energy materials such as Ge, LiF, ice and even in mild steels [15,152]. In high strength alloys the activation energy is large and the stress dependence of the exponential function is so large that the effect of the change in the pre-exponential term can be neglected and A_f and A_r can be considered to be independent of the stress. Under various conditions equation (7.1) can be further simplified. In particular, for symmetrical barriers the rate equation reduces to a sinh type relation [147-150].

The empirical relation [153,154]:

$$\dot{\gamma}_p = A' \sinh^n \beta\tau \tag{7.2}$$

was proposed a very long time ago and is still used extensively for the kinetics equation of the constitutive law. In (7.2) A', β and n are experimental constants. Equation (7.2) appears to be a reasonably good description of the behavior exhibited in many tests, however, being an empirical expression its validity can not be assumed outside the actually tested range. This limits its application severely. Because the deformation kinetics rate equation (7.1) is physically based and rigorously derived it can be used for extrapolation with confidence and for the physical description of the parameters of the $\sinh^n$ relation (7.2). Equating (7.1) and (7.2) gives

$$\dot{\gamma}_p = A' \sinh^n \beta\tau = A' \left[\frac{\exp(\beta\tau) - \exp(-\beta\tau)}{2}\right]^n = A_f \exp\left(\frac{V_f\tau}{kT}\right) - A_r \exp\left(-\frac{V_r\tau}{kT}\right). \tag{7.3}$$

At high stresses the reverse term $A_r \exp\left(-\frac{V_r\tau}{kT}\right)$ and $\exp(-\beta\tau)$ are negligible, i.e.,

$$\frac{A'}{2^n} \exp[n\beta\tau] = A_f \exp\left(\frac{V_f\tau}{kT}\right),$$

from this it follows that

$$A' = 2^n A_f \quad \text{and} \quad n\beta = \frac{V_f}{kT}. \tag{7.4}$$

At low stresses (when $\beta\tau \ll 1$) the sinh term in equation (7.3) reduces to a power law function

$$A'\beta^n\tau^n = A_f \exp\left(\frac{V_f\tau}{kT}\right) - A_r \exp\left(-\frac{V_r\tau}{kT}\right). \tag{7.5}$$

From (7.5) the exponent is

$$n = \frac{d\ln\dot{\gamma}_p}{d\ln\tau} = \frac{\frac{A_fV_f\tau}{kT}\exp\left(\frac{V_f\tau}{kT}\right) + \frac{A_rV_r\tau}{kT}\exp\left(-\frac{V_r\tau}{kT}\right)}{A_f\exp\left(\frac{V_f\tau}{kT}\right) - A_r\exp\left(-\frac{V_r\tau}{kT}\right)}. \tag{7.6}$$

and from equations (7.4) and (7.6), β is defined as

$$\beta = \frac{V_f}{nkT} = \frac{1}{\tau}\left[\frac{1 - \frac{A_r}{A_f}\exp\left(-\frac{(V_f+V_r)\tau}{kT}\right)}{1 + \frac{A_r V_r}{A_f V_f}\exp\left(-\frac{(V_f+V_r)\tau}{kT}\right)}\right]. \tag{7.7}$$

Equations (7.4), (7.6) and (7.7) define A', β and n in terms of rigorously derived physical quantities: the $\dot{\gamma}_p = A' \sinh^n \beta\tau$ relation is now equivalent to the physically based rate equation (7.1) and describes the plastic strain rate well.

In applications the integration of equation (7.1) and (7.2) may be inconvenient when the internal stress, and hence the effective stress, changes with deformation in low-temperature deformation. For the economical evaluation of test results and for the design of components a constitutive law that incorporates the rigorousness of the deformation kinetics rate equation and the simplicity of the empirical form of the hyperbolic sine model expressed with physically defined parameters is of advantage. To obtain this form equations (7.1), (7.2), (7.5), (7.6) and (7.7) are combined to

$$\dot{\gamma}_p = A_f \exp\left(\frac{V_f\tau}{kT}\right) - A'_r \exp\left(-\frac{V_f\tau}{kT}\right). \tag{7.8}$$

Equation (7.8) is in formal agreement with the rigorously derived rate equation (7.1) at the condition that the work is the same in forward and reverse activations. In equation (7.8) A'_r is an activation parameter which can be determined by expressing the threshold condition $\dot{\gamma}_p = 0$ from equations (7.1) and (7.8)

$$\tau_{th} = \frac{kT}{V_f + V_r}\ln\frac{A_r}{A_f} = \frac{kT}{2V_f}\ln\frac{A'_r}{A_f}. \tag{7.9}$$

From this it follows that

$$A'_r = A_f\left(\frac{A_r}{A_f}\right)^{\frac{2V_f}{V_f+V_r}}.$$

In the high strain rate range the reverse rate terms are negligible and equations (7.1)

and (7.8) are identical. In the low range the difference between the two is

$$\begin{aligned}
\frac{\Delta\dot{\gamma}_p}{\dot{\gamma}_p} &= \frac{A_r' \exp\left(-\frac{V_f\tau}{kT}\right) - A_r \exp\left(-\frac{V_r\tau}{kT}\right)}{A_f \exp\left(\frac{V_f\tau}{kT}\right) - A_r \exp\left(-\frac{V_r\tau}{kT}\right)} \\
&= \frac{A_f \exp\left(-\frac{V_f(\tau-2\tau_{th})}{kT}\right) - A_r \exp\left(-\frac{V_r\tau}{kT}\right)}{A_f \exp\left(\frac{V_f\tau}{kT}\right) - A_r \exp\left(-\frac{V_r\tau}{kT}\right)} \\
&= \frac{A_f \exp\left(\frac{V_f\tau_{th}}{kT}\right) - A_r \exp\left(-\frac{V_r\tau_{th}}{kT}\right) \exp\left(\frac{(V_f-V_r)(\tau-\tau_{th})}{kT}\right)}{A_f \exp\left(\frac{V_f\tau}{kT}\right) - A_r \exp\left(-\frac{V_r\tau}{kT}\right)} \exp\left(-\frac{V_f(\tau-\tau_{th})}{kT}\right).
\end{aligned}$$

where $\Delta\dot{\gamma}_p$ represents the difference between equations (7.1) and (7.8).

Typically for $|V_r - V_f| < 10\,b^3$ (the lower limit for Peierls-Nabarro mechanism [15]), $\tau - \tau_{th} < 30$ MPa (about one third of Orowan stress, which characterizes the threshold condition [4]) and $T = 300$K,

$$\exp\left(-\frac{(V_r - V_f)(\tau - \tau_{th})}{kT}\right) \approx 1 - \frac{(V_r - V_f)(\tau - \tau_{th})}{kT},$$

the error reduces to (the condition $\dot{\gamma}_p = 0$ at $\tau = \tau_{th}$ has been used):

$$\begin{aligned}
\frac{|\Delta\dot{\gamma}_p|}{\dot{\gamma}_p} &= \frac{\frac{|V_r-V_f|(\tau-\tau_{th})}{kT} A_r \exp\left(-\frac{V_r\tau_{th}}{kT}\right) \exp\left(-\frac{V_f(\tau-\tau_{th})}{kT}\right)}{A_f \exp\left(\frac{V_f\tau}{kT}\right) - A_r \exp\left(-\frac{V_r\tau}{kT}\right)} \\
&= \frac{\frac{|V_r-V_f|(\tau-\tau_{th})}{kT} \exp\left(-\frac{V_f(\tau-\tau_{th})}{kT}\right)}{\exp\left(\frac{V_f(\tau-\tau_{th})}{kT}\right) - \exp\left(-\frac{V_r(\tau-\tau_{th})}{kT}\right)}
\end{aligned}$$

which approaches to $|V_r - V_f|/(V_r + V_f) < 1$ as $\tau \hookrightarrow \tau_{th}$ and diminishes rapidly with increasing stress. Because in the threshold region strain rate measurements have a scatter factor of about 4, equation (7.8) is a good approximation of the general equation (7.1) within the specified error range. Figure 7.1 illustrates the strain rate defined by equations (7.1) and (7.8) together with the empirical equation (7.2) measured in an

Al-Mg alloy [153]. All curves fall within the ±2 band that envelopes the experimental data.

Letting $V_f = V_r = V$, both equation (7.1) and equation (7.8) become

$$\dot{\gamma}_p = \sqrt{A_f A_r}\left[\exp\left(\frac{V(\tau - \tau_{th})}{kT}\right) - \exp\left(-\frac{V(\tau - \tau_{th})}{kT}\right)\right]$$

which can be expressed as a hyperbolic sine function:

$$\dot{\gamma}_p = 2A \sinh \frac{V(\tau - \tau_{th})}{kT} \tag{7.10}$$

where

$$A = \sqrt{A_f A_r} = b\nu\sqrt{l_f l_r \rho_f \rho_r}\exp\left(-\frac{\Delta G_f^{\ddagger} + \Delta G_r^{\ddagger}}{2kT}\right).$$

During deformation polycrystalline materials often undergo work hardening. For small strains [152] the effective stress can be expressed as

$$\tau_{eff} = \tau - \tau_i = \tau - H\gamma - \tau_{i0}. \tag{7.11}$$

where τ_i is the internal stress, τ_{i0} is the initial internal stress and H is the work hardening coefficient.

Substituting the effective stress from equation (7.11) into (7.10) the rate equation is

$$\dot{\gamma}_p = 2A \sinh \frac{V(\tau - H\gamma_p - \tau_0)}{kT} \tag{7.12}$$

where

$$\tau_0 = \tau_{i0} + \tau_{th} = \tau_{i0} + \frac{kT}{2V}\ln\frac{A_r}{A_f}. \tag{7.13}$$

7.1.2 Operational Equations

Define an energy function Φ as

$$\Phi = \frac{V}{kT}(\tau - H\gamma_p - \tau_0). \tag{7.14}$$

By definition Φ is the effective activation work normalized with thermal energy content kT. Because the activation parameters (A_f, A_r, V, τ_{i0}) and the work hardening coefficient H are microstructural quantities the function Φ depends on the current stress, the accumulated plastic strain andthe temperature. The evolution of function Φ controls the deformation response. For an isothermal process, the small-strain deformation is governed by

$$\dot{\gamma} = \frac{\dot{\tau}}{\mu} + \dot{\gamma}_p, \tag{7.15}$$

$$\dot{\gamma}_p = 2A \sinh \Phi, \tag{7.16}$$

$$\dot{\Phi} = \frac{V}{kT}(\dot{\tau} - H\dot{\gamma}_p). \tag{7.17}$$

$\gamma = \gamma_e + \gamma_p$ where $\gamma_e = \tau/\mu$ (μ is the shear modulus) is the elastic strain, and γ_p is the plastic strain. The shear strain, γ, can be converted to the normal strain ϵ with the relation [4] $\epsilon = \gamma/\sqrt{3}$ and the shear stress τ can be converted to the normal stress σ with [4] $\sigma = \sqrt{3}\tau$.

By imposing the loading constraint the evolutionary equation (7.16) and (7.17) can be solved to yield the operational equation that describes

- stress-strain
- stress-time
- strain-time

response.

Constant Strain Rate Loading.

At constant strain rate, equation (7.15).

$$\dot{\tau} = \mu(\dot{\gamma} - \dot{\gamma}_p).$$

Substituting this and the rate equation (7.16) into (7.17):

$$\dot{\Phi} = \frac{V\mu\dot{\gamma}}{kT}\left[1 - \left(1 + \frac{H}{\mu}\right)\frac{2A}{\dot{\gamma}}\sinh\Phi\right]. \tag{7.18}$$

Equation (7.18) can be integrated to

$$\frac{u-a}{\chi u+b} = \frac{1-a}{\chi+b}\exp\left(-\frac{V\mu\dot{\gamma}\sqrt{1+\chi^2}t}{kT}\right) \tag{7.19}$$

where

$$\chi = \frac{2A}{\dot{\gamma}}(1+\frac{H}{\mu}),\ a = \frac{\sqrt{1+\chi^2}-1}{\chi},\ b = \frac{\sqrt{1+\chi^2}+1}{2}$$

and

$$u = \exp -\Phi.$$

After a short elastic-plastic transient Φ reaches a steady value of

$$\Phi_s = \frac{V}{kT}(\tau - H\gamma_p - \tau_0) = -\ln\frac{\sqrt{1+\chi^2}-1}{\chi} \tag{7.20}$$

Equation (7.20) describes the stress-strain response in the range of plastic deformation. By back-extrapolation the yield stress can be obtained at $\gamma_p = 0$ as

$$\tau_y = \tau_0 - \frac{kT}{V}\ln\frac{\sqrt{1+\chi^2}-1}{\chi}. \tag{7.21}$$

For more complicated yielding behavior, e.g. for yield drop phenomena, a dislocation multiplication model has to be incorporated into the kinetics description [15,152]. In that case, the differential equation (7.18) has to be solved numerically.

Stress Relaxation

In stress relaxation, the total strain is held at a constant value so that

$$\dot{\gamma} = \frac{\dot{\tau}}{\mu} + \dot{\gamma}_p = 0.$$

Equation (7.17) then reduces to

$$\dot{\Phi} = -\frac{V(\mu + H)}{kT}\dot{\gamma}_p = -\frac{2V(\mu + H)A}{kT}\sinh\Phi \tag{7.22}$$

which can be integrated to the form

$$\tanh(\frac{\Phi}{2}) = \tanh(\frac{\Phi_o}{2})\exp\left(-\frac{2V(\mu + H)At}{kT}\right). \tag{7.23}$$

From this the stress variation in stress relaxation can be expressed as

$$\tau = \tau_i + \frac{2kT}{V}\tanh^{-1}\left[\tanh(\frac{\Phi_o}{2})\exp\left(-\frac{2V(\mu + H)At}{kT}\right)\right]. \tag{7.24}$$

Constant Stress Rate Loading and Ratchetting

Consider a triangular-wave loading profile shown in Figure 7.2 where t_s represents the starting time of plastic flow and t_f the final time of plastic flow, both satisfying the condition $\Phi = 0$.

(i) In the loading period ($t_s \leq t \leq t_R$)

$$\dot{\Phi} = \frac{V}{kT}(\dot{\tau} - H\dot{\gamma}_p) = \frac{V\dot{\tau}}{kT}\left(1 - \frac{2AH}{\dot{\tau}}\sinh\Phi\right). \tag{7.25}$$

which can be integrated to

$$\frac{u - p}{\lambda u + q} = \frac{1 - p}{\lambda + q}\exp\left(-\frac{V\dot{\tau}\sqrt{1 + \lambda^2}(t - t_s)}{kT}\right) \tag{7.26}$$

where

$$\lambda = \frac{2AH}{\dot{\tau}},\ p = \frac{\sqrt{1 + \lambda^2} - 1}{\lambda},\ q = \frac{\sqrt{1 + \lambda^2} + 1}{2}.$$

$$u = \exp -\Phi.$$

(ii) In the unloading period ($t_R \leq t \leq t_f$),

$$\dot{\Phi} = -\frac{V}{kT}(\dot{\tau} + H\dot{\gamma}_p) = -\frac{V\dot{\tau}}{kT}\left(1 + \frac{2AH}{\dot{\tau}}\sinh\Phi\right). \tag{7.27}$$

which can be integrated to

$$\frac{u+p}{q-\lambda u} = \frac{u_R+p}{q-\lambda u_R}\exp\left(-\frac{V\dot{\tau}\sqrt{1+\lambda^2}(t_R-t)}{kT}\right) \tag{7.28}$$

where $u_R = \exp -\Phi(t_R)$ is determined by (7.26) at $t = t_R$.

In stress controlled cycling materials often exhibit ratchetting behavior in which the plastic strain accumulates progressively. The small amount of plastic strain that is not reversed in the cycles may lead to unacceptably large accumulated strains. For this condition equations (7.26) and (7.28) provide a set of iterative equations which express the accumulated plastic strain. Although equations (7.26) and (7.28) are derived for zero-to-tension loading case they are also valid for loading with a positive stress ratio ($R = \tau_{min}/\tau_{max}$) provided the minimum stress does not exceed τ_0.

At low temperatures λ is small and then equations (7.26) and (7.28) can be combined in a differential form (see Appendix D for detail):

$$\begin{aligned} \frac{d\gamma_p}{dN} &= \frac{kT}{VH}\left[\Phi + \ln\left(\frac{2AH}{\dot{\tau}} + \exp(-\Phi)\right)\right], \\ \Phi &= \frac{V}{kT}(\tau_{max} - H\gamma_p - \tau_0). \end{aligned} \tag{7.29}$$

Creep

In creep $\dot{\tau} = 0$ and equation (7.17) reduces to

$$\dot{\Phi} = -\frac{VH}{kT}\dot{\gamma}_p = -\frac{2VHA}{kT}\sinh\Phi \tag{7.30}$$

which can be integrated to

$$\tanh(\frac{\Phi}{2}) = \tanh(\frac{\Phi_0}{2}) \exp\left(-\frac{2VHAt}{kT}\right). \tag{7.31}$$

7.1.3 Comparison and Discussion

Plastic deformation is always rate and temperature dependent – it is thermally activated [155-158]. Analyses of experimental results obtained in tensile tests demonstrate that equation (7.19) and (7.20) represent the behavior well over a wide strain rate and temperature range. Figure 7.3 represents the behavior of 304 stainless steel at three strain rates [155] and Figure 7.4 shows the effect of temperature on the stress-strain relation in 8660 steel [158]. The variation of yield stress with strain rate and temperature is shown in Figure 7.5. The good agreement with the constitutive law is noted.

The behavior in stress relaxation is expressed with equation (7.23). Stress relaxation tests provide a method for the determination of the internal stress. As shown by equation (7.24), τ_i is the stress level at the end of stress relaxation. The stress relaxation of a 1100 aluminum alloy was analyzed by Wilson and Garofalo [147,148] using a kinetic equation similar to (7.24) for a symmetrical barrier. Their results are shown in Figure 7.6.

Creep was also analyzed. Equation (7.31) shows that the initial value of Φ controls the subsequent creep: it depends on the stress, temperature, and the initial strain. Figure 7.7 shows the creep behaviors of Type 304 stainless steel at three stress levels. Very good agreement is found between the theoretical description (7.25) and the observed behavior.

The validity of the deformation kinetics model can be further verified by a simulated test on Type 304 stainless steel in comparison with the actual experiments of Ruggles and Krempl [159]. The imposed loading sequence (History I) are: OA–strain controlled loading to $\epsilon = 1$ percent with strain rate $\dot{\epsilon} = 8.33 \times 10^{-4} s^{-1}$, AD– stress controlled cycling (1000 cycles) with a rise time of 2 sec., DE–creep for 700 sec., FG–strain controlled loading to ϵ_F+1% strain and HI–one cycle of stress controlled cycling (2100 sec.). These processes are described by equations (7.19), (7.26) (7.28), (7.29) and (7.31) with material constants and activation parameters as listed in TABLE 7.1. The measured behavior is shown in Figure 7.8(a) and the calculated stress-strain response in Figure 7.8(b). The measured and calculated behavior is also given in TABLE 7.2 Excellent agreement was found between the theoretical description and the experiment.

In stress controlled cycling materials often exhibit significantly rate dependent ratchetting behavior [159]. The classical treatment applies either time-independent plasticity or plasticity [160]. Equation (7.29) provides a theoretical description developed from deformation kinetics theory; it expresses the strain increment per cycle ($d\gamma/dN$) explicitly in terms of stress, temperature and loading rate. Figure 7.9 shows the comparisons of equation (7.29) with the observed behavior and a power-law model [160]. It is obvious that deformation kinetics theory provides a good description of ratchetting.

7.2 Dislocation Creep

7.2.1 The Rate Equation

At high temperatures in the range of 0.3–0.6T_m, atoms possess higher thermal energy so that dislocation movement acquires a new degree of freedom—climb. The climb step releases the gliding dislocation in front of an obstacle, allowing it to glide continuously on another crystallographic plane until it meets another obstacle where the process is repeated. The mechanism based on this climb-plus-glide sequence is referred as climb-controlled creep [161,162,163]. The process can be represented by a consecutive system with two energy barriers (Figure 7.10): barrier I represents gliding and barrier II represents climbing. In this activation system, climbing, as a new degree of freedom of

TABLE 7.1 Material Constants and Activation Parameters for 304 stainless steel

material constants	value	unit
μ	5766.4	(MPa)
H	718.33	(MPa)
$V/\sqrt{3}$	1.213×10^{-21}	(cm^3)
$A/\sqrt{3}$	5.08×10^{-9}	(sec^{-1})
$\sqrt{3}\tau_0$	157.5	(MPa)

TABLE 7.2 Comparison of Calculations and Measurements

mechanical quantities	test	calculation	test	calculation
t_R (s)	2	2	210	210
σ_A(MPa)	217	219	209	219
ϵ_{RAT}(%)	0.561	0.575	1.139	1.286
ϵ_{CR}(%)	0.365	0.386	0.018	0.016
ϵ_F(%)	1.810	1.834	2.039	2.176
σ_G(MPa)	257	258.5	256	258
ϵ_{SC}(%)	0.702	0.6	0.847	0.733

σ_A – stress at point A;

σ_G – stress at point G;

ϵ_{RAT} – rachet strain accumulated from point B to C;

ϵ_{CR} – creep strain in DE;

ϵ_F – plastic strain at point G;

ϵ_{SC} – plastic strain produced by load sequence HI.

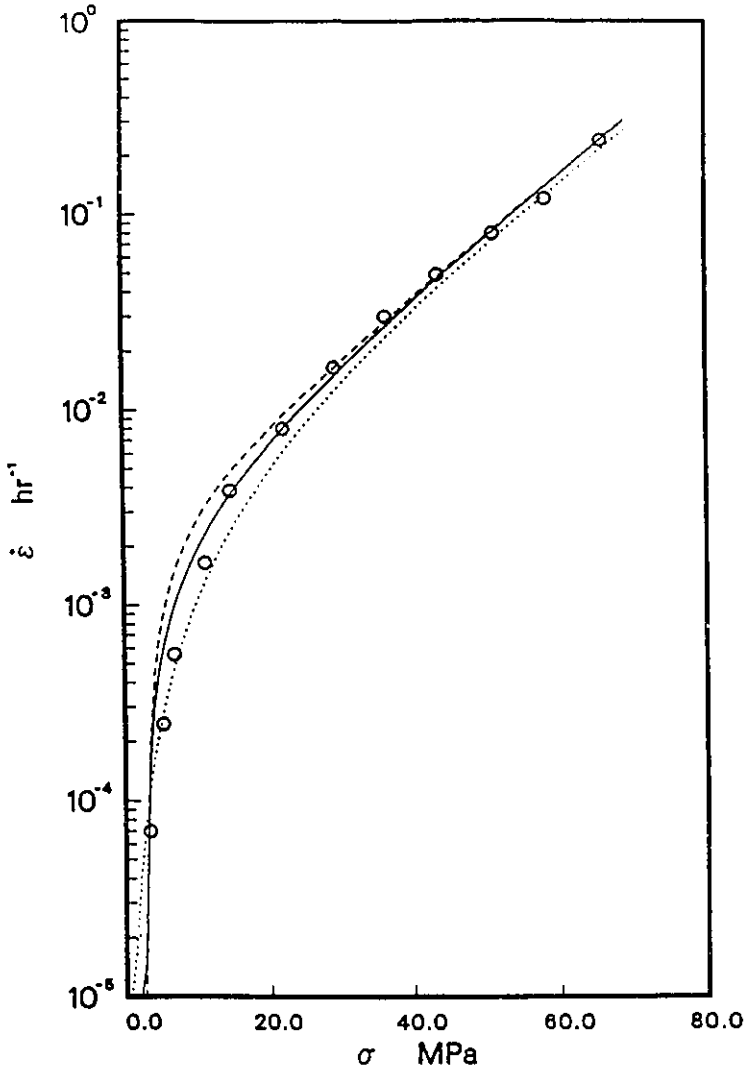

Figure 7.1. Typical strain rate vs stress relation. The solid line represents equation (7.1) with $A_f = 2 \times 10^{-3}$, $V_f/kT = 0.073$, $A_r = 2.5 \times 10^{-3}$ and $V_r/kT = 0.01$. The dotted line represents equation (7.2) with $A' = 9.17 \times 10^{-3}$, $\beta = 0.034$ and $n = 2.06$. The dashed line represents equation (7.8) with $A_f = 2 \times 10^{-3}$, $A_r = 3 \times 10^{-3}$ and $V/kT = 0.073$. The symbols represent the observed behavior [153].

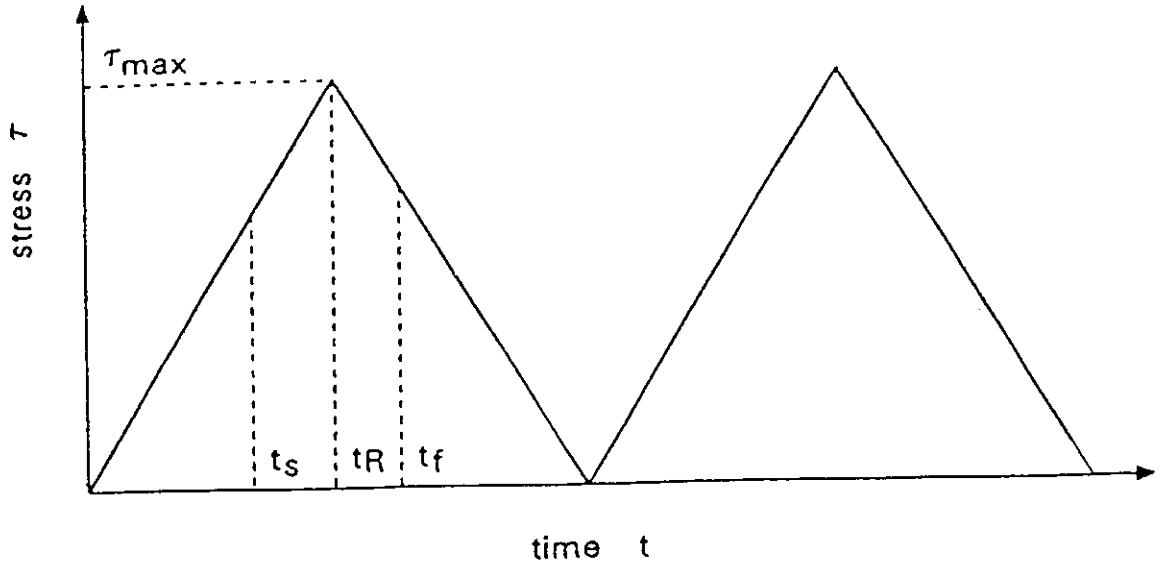

Figure 7.2. Triangular-wave loading profile. t_R is the stress rising time.

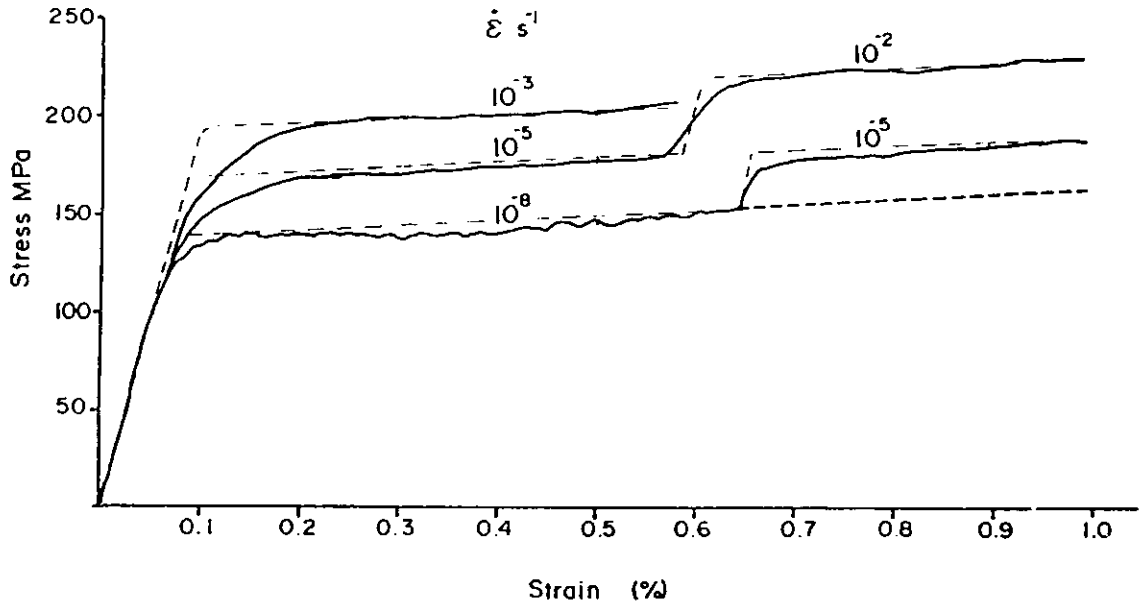

Figure 7.3. Stress-strain response in Type 403 stainless steel [155]. The solid lines represent the test behavior. The dashed lines represent equation (7.20) with $\tau_0 = 55.32$ MPa, $H = 718.33$ MPa, $V/kT = 0.43(\text{MPa})^{-1}$, and $\chi = 2 \times 10^{-13}/\dot{\epsilon}$.

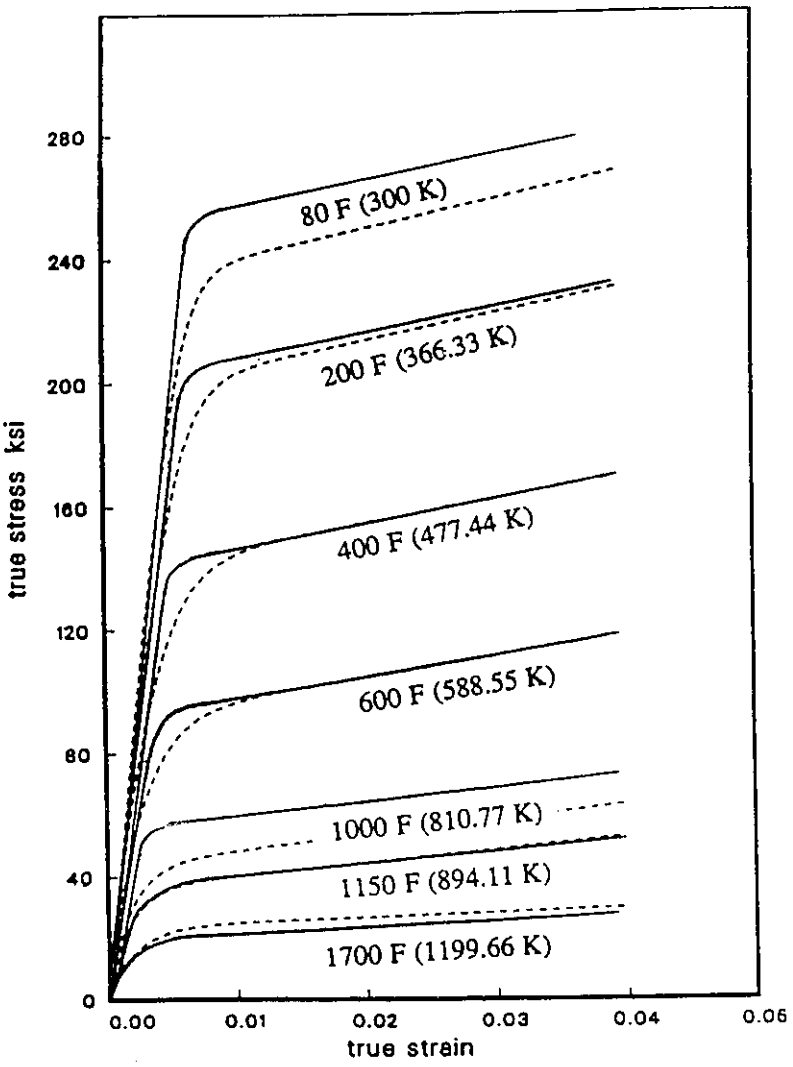

Figure 7.4. Stress-strain curves for 8660 steel [156]. The solid lines represent the observed behavior. The dashed lines represent equation (7.19) with $\chi = 66.97 \exp(-2589/T)$, $V/k = 6.5$. The elastic modulus E and work hardening coefficient H vary with the temperature as $E = 40000[1 - 0.0008(T - 300)]$ and $H = 963[1 - 0.00093(T - 300)]$. Temperature is in degree Kelvin.

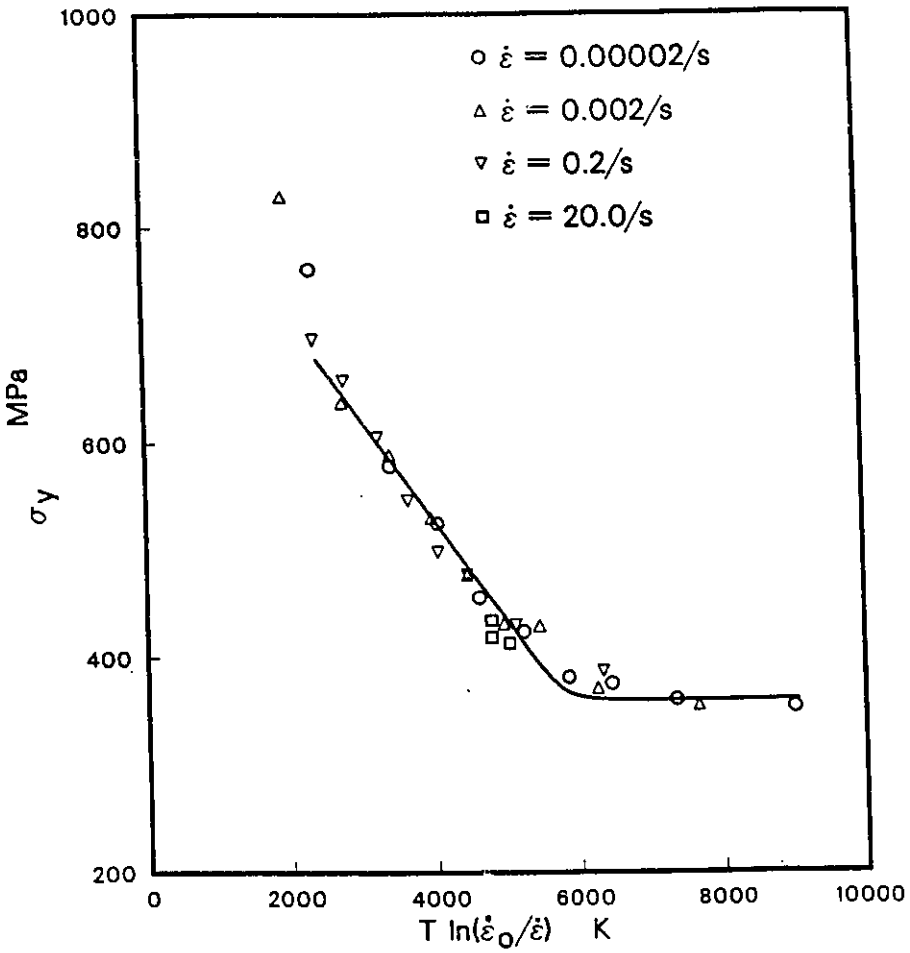

Figure 7.5. Yield stress as a function of strain rate and temperature. The symbols representthe behavior of a micro-alloyed steel [149] and the curve represent equation (7.21)

$$\sigma_y = 359.54 - 0.0942T \ln\{[\sqrt{(1+\chi^2)} - 1]/\chi\}$$

where $\chi = (5.4 \times 10^8/\dot{\epsilon}) \exp(-5800/T)$.

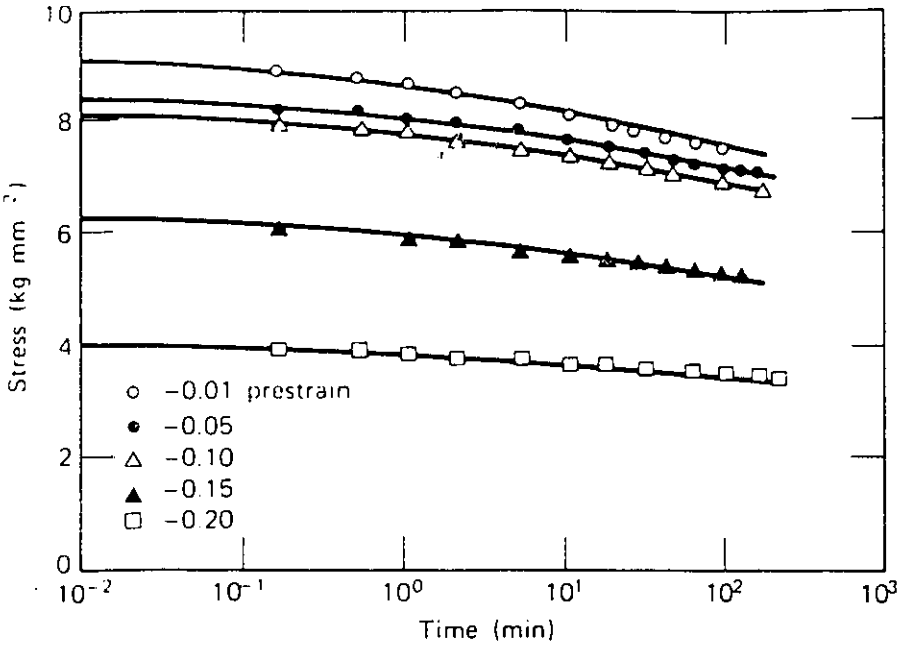

Figure 7.6. Stress relaxation in 1100 aluminum [148].

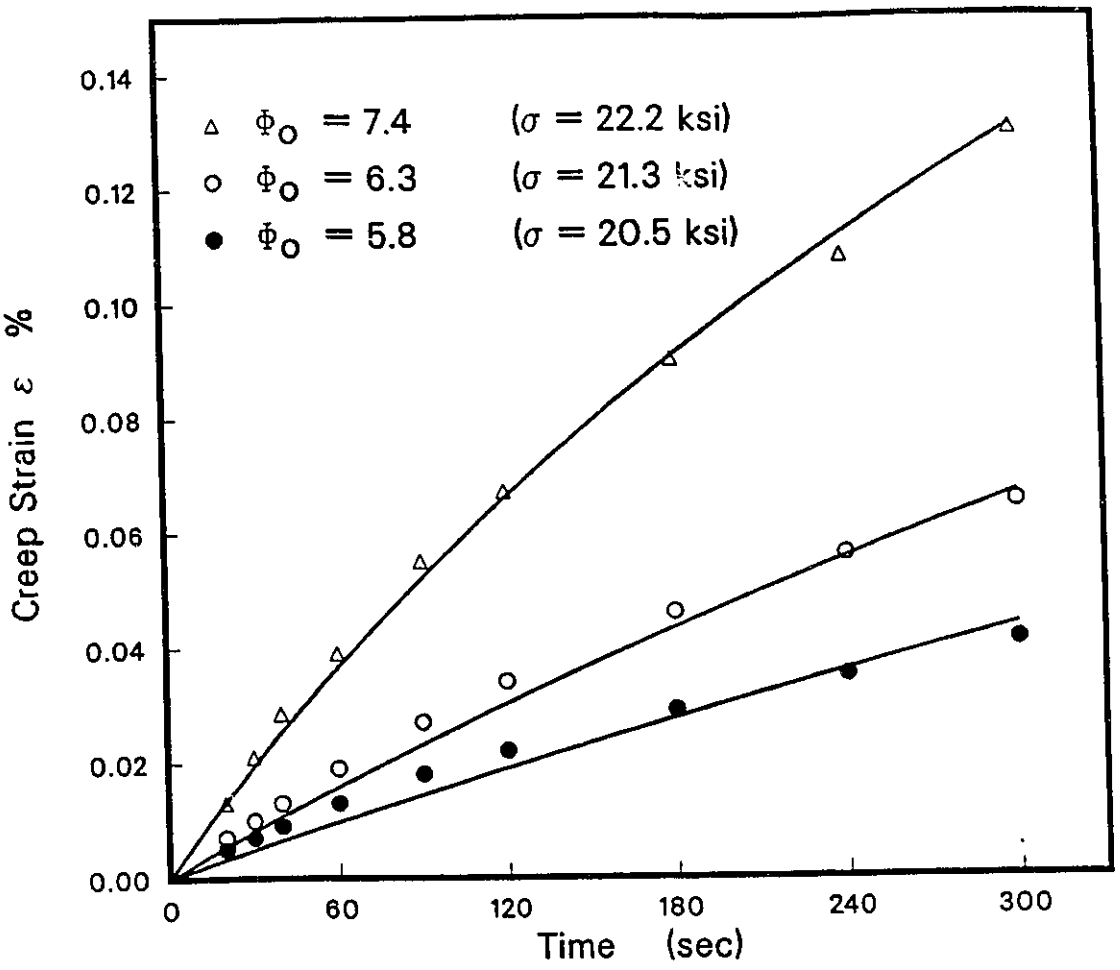

Figure 7.7. Comparison of equation (7.31) with the creep behavior of Type 304 stainless steel tested at room temperature [155]. The creep strain is given by $\epsilon = (\Phi_0 - \Phi)/\sqrt{3}VH$, where Φ is obtained from equation (7.31) with $V/kT = 0.52(\text{MPa})^{-1}$, $H = 718.33$ MPa and $2VHA/kT = 6.6 \times 10^{-6}$.

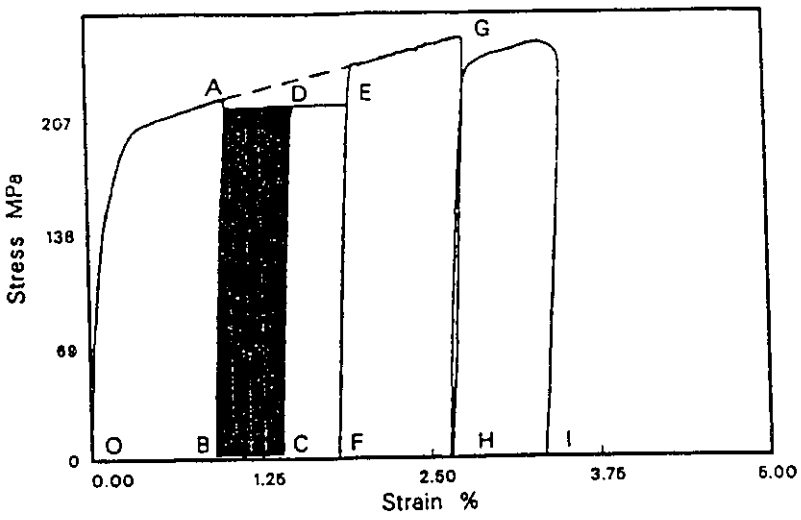

(a)

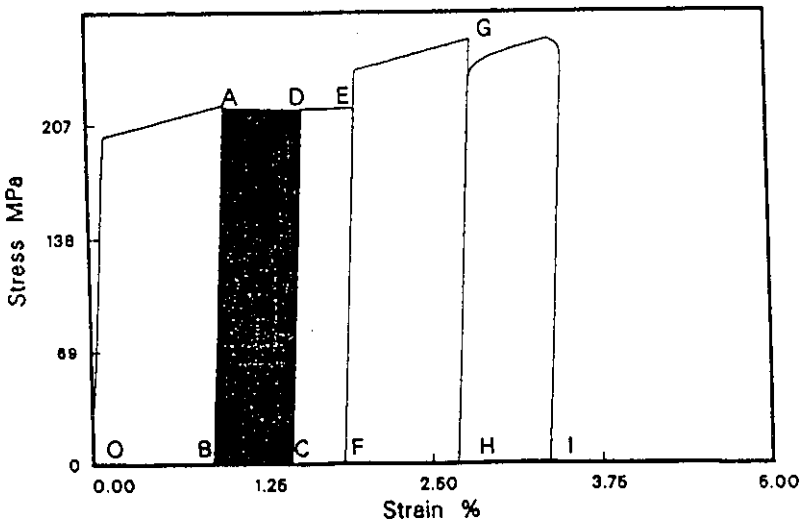

(b)

Figure 7.8. Stress-strain curve for Type 304 stainless steel: a) experimental [159]; b) predicted.

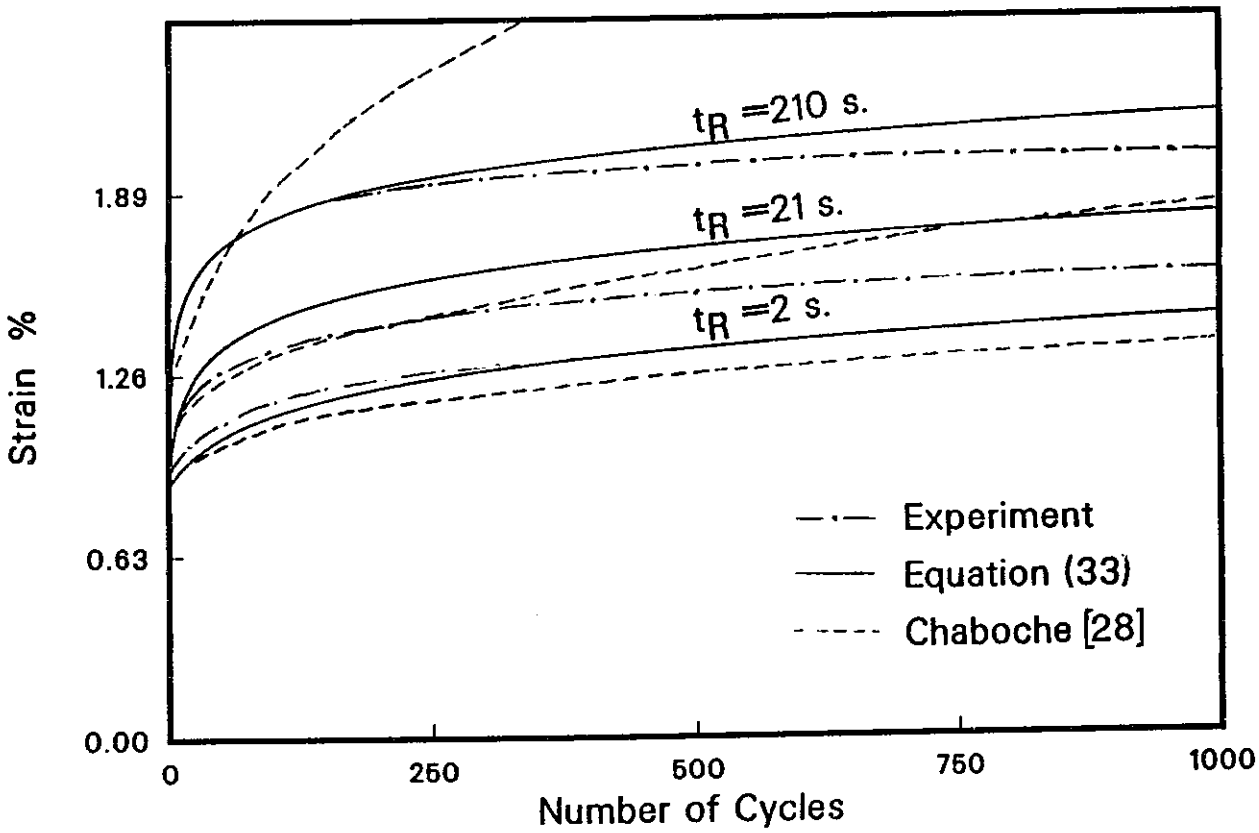

Figure 7.9. The rate-dependence of ratchet strain under stress cycling. The symbols represent the test results [159]. The solid curves are descriptions of equation (7.29) and the dashed cruves are descriptions of Chaboche's model [160].

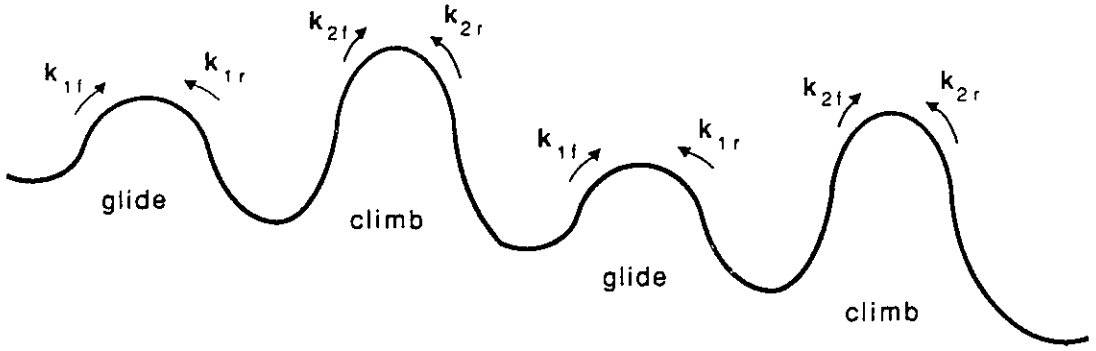

Figure 7.10. The schematic of energy barriers for dislocation motion in the glide-plus-climb sequence.

motion, proceeds independently with gliding. Suppose dislocations are stopped by an obstacle, during the time $t_1 = 1/\mathrm{k}_{1r}$ when dislocations are waiting to glide backwardly, some may overcome the climbing barrier to climb onto another crystallographic plane. The number of climbing dislocations can be calculated by

$$n_f = \rho_1 \mathrm{k}_{2f} t_1 = \dot{\rho}_1 \mathrm{k}_{2f}/\mathrm{k}_{1r}.$$

Occasionally, some of the dislocations that have climbed on the new crystallographic plane may also fall back by reverse activation. Since the waiting time at the gliding barrier is $t_2 = 1/\mathrm{k}_{1f}$, the number of backward dislocations will be

$$n_r = \rho_2 \mathrm{k}_{2r} t_2 = \rho_2 \mathrm{k}_{2r}/\mathrm{k}_{1f}.$$

Thus, the net flow over the climbing barrier is

$$n = n_f - n_r = \rho_1 \mathrm{k}_{2f}/\mathrm{k}_{1r} - \rho_2 \mathrm{k}_{2r}/\mathrm{k}_{1f}.$$

Only these dislocations that stay on the new crytallographic plane can glide continuously to produce plastic strain, following Orowan [72], the resulting plastic strain rate is

$$\dot{\gamma} = bmv_{glide} = nbl\mathsf{k}_{1f} = \delta(\rho_1 \frac{\mathsf{k}_{1f}\mathsf{k}_{2f}}{\mathsf{k}_{1r}} - \rho_2 \mathsf{k}_{2r}). \tag{7.32}$$

Equation (7.32) expresses the glide-plus-climb mechanism. At low stresses when the gliding is limited, i.e., $\mathsf{k}_{1f} \approx \mathsf{k}_{1r}$, the process is climb-controlled. At high stresses, $\mathsf{k}_{1f} \gg \mathsf{k}_{1r}$ and k_{2r}, then the process is glide-controlled. For simplicity, consider that the two barriers are symmetrical: for the gliding barrier, $\Delta G^{\ddagger}_{1f} = \Delta G^{\ddagger}_{1r}$, $V_{1f} = V_{1r} = V_G$; and for the climbing barrier, $\Delta G^{\ddagger}_{2f} = \Delta G^{\ddagger}_{2r} = \Delta G^{\ddagger}_{D}$, $V_{2f} = V_{2r} = \Omega$ (Ω is the atomic volume), then equation (7.32) can be written into

$$\dot{\gamma} = A_f \exp\left(-\frac{\Delta G^{\ddagger}_{D} - (V+\Omega)\tau_{eff}}{kT}\right) - A_r \exp\left(-\frac{\Delta G^{\ddagger}_{D} + \Omega\tau_{eff}}{kT}\right) \tag{7.33}$$

where $V = 2V_G$, $A_f = \delta\rho_1\nu$ and $A_r = \delta\rho_2\nu$. Since Ω (about b^3) is very small compared with the activation volume for gliding, V_G (about $10 - 100b^3$), and $\Omega\tau_{eff} \ll kT$ when the temperature is high, the stress dependence of the Ω term can be neglected. Then, equation (7.27) reduces to

$$\dot{\gamma} = \exp\left(-\frac{\Delta G^{\ddagger}_{D}}{kT}\right)\left[A_f \exp\left(\frac{V\tau_{eff}}{kT}\right) - A_r\right]. \tag{7.34}$$

As indicated by equation (7.32), the rate controlling process is the diffusion of single ions or vacancies to or from the climbing dislocation. The activation energy has been found to be almost equal to that of the self-diffusion [164].

In addition to strain hardening, on the other hand, high-temperature dislocation creep may be associated with diffusion controlled recovery mechanism which involves thermally activated cross-slip and edge dislocation climb. Recovery is a time-dependent process, which can be expressed with the simplest model as [166]

$$\tau_{\text{recovery}} = R^{*}t.$$

Then the effective stress is expressed as

$$\tau_{eff} = \tau - H\gamma + R^* t. \tag{7.35}$$

Substituting (7.35) into equation (7.34):

$$\dot{\gamma} = \exp\left(-\frac{\Delta G_D^{\ddagger}}{kT}\right)\left[A_f \exp\left(\frac{V(\tau - H\gamma + R^* t)}{kT}\right) - A_r\right] \tag{7.36}$$

Equation (7.36) is the constitutive law for creep in the primary and secondary (steady-state) stages.

At the steady state work hardening is in dynamic balance with recovery such that, following equation (2.21),

$$d\tau_i = H\, d\gamma - R^*\, dt = 0. \tag{7.37}$$

Then, the material has a stable substructure with

$$\tau_i = H\gamma - R^* t = \text{const.}$$

Substituting (7.37) into (7.36), at steady state,

$$\dot{\gamma}_s = \frac{R^*}{H} = \exp\left(-\frac{\Delta G_D^{\ddagger}}{kT}\right)\left[A_f \exp\left(\frac{V(\tau - \tau_i)}{kT}\right) - A_r\right] \tag{7.38}$$

Equation (7.38) is the rate equation for secondary creep where the strain rate is the lowest.

7.2.2 The Operational Equation

Let

$$\Phi = \frac{V}{kT}(\tau - H\gamma + R^* t),$$

In a creep process, the evolutionary equation of function Φ is

$$\dot{\Phi} = \frac{V}{kT}(R^* - H\dot{\gamma}) = \frac{VH}{kT}(\dot{\gamma}_s - \dot{\gamma}) \tag{7.39}$$

Substituting equation (7.38) into (7.41),

$$\dot{\Phi} = \frac{VHA_f}{kT} \exp\left(-\frac{\Delta G_D^{\ddagger}}{kT}\right)\left(\exp\left(\frac{V(\tau - \tau_i)}{kT}\right) - \exp\Phi\right) \tag{7.40}$$

which can be integrated to the form

$$\exp -\Phi = \exp\left(-\frac{V(\tau - \tau_i)}{kT}\right)\left\{1 - \left[1 - \exp\left(-\frac{V\tau_i}{kT}\right)\right]\exp(-\alpha t)\right\} \tag{7.41}$$

where

$$\alpha = \frac{VHA_f}{kT} \exp\left(-\frac{\Delta G^{\ddagger} - V(\tau - \tau_i)}{kT}\right).$$

From this, the plastic strain can be found as

$$\gamma = \frac{\tau_i}{H} + \dot{\gamma}_s t + \frac{kT}{VH} \ln\left\{1 - \left[1 - \exp\left(-\frac{V\tau_i}{kT}\right)\right]\exp(-\alpha t)\right\} \tag{7.42}$$

7.2.3 Discussion

Empirically, steady-state creep is often represented by a power-law function

$$\dot{\gamma} = A\left(\frac{\tau}{\mu}\right)^n, \tag{7.43}$$

and therefore is called *power-law creep*. The power law (7.39), however, fails to describe creep at high stresses (above about $10^{-3}\mu$) where it is believed that deformation undergoes a transition from climb-controlled to glide-controlled flow and a better fit to experiment is found with [4]

$$\dot{\gamma}_s \propto \exp\left(-\frac{\Delta G_D^{\ddagger}}{kT}\right) \exp B\tau,$$

and the phenomenon is called *power-law breakdown* [4].

To describe creep rates over the full stress range, a $\sinh^n$ type equation was proposed by Garofalo [165]:

$$\dot{\gamma}_s = A' \sinh^n \beta\tau. \tag{7.44}$$

The correlation of these empirical or semi-empirical equations with the physically based rate equation has been discussed in the previous section and will not be repeated here. Figure 7.11 shows the comparison of equation (7.38) with the power-law equation (7.41) and the $\sinh^n$ equation (7.38) for creep in pure aluminum [167].

The operational equation (7.42) describes the strain vs time relation in the primary and the secondary stages of creep. Generally, creep decelerates with the accumulation of plastic strain in the primary stage until the creep rate reaches a minimum value, and follows the secondary creep where creep strain vs time exhibits a linear relationship. Figure 7.12 shows the creep behavior of Ti-8Al-1Mo-1V alloy solution annealed at 1950° F [168].

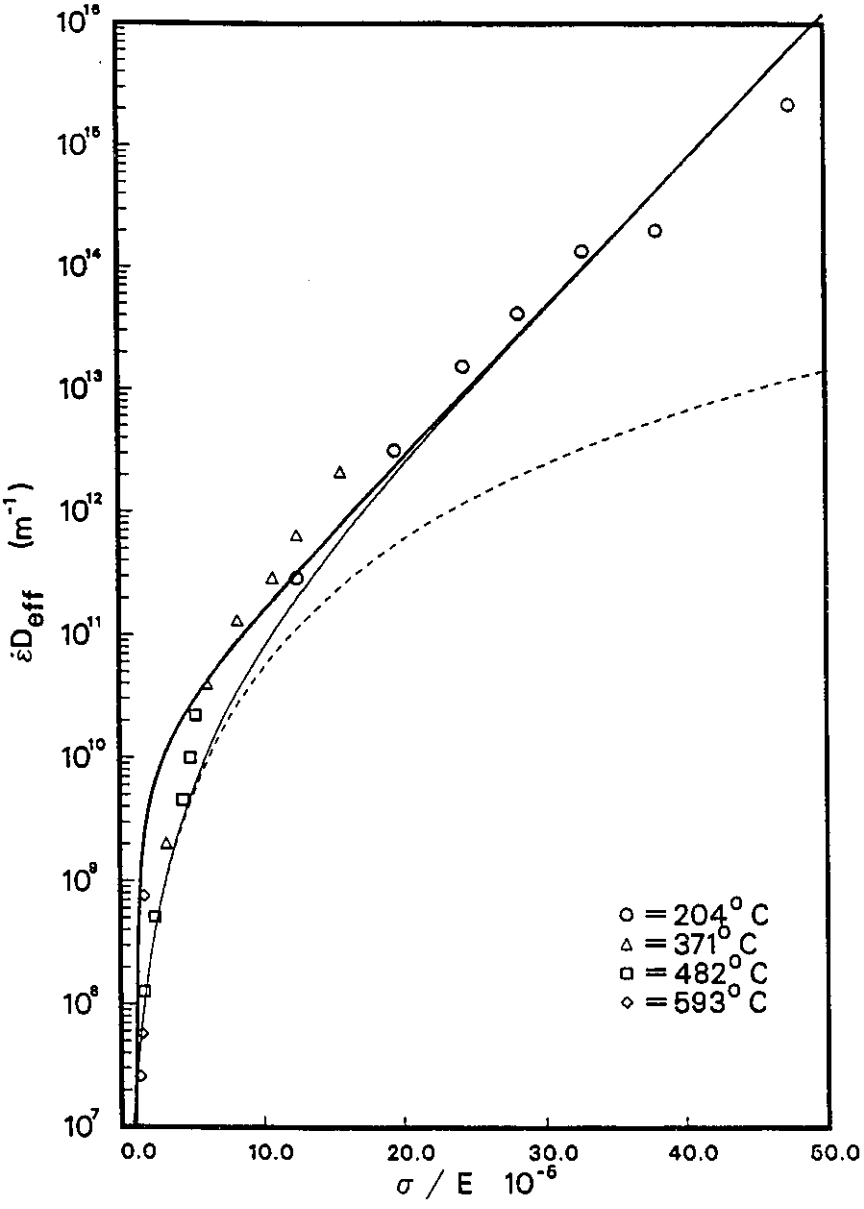

Figure 7.11. Steady-state creep rate in pure aluminum. Symbols represent test data [167]. The heavy curve represents the description of equation (7.32):

$$\dot{\varepsilon}D_{eff} = 10^{10}[\exp(0.28 \times 10^{5}\tau/E) - 1.38]$$

The light curve was obtained from (7.38) with $A' = 1.13 \times 10^{11}$, $B = 8 \times 10^{3}/E$ and $n = 3.5$. The dashed curve was obtained from the power law (7.37) with $n = 3.5$ and $A = 1.64 \times 10^{7}$.

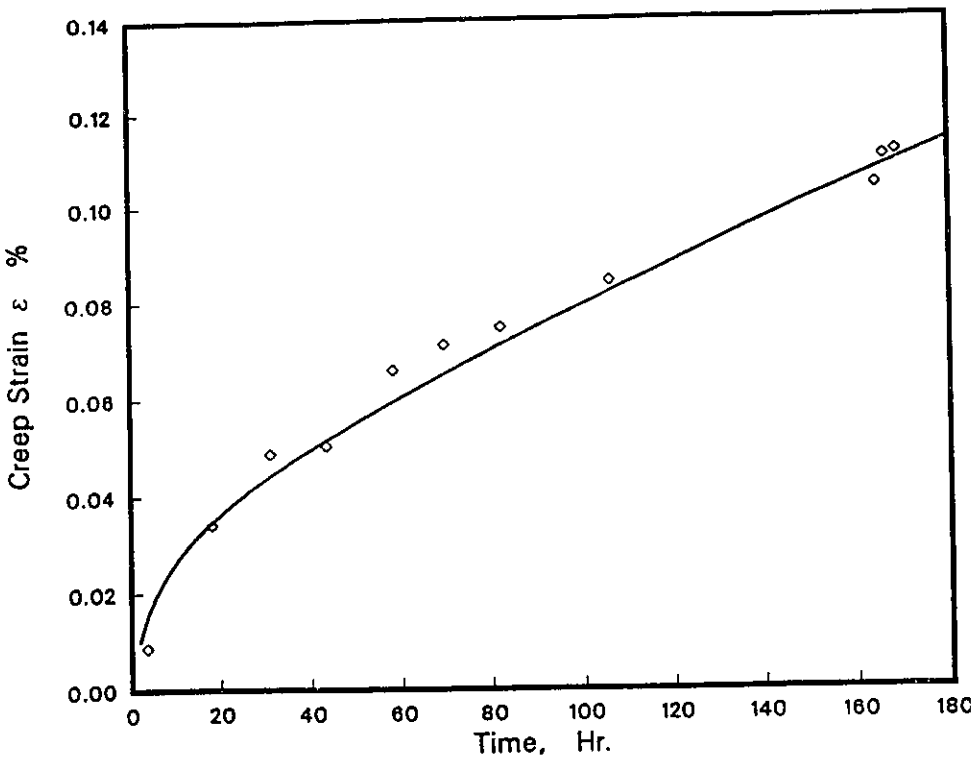

Figure 7.12. Creep strain vs time relation for Ti-8Al-1Mo-V alloy prior solution annealed at 1950° F and tested at 50 ksi and 850°F. Symbols represent the test behavior [168]. The curve was obtained from equation (7.36) with $\tau_i/H = 0.043, V\tau_i/kT = 4.3, VH/kT = 100, \dot{\varepsilon}_s = 0.0004, \alpha = 0.012$.

7.3 Diffusional Flow

The diffusion of point defects results in a deformation rate falling into the high temperature-low stress region of the deformation map as shown in Figure 2.1 [4]. In this regime, however, a distinction is made between Nabarro-Herring creep [169,170] associated with diffusion through the grain, and Coble creep [171] associated with diffusion at grain boundaries. As an alternative mode of deformation, these diffusional flows lead to strain, provided they are coupled with grain boundary sliding to accommodate the shape change of grains [173,172,174]. It has been shown that diffusion-controlled plastic deformation can be represented a symmetrical barrier, and hence the rate equation takes the form of a hyperbolic sine function as [15,166]

$$\dot{\gamma} = 2A \exp\left(-\frac{\Delta G^{\ddagger}}{kT}\right) \sinh\left(\frac{V\tau_{eff}}{kT}\right) \tag{7.45}$$

where $\tau_{eff} = \tau - H\gamma + R^{*}t$ is the effective stress.

At high temperature and low stress such that $V\tau_{eff}/kT \ll 1$, equation (7.45) reduces to

$$\dot{\gamma} = 2A\mathrm{k}^{\ddagger}\frac{V\tau_{eff}}{kT}. = 2A\mathrm{k}^{\ddagger}\frac{V(\tau - H\gamma + R^{*}t)}{kT}. \tag{7.46}$$

Following the same procedure as in the previous section, equation (7.46) can be integrated to

$$\gamma = \dot{\gamma}_s t + \frac{\tau_i}{H}\left[1 - \exp\left(-\frac{2VHA\mathrm{k}^{\ddagger}t}{kT}\right)\right]. \tag{7.47}$$

Equation (7.47) is the operational equation for diffusional flow-controlledplastic deformation. It is in formal agreement with the well-known Garofalo equation [175], the validity of this equation has been firmly established and needs no discussion further.

Chapter 8

Summary and Conclusion

The time and temperature dependence of plastic deformation and crack growth is an indispensable part of deformation and fracture of metallic materials. When deformation and/or crack growth results from thermally activated processes, each elementary step is described by the the elementary rate constant defined by statistical mechanics as

$$\mathsf{k} = \nu \exp\left(-\frac{\Delta G^{\ddagger}(W)}{kT}\right).$$

Following kinetics principles, the appropriate combination of elementary rate constants can be derived to represent the underlying mechanism of deformation and/or crack growth. The mathematical expression of the kinetics combination is the physically based constitutive law.

8.1 Transgranular Fatigue Crack Growth

1) Based on the concept of restricted slip reversibility (RSR), a transgranular fatigue crack growth model has been developed to represent crack growth processes that result in transgranular fracture. The RSR model provides a physical description for striation formation during fatigue crack growth, a feature that has been verified through numerous experimental observations. The proposed model correlates transgranular fatigue

crack growth with the plastic deformation accommodation ahead of the crack tip. Its formulation through equation (3.5) comes out of a rationale based on the physically realistic RSR mechanism. Under the assumption of small scale yielding conditions where stress intensity factor is believed to control the near-tip stress field, the fatigue crack growth rate is shown to be generally dependent on the microstructural and environmental quantities (activation energies, activation volumes, work factors, internal stresses), material properties (yield strength and work hardening coefficient) as well as test conditions ($\Delta K, R, T, f$). In the absence of environmental effects, the FCGR model takes the form of the Paris equation with a physically defined power law exponent of 3:

$$\frac{da}{dN} = C(\Delta K)^3 \tag{8.1}$$

where

$$C = \frac{\alpha_f - \alpha_r}{12\pi(1-R)H\sigma_y^2}.$$

- Equation (8.1) predicts that, if microstructural change only results in the change of yield strength σ_y and work hardening coefficient H without affecting the slip systems of the alloy, FCGRs will decrease inversely with increasing $H\sigma_y^2$.
- The model also predicts that the rate of fatigue crack growth increases with increasing the stress ratio R. For the first order approximation (the R effect on the cyclic plastic zone size has not been taken into account), FCGR is inversely proportional to (1-R).

2) FCGR tests on a 8090 Al-Li alloy have shown that fatigue crack growth in this alloy proceeds along crystallographic slip planes and fatigue crack growth rate varies with specimen orientation. With strong textures in the material, the geometrical relation between the preferred slip planes and the load axis will vary with specimen orientation. The RSR model is extended to transgranular fatigue crack growth in Al-Li alloys involving highly planar slip. In the absence of environmental effects, the model takes the form

$$\frac{da}{dN} = C(\Delta K)^3 \cos^2\phi. \tag{8.2}$$

where the geometric factor $\cos^2\phi$ (ϕ is the angle between slip band facets and the specimen thickness axis) is texture related.

Equation (6.2) predicts that FCGR is slower in textured materials than texture free materials because for a textured material $\phi > 0$ and $\cos^2\phi < 1$.

3) In a reactive environment, corrosion products may accumulate in the form of either oxidation or hydrogen embrittlement, or dissolution may occur. It is appreciated that all corrosion damage processes occur in a localized region ahead of the crack tip. Incorporating a corrosion damage zone into the RSR model, it has been shown that the general environment assisted fatigue can be expressed as

$$\left(\frac{da}{dN}\right)_e = \left(\frac{da}{dN}\right)_m + \xi\left(\frac{da}{dN}\right)_c \tag{8.3}$$

the first term represents the mechanical fatigue described by equation (8.1), the second term represents the environmental enhancement of crack growth and is directly related to the corrosion damage zone size, $\xi = [1-(1+\varepsilon_c)\Delta\gamma]$ is the weight function for corrosion fatigue.

8.2 Temperature Dependence in Stress Corrosion Cracking

The conventional, usually observed material behavior is increasing crack growth rate with increasing temperature, as described by the Arrhennius type equation

$$v = v_o \exp\left(-\frac{\Delta G^{\ddagger}(W)}{kT}\right) \tag{8.4}$$

which exhibits a positive temperature dependence.

Under circumstances, the rate of crack growth may decrease with increasing temperature, exhibiting a negative temperature dependence. This unusual behavior is thought

to be the result of competition between bond breaking and healing processes that control the crack growth.

A fracture kinetics description is derived for the positive-negative temperature dependence of stress corrosion cracking at stages I and II. The constitutive law (6.6) is derived from the general rate equation for a consecutive system with two energy barriers, which takes the form

$$v = \left(\frac{\mathsf{k}_1}{\kappa_1 \nu^2} + \frac{1}{\kappa_{2f} \mathsf{k}_{2f}} \right)^{-1} - \kappa_{2r} \mathsf{k}_{2r} \tag{8.5}$$

where

$$\begin{aligned} \mathsf{k}_1 &= \nu \exp\left(-\frac{\Delta G_1^{\ddagger} + \alpha_1 K}{kT} \right) \\ \mathsf{k}_{2f} &= \nu \exp\left(-\frac{\Delta G_{2f}^{\ddagger} - \alpha_{2f} K}{kT} \right) \\ \mathsf{k}_{2r} &= \nu \exp\left(-\frac{\Delta G_{2r}^{\ddagger} + \alpha_{2r} K}{kT} \right) \end{aligned}$$

It expresses the rate of crack growth explicitly in terms of stress intensity factor and temperature: it provides a quantitative description of the cross-over behavior. The theoretical description has been found in good agreement with the observed behavior.

The fracture kinetics analysis shows that the cross-over behavior occurs in the near-threshold region where bond healing effects predominate. Although no particular mechanism is implied in the description, it does suggest that reverse activation is an important part of the crack growth mechanism, may it be an absorption-desorption type or diffusion-controlled hydrogen partitioning. In all of these processes, reverse activation does occur.

The fracture kinetics analysis provides an effective method for quantitative determination of the transition condition at a given stress intensity level, using equation (6.7). The study provides the means for crack growth control.

8.3 Plastic Deformation

Based on deformation kinetics theory, evolutionary rate equations have been derived for the representation of dislocation-glide mechanism, the glide-plus-climb mechanism and diffusional flow.

Generally, the plastic strain rate can be expressed as

$$\dot{\gamma}_p = \dot{\gamma}_{f0} \exp\left(-\frac{\Delta G_f^{\ddagger} - V_f \tau_{eff}}{kT}\right) - \dot{\gamma}_{r0} \exp\left(-\frac{\Delta G_r^{\ddagger} + V_r \tau_{eff}}{kT}\right) \tag{8.6}$$

where the effective stress can generally be expressed as

$$\tau_{eff} = \tau - H\gamma + R^* t - \tau_{i0}.$$

For low-temperature plastic deformation, the above rate equation can be equivalently expressed by a hyperbolic sine form. The operational equations under constant strain rate, constant stress rate and stress controlled cycling, constant strain (stress relaxation) and constant stress (creep) conditions have been integrated and shown in good agreement with experimentally observed material behaviors.

For dislocation creep, the rate equation (8.6) represents the kinetics combination of glide and climb steps. An operational equation is obtained by integrating the governing rate equation, which describes the strain-time response in primary and secondary creep. The theoretical description has been found in close agreement with observed behaviors.

For diffsional flow, the evolutionary rate equation is integrated to a form similar to Garofalo equation.

Comparing with other unified constitutive models (see the reference [88]), deformation kinetics theory leads to mathematically rigorous, simple yet adequately accurate constitutive models that can be used to predict material responses under a variety of loading constraints.

The concept of the evolutionary energy function Φ is proposed. Since all thermally activated deformation processes are controlled by the apparent activation energy, $\Delta G^{\ddagger}(W) = \Delta G^{\ddagger} \pm W = \Delta G^{\ddagger} \pm kT\Phi$, the ongoing of a deformation process is fully determined by the evolution of the activation energy content. This principle may render an unified approach to the establishment of physically based constitutive laws of plastic deformation. According to the laws of statistical thermodynamics, any structure change that results from the rearrangement of atomic configurations could be related to the change in entropy and enthalpy of the material. In the notion of thermodynamics,

$$\Delta G^{\ddagger}(W) = \Delta H + T\Delta S$$

where H represents the enthalpy and S represents the entropy.

8.4 Recommendations on Future Research

1. The FCGR tests on the 8090 Al-Li alloy should be completed by metallurgical measurements of angles θ and ϕ for all specimen orientations. A few tensile tests should also be carried out to obtain the mechanical properties along the interested direction.

2. A series of tests under ΔK decreasing conditions should be carried out to allow the examination of crack growth rates in the near threshold region.

3. A series of tests with periodic overloads, approaching K_c, should be conducted to see whether the overloads induce inclined fracture.

4. The texture of the 8090 Al-Li alloy should be examined by metallurgical means in order that a deterministic relation can be established between the orientation of the specimen and the path of crystallographic crack growth. The RSR model in the form of equation (8.1) and (8.3) should be further testified by the data obtained from the above experiments. For the description of the full range of crack growth, the model should be further extended to include crack closure effect, if significant crack closure level is detected in experiments (2).

5. Corrosion chemistry processes should be incorporated into the RSR model to describe the time dependent environmental assisted fatigue (e.g. corrosion fatigue and hydrogen embrittlement). The fracture work condition in environment assisted cracking should be examined on a physical and mechanical basis.

6. The possibility of extending Ashby's deformation map concept to crack growth should be investigated.

Bibliography

[1] H. L. Gegel, "Processing Science and Materials Development", Air Force Wright Aeronautical Laboratories/Materials laboratory, Wright-Patterson Air Force Base, Ohio, USA.

[2] G.A. Davies, "Structural Qualification By Finite Element Analysis", 61st Meeting of the Structures and Marterials Panel, Semptember, 1985.

[3] M.F. Ashby, *Acta Metall.* **20**, 887 (1972).

[4] H.J. Frost and M.F. Ashby, *Deformation Mechanism Maps*, Pergamon Press, 1982.

[5] R. Becker, *Phys. Z.* **26** (1925) p. 919.

[6] H. Eyring, *J. Chem. Phys.* 4 (1936) p. 283.

[7] E. Orowan, *Z. Phys.* **91** (1936) p. 382.

[8] E. Orowan, *Proc. Roy. Soc. London* ser. A **168** (1938) p. 307.

[9] W. Boas and E. Schmid, *Z. Phys.* **100** (1936) p. 463.

[10] S. Glasstone, K.J. Laidler and H. Eyring, *The theory of Rate Processes*, McGrw-Hill (1941).

[11] S.W. Benson, *The Foundations of Chemical Kinetics*, McGraw-Hill, 1960.

[12] K.J. Laidler, *Chemical Kinetics*, McGraw-Hill, 1965.

[13] D. Caldwell and H. Eyring, *Perspectives in Quantum Theory*, Dover Publications, 1972, p. 117.

[14] J.P. Hirth and W.D. Nix, *Phys. Stat. Sol.* **35**, 177 (1969).

[15] A.S. Krausz and H. Eyring, *Deformation Kinetics*, Wiley-Interscience, New York, 1975.

[16] P.C. Paris and F. Erdogan, *Journal of Basic Engineering* 85 (1963) p. 528.

[17] P.C. Paris, *Fatigue Thresholds* Vol.I, Engineering Materials Advisory Services (1982), p. 3.

[18] A.J. McEvily and R.P. Wei, in *Corrosion Fatigue* NACE-2, National Association of Corrosion Engineerers (1972), p. 381.

[19] A.S. Krausz and K. Krausz, *Fracture Kinetics of Crack Growth*, Kluwer Academic Publishers, 1988.

[20] R.O. Ritchie, *Int. Metals Rev.* **25** (1979), p. 205.

[21] S.Kocanda, Failure of Metals, Sijthoffand Noordhoff, Alphen aan den Rijn, The Netherlands (1978).

[22] M.F.Kanninen and C.H. Popelar, *Advanced Fracture Mechanics*, Oxford University Press, 1985, p. 489.

[23] W. Schutz, in *Fatigue Thresholds* Vol. II, Engineering Materials Advisory Services (1982), p. 911.

[24] K. Tanaka, *Fracture Mechanics: Perspectives and Directions*, ASTM STP 1020 (1989), p. 151.

[25] R.G. Forman, V.E. Kearney and R.M. Engle, *J. Basic Eng.* **89** (1967), p. 459.

[26] M.O. Speidel, in *Stress Corrosion Cracking and Hydrogen Embrittlement of Iron-Base Alloys*, NACE-5, National Association of Corrosion Engineers (1977) p. 1071.

[27] D.B. Dawson and R.M. Pelloux, *Metall. Trans.*, **5** (1974), p. 723.

[28] R.P. Gangloff, in *Environment Induced Cracking of Metals*, NACE-10, National Association of Corrosion Engineers (1990) p. 55.

[29] W.H. Bamford, in *Corrosion Fatigue* , ASTM STP 801 (1983), p. 405.

[30] W. Yu and R.O. Ritchie, *Trans. ASME, J. Engng. Mater. & Tech.* **109** (1987), p. 81.

[31] P.E. Bretz, L.N. Mueller and A.K. Vasudevan, in *Aluminum-Lithium Alloys II Conf., AIME*, Monterey, California, 1983, p. 543.

[32] M. Peters, K. Welpman, W. Zink and T.H. Sanders Jr., in *Aluminum-Lithium Alloys III Conf., Inst. Metals* Oxford, U.K., 1985, p. 237.

[33] A.J. Forty and P. Humble, *Phil. Mag.* **8** (1963), p. 247.

[34] A.J. McEviley and A.P. Bond, *Trans. ASM* **60** (1967), p. 661.

[35] D.A. Vermilyee, *J. Electrochem. Soc.* **119** (1972), p. 405.

[36] T.R. Beck, *Corrosion* **30** (1974), p. 408.

[37] R.P. Gangloff and R.P. Wei, *Metall. Trans.* 8A (1977), p.1043.

[38] R.P. Wei, in *Fatigue Mechanism*, ASTM STP 675 (1979), p. 816.

[39] T. Yokobori, *International Congree on Fracture: Dritte Internationale Tagung uber den Bruch*, vol.1, Verein Deutscher Eisenhuffenleute (1973), p. 1.

[40] P.J. Bania and S.D. Antolovich, *Stress Corrosion: New Approaches*, ASTM STP 610 (1976), p. 157.

[41] P.K. Liaw and V.P. Swaminathan, *Eng. Fract. Mech.* **34** (1989), p. 457.

[42] J.D. Frandsen and H.L. Marcus, *Metall. Trans.* 8A (1977) p. 230.

[43] R.P. Skelton (Editor), *Fatigue At High Temperature*, Applied Science Publishers, london & New York, 1983.

[44] W. Elber, *Engineering Fracture Mechanics* **2** (1970), p. 37.

[45] R.O. Ritchie, in *Fatigue Thresholds* Vol.I, Engineering Materials Advisory Services (1982), p. 503.

[46] C.J. Beevers, in *Fatigue Thresholds* Vol.I, Engineering Materials Advisory Services (1982), p. 257.

[47] T.C. Lindley and C.E. Richards, in *Fatigue Thresholds* Vol.II, Engineering Materials Advisory Services (1982), p. 1087.

[48] R.O. Ritchie, in *Fracture and Fracture Mechanics*, Pergamon Press, 1985, p. 93.

[49] R.C. McClung, *Metall. Trans.* **22**A (1991), p. 1559.

[50] K. Krausz, X. Wu, Z. Lian and A.S. Krausz, *Z. Metallkd* **83** (1992) p. 283.

[51] A.S Krausz, X. Wu, Z. Lian and K. Krausz, *Z. Metallkd* **83** (1992) p. 356.

[52] F.A. McClintock, in *Fracture of Solids*, John Wiley & Sons, New York, 1963, p. 65.

[53] J.R. Rice, in *Fatigue Crack Propagation*, ASTM STP 415 (1967).

[54] T. Mura and C.T. Lin, *Int. J. Fract.* **10** (1974), p. 284.

[55] A.J. McEvily, in *Fatigue Mechanisms: Advances in Quantitative Measurement of Physical Damage*, ASTM STP 811 (1983), p. 283.

[56] A.S. Kuo and H.W. Liu, *Scripta Metall.* (1980), p. 525.

[57] J. Weertman, in *Mechanics of Fatigue* , American Society of Mechanical Engineering (1981), p. 11.

[58] S.M. Wiederhorn and L.H. Boltz, *J. Amer. Ceram. Soc.* **53** (10) (1970), p. 543.

[59] S.P. Brown, *Proc. 6-th Canadian Congr. on Appl. Mech.* (1977), p. 257.

[60] A.S. Krausz *Int. J. Fract.* 14 (1978), p. 5.

[61] A.S. Krausz and K. Krausz, *Canadian Metall. Quart.* **23** (1984), p. 107.

[62] K. Krausz and A.S. Krausz, *Deformation of Ceramic Materials*, Plenum, 1984, p. 547.

[63] A.S. Krausz and K. Krausz, *Proceedings of the 2nd International Conference on Fatigue and fatigue Thresholds* (1984) 497–510.

[64] K. Krausz and A.S. Krausz, in *Fatigue'87* III (1987), p. 1239.

[65] K. Krausz, Int. J. Fract. **36** (1988), p. R23.

[66] A.S. Krausz and K. Krausz, *Z. Metallkunde* **81** (1990), p. 181–192.

[67] K. Krausz and A.S. Krausz, Int. J. Fract. **47** (1991), p. R37.

[68] R.P. Wei and G. Shim, in *Corrosion Fatigue*, ASTM STP 801 (1983), p. 5.

[69] T.L. Hill, *Statistical Mechanics*, McGraw-Hill (1965).

[70] G.J. Taylor, *Proc. Roy. Soc. London* **A145** (1934) p. 362.

[71] M. Polanyi and E. Schmid, *Z. Physik* **16** (1923), p.336.

[72] E. Orowan, *Proc. Phys. Soc.* **52** (1940), p. 8.

[73] A.A. Griffith, *Phil. Trans. Roy. Soc. London* **A221** (1921), p. 163.

[74] A.A. Griffith, *Proc. 1st Conf. Appl. Mech.*, Delft (1924).

[75] E. Orowan, *Proc. Roy. Soc. London*, ser. A **171** (1939), p. 79.

[76] J. Wadsworth, Acta Metall. **11** (1963), p. 663.

[77] K.U. Snowden, Acta Metall. **11** (1963), p. 675.

[78] P.J.E. Forsyth, Acta Metall. **11** (1963), p. 703.

[79] C. Laird and G.C. Smith, *Phil. Mag.* **7** (1962), p. 847.

[80] P. Newmann, Acta Metall. **22** (1974), p. 1155.

[81] R.M.N. Pelloux, ASM Trans. Quart. **62** (1969), p. 1.

[82] F.A. McClintock, Fracture, H. Liebowitz ed., Vol.3, Academic Press, 1971, p.47.

[83] C. Fong and D. Tromans, *Metall. Trans.* **19A** (1988), p. 2753.

[84] C. Fong and D. Tromans, *Metall. Trans.* **19A** (1988), p. 2765.

[85] G. Alefeld, *Z. Naturforsch* **17a** (1962) p. 899.

[86] R.W. Bailey, *J. Inst. Metals* **35** (1926) p. 27.

[87] E. Orowan and J.W. Scot, *Iron Steel Inst.* **54**, 45 (1946-47).

[88] A.K. Miller (Editor), *Unified Constitutive Equations for Creep and Plasticity*, Elsevier Applied Science, 1985.

[89] N.J. Marchand, in *Constitutive Laws of Plastic Deformation and Fracture*, 19th Canadian Fracture Conf., Ottawa, Ontario, 1989.

[90] X.J. Wu, A. K. Koul and A.S. Krausz, "A Transgranular Fatigue Crack Growth Model Based On Restricted Slip Reversibility", LTR-ST-1831, IAR, NRC, 1991.

[91] J.R. Rice, *ASTM STP* **415** (1967) p. 247.

[92] W.G. Johnston,*J. Appl. Phys.* **33** (1965), p. 2716.

[93] V.I. Smirnov, *A Course of Higher Mathematics*, Vol. I, Pergamon Press, 1964.

[94] Damage Tolerant Design Handbook, MCIC-HB-01, Part 2, Metals and Ceramics Information Center, Battelle, Columbus Laboratory (1975) 8.3-7; 8.4-10; 8.1-87; 8.5-4(1/75).

[95] M.W. Mahoney and N.E. Paton, *Nuclear Technology* **23** (1974), p. 53.

[96] G. Schuster and C. Altstetter, *Metall. Trans.* **14A** (1983), p. 2077.

[97] A.R. Rosenfield, *Eng. Fract. Mech.* **9** (1977), p. 509.

[98] L.A. James and W.J. Mills, *Eng. Fracture Mech.* **22** (1985), p. 797.

[99] D.D. Krueger, S.D. Antolovich and R.H. Van Stone, *Metall. Trans.* **18A** (1987), p. 1431.

[100] R.H. Van Stone, D.D. Krueger and L.T. Duvelius, in *Fracture Mechanics II, Testing and Applications*, ASTM STP 791 (1983), p. 553.

[101] Metals Handbook 9th Edition Vol. 3, American Society for Metals, Metals Park, 1980, p. 753; 755; 764.

[102] W.W. Gerberich and N.R. Moody, in *Fatigue Mechanisms*, ASTM STP 675 (1979), p. 292.

[103] M.H. Swain and J.C. Newman, *Proc. AGARD Conf. on Fatigue Crack Topography*, AGARD-CP-376, 1984, p. 12-1.

[104] J.C. Wang and Y.Z. Lu, *Eng. Fract. Mech.* **34** (1989) p. 831.

[105] J.P. Benson and D.V. Edmonds, *Matel Sci.* **12** (1978), p. 223.

[106] I.M. Ritche, *Phil. Mag.* **19** (1969), p. 421.

[107] K.T. Venkateswara Rao, W. Yu and R.O. Ritchie, *Metall. Trans.* **19A** (1988) p. 563.

[108] K.T. Venkateswara Rao, W. Yu and R.O. Ritchie, *Aluminum-Lithium Alloys: Design, Development and Application Update*, ASM Int., 1987, p. 173.

[109] K.T. Venkateswara Rao, R.S. Piascik, R.P. Gangloff and R.O. Ritchie, in *Aluminum-Lithium Alloys*, Vol. II, 5th Int. Al-Li Conf., Williamburg, VA, 1989, p. 955.

[110] G.R. Yoder, P.S. Pao, M.A. Imam, L.A. Cooley, in *Aluminum-Lithium Alloys*, Vol. II, 5th Int. Al-Li Conf., Williamburg, VA, 1989, p. 1033.

[111] D. McCammond, S.A. Meguid, A.N. Sinclair, J.K. Spelt, R.D. Venter, M. Gabbani and M. Mummi, "A Critical Review of Aluminum-Lithium Technology and Its Impact on Aircraft Structural Design, Manufacturing and Maitenance Part II", NAE-CR-4, NRC No. 31068, 1989.

[112] K.S. Chan and J.H. Fitsgerald, *Eng. Fract. Mech.* **40** (1991) p. 251.

[113] Test Plan and Instructions for E24.04. Round Robin on Crack Opening Load Measurement, ASTM E-24, 1991.

[114] R.O. Ritchie, *Intl. Metals Reviews* **20** (1979), p. 205.

[115] R.J. Cooke, P.E. Irving, G.S. Booth and C.J. Beevers, *Eng. Fract. Mech.* **7** (1975), p. 69.

[116] D. Benoit, R. Namdar-Tixier and R. Tixier, *Mater. Sci. & Eng.* **45** (1980), p. 1.

[117] R.P. Wei and G.W. Simmons, in *Fatigue: Enviroment and Temperature Effects*, Sagamore Army Material Research Conference Proceedings, Vol. 27, 1983, p. 59.

[118] T-H. Shih and R.P. Wei, *Eng. Fract. Mech.* **18** (1983), p. 827.

[119] R.P. Gangloff, *Metall. Trans.* **16A** (1985), p. 953.

[120] K. Hauffe, *Oxidation of Metals*, Plenum Press, New York, 1965.

[121] Johnson, H.H. and P.C. Paris, *Engineering Fracture Mechanics* **1** (1968) 3-43.

[122] Williams, D.P. and H.G. Nelson, *Metallurgical Transactions* **1A** (1970) 63-69.

[123] Gangloff, R.P. and R.P. Wei, *Metallurgical Transactions* **8A** (1977) 1043-1053.

[124] Frandsen, J.D. and H.L. Marcus, *Metallurgical Transactions* **8A** (1977) 265-272.

[125] Gerberich, W.W., T. Livne and X. Chen, in *Modelling Environmental Effects on Crack Growth Processes*, The Metallurgical Society, 1986, pp. 243-257.

[126] Kerns, G. E., M. T. Wang and R. W. Staehle, in Stress Corrosion Cracking and Hydrogen Embrittlement of Iron Base Alloys. National Association of Corrosion Engineers 5 (1973) 700-735.

[127] Perus, T.-P. and C.J. Altstetter, *Metallurgical Transactions* **19A** (1988) 145-152.

[128] Wei, R.P. and R.P. Gangloff, in *Fracture Mechanics: Perspectives and Directions*, ASTM STP 1020 (1989), p.

[129] Lee, S-M., S-I. Pyun and Y-G. Chun, *Metallurgical Transactions* **22A** (1991) 2407-2414.

[130] Huang, F. H. and W. J. Mills, *Metallurgical Transactions* **22A** (1991) 2049-2059.

[131] Pasco, R.W. and P.J. Ficalora, *Scripta Metallurgica* **15** (1981) 1019-1022.

[132] Pasco, R.W., K. Sieradzki and P.J. Ficalora, *Scripta Metallurgica* **16** (1982) 881-883.

[133] Gao, M. and R.P. Wei, *Metallurgical Transactions* **16A** (1985) 2043-2065.

[134] Krausz, A. S. and K. Krausz, in *Materials Engineering for High Risk Environment*, Proc. NUCMAT-88 (A. Niku-Lari ed.) (1988) 1-11.

[135] Krausz, A. S. and K. Krausz, in *Advances in Fracture Research*, ICF-7 (1989) 1611-1620.

[136] R.E. Reed-Hill and J.R. Donoso, *Rev. Def. Beh. Mater.* **2**, 7 (1977).

[137] R.W. Bailey, *J. Inst. Metals* **35** (1926) p. 27.

[138] E. Orowan, J.W. Scot, *Iron Steel Inst.* **54**, 45 (1946-47).

[139] J.E. Dorn, *Dislocation Dynamics*, McGraw-Hill, 1967, p. 27.

[140] V. Celli, M. Kabler, T. Ninomiya and R. Thomson, *Phys. Rev.* **131**, 58 (1963).

[141] J.E. Dorn and S. Rajnak. *Trans. Met. Soc. AIME* **230**, 1052 (1964).

[142] P. Guyot, J.E. Dorn, *Can. J. Phys.* **45**, 983 (1967).

[143] J.P. Hirth, in *Inelastic Behavior of Solids*, McGraw-Hill, New York, 281 (1970).

[144] A.S. Krausz and B. Faucher, *Scripta Met.* **13**, 91 (1979).

[145] U.F. Kocks, A.S. Argon and M.F. Ashby, *Prog. Mater. Sci.* **19**.

[146] A.S. Krausz and B. Faucher, in *Reviews on the Deformation Behavior of Materials* **4**, 105 (1982).

[147] J.F. Wilson and F. Garofalo, *Mater. Res. Stand. ASTM* **6**, 85 (1966).

[148] J.F. Wilson and N.K. Wilson, *Trans. Soc. Rheol.* **10**, 399 (1966).

[149] B. Faucher and W.R. Tyson, in *Constitutive Laws of Plastic Deformation and Fracture*, 19th Canadian Fracture Conference, Ottawa, 1989, p. 27-1.

[150] B.F. Dyson, in *Modelling of Material Behavior and Design*, TMS, 1990, p. 59.

[151] A.S. Argon, *Scripta Met.* **4**, 1001 (1970)

[152] W.G. Johnston, *J. Appl. Phys.* **33**, 2716 (1961).

[153] F. Garofalo, *Trans. AIME* **227**, 351 (1963)

[154] A.G. Guy, *Introduction to Material Science*, McGraw-Hill, 1972.

[155] E. Krempl, *J. Mech. Phys. Solids* **27**, 363 (1979).

[156] V.G. Ramaswamy, D.C. Stouffer and J.H. Laflen, *J. Eng. Mater. Tech.* **112**, 280 (1990).

[157] L.A. Lalli and A.J. DeArdo, *Met. Trans.* **21A**, 3101 (1990).

[158] J. Larry, ed. *Residual Stress for Designers and Metallurgists*, ASM, Metals Park, OH., 1981, p. 56.

[159] M.B. Ruggles and E. Krempl, *J. Eng. Mater. Tech.* **111**, 378 (1989).

[160] J.L. Chaboche and D. Nouailhas, *J. Eng. Mater. Tech.* **111**, 406 (1989).

[161] J. Weertman, *J. Mech. Phys. Solids* **4**, 230 (1956).

[162] J. Weertman, *Trans. AIME* **218**, 207 (1960).

[163] J. Weertman, *Trans. AIME* **227**, 1475 (1963).

[164] O.D. Sherby and J. Weertman, *Acta Met.* **27**, 387 (1969).

[165] F. Garofalo, *Joint Int. Conf. on Creep*, London, 1963, p. 1-31.

[166] A.S. Krausz and K. Krausz, "The Operational Equation of Design for High Temperature Conditions", *Proc. ASME Winter Conference*, Atlanta, Georgia, 1991.

[167] H. Luthy, A.K. Miller and O.D. Sherby, *Acta Met.* **28** (1980) p. 126.

[168] D.B. Warmuth and H.D. Kessler, *Metal Progress* **89**, March 1966, p. 94.

[169] F.R.N. Nabarro, "Report of a Conference on Strength of Solids", The Physical Society, London, 1948. p. 75.

[170] C. Herring, *J. Appl. Phys.* **21**, 437 (1950).

[171] R.L. Coble, *J. Appl. Phys.* **34**, 1679 (1963).

[172] G.B. Gibs, *Mater. Sci. Eng.* **2**, 269 (1967).

[173] R. Raj and M.F. Ashby, *Met. Trans.* **2**, 1113 (1971).

[174] R.C. Gifkins, T.G. Langdon, *Scripta. Met.* **4**, 563 (1970).

[175] F. Garofalo, in *Fundamentals of Creep and Creep-Rupture in Metals*, The Macmillan Co., New York (1965).

Appendix A:

The Absolute Rate Theory

Atoms in condensed phases occupy equilibrium positions and are vibrating about the minimum of the free energy well. Under the combined effect of mechanical forces and thermal vibrations, these atoms will move into a new equilibrium valley while breaking the previous bonds and establishing new bonds. The motion of atoms can be conveniently represented in the 'configuration space'. Generally for a system of N atoms, the configuration space has 3N-5 dimensions to specify their relative position plus one more for the potential energy. The physical concept, however, can be illustrated by the following simple configuration.

Suppose there are three atoms moving with respect to each other in a straight line, Fig. A.1a, the configuration space is then two dimensional, the X-coordinate being the distance of atoms 1 and 2, the Y-coordinate being the distance between 2 and 3. Every point in this configuation space corresponds to a configuration of the three atoms. The forces between these atoms can be derived from the potential energy for this configuration. If we make a landscape over the configuration spcae such that the height at any point is equal to the potential energy for this configuration, Fig. A.1b, a ball rolling on this landscape will represent the motion of the three atoms under the influence of forces among them. The relative motion of the atoms will change in real space in such a way that the corresponding point in configuration space always coincides with the position of the ball.

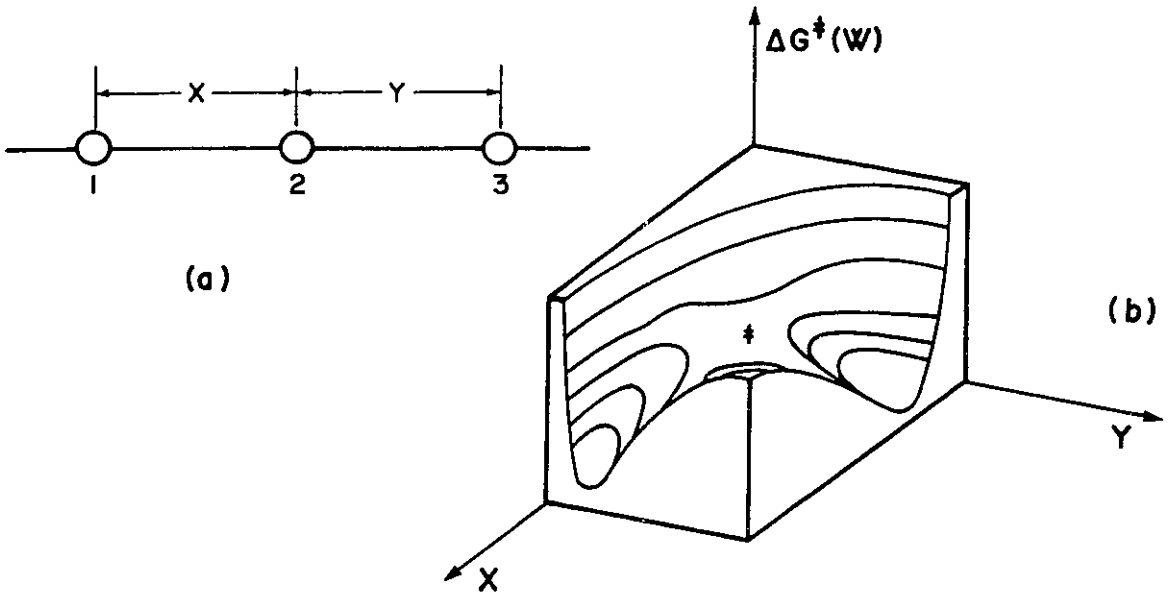

Figure A.1. (a) The coordinates of three atoms moving in a straight line; (b) a typical potential energy surface for the linear three-atom interaction shown in (a).

Equilibrium states correspond to valleys in our landscape. A reaction consist in passing over of our ball from one low region to another. Such a passage will occurs along the path that leads through the lowest saddle point between two valleys. The saddle point is the place of almost no return and is called the transition or activated complex, denoted by "‡".

By assuming a thermodynamic equilibrium to exist between the initial and the activated states, the specific rate of a reaction can be determin calculating the concentration of the activated complexes and the rate of passage across the saddle point using the methods of statistical mechanics.

The rate of reaction over a single potential barrier is

$$\text{rate} = C^{\ddagger}\frac{\bar{v}}{\Delta}$$

where $C^{\ddagger}$ is the concentration of activated complexes per unit volume lying in the length Δ along the reaction path at the activated state; $\bar{v}$ is mean velocity of the activated complexes moving within the distance Δ. Using Boltzmann statistics, $\bar{v}$ can be calculated as

$$\bar{v} = \left(\frac{kT}{2\pi m^{\ddagger}}\right)^{1/2}.$$

where $m^{\ddagger}$ is the mass of the activated complex in motion through the distance Δ, k is the Boltzmann constant, and T is the absolute temprature. The activation distance Δ can be defined as

$$\Delta = h\sqrt{2\pi m^{\ddagger} kT}$$

such that the translational partition function along the reaction coordinate is nomalized to unity, where h is Plank's constant. The ratio v/Δ represents the frequency of emptying the length of path Δ of activated complexes.

Accordingly,

$$\text{rate} = \frac{kT}{h} C^{\ddagger}$$

In equilibrium, according to Boltzmann statistics, the fraction of particles at the ith energy level with respect to the total number of particles N_t is

$$\frac{N_i}{N_t} = \frac{\exp(-\Delta E_i/kT)}{\sum_j \exp(-\Delta E_j/kT)}$$

Then, the ratio between the number of atoms in the activated state, $N_{\ddagger}$, with respect to the total number of atoms, N_t ($N_t = N_{\ddagger} + N_r$, where N_r is the number of reactant), is

$$\begin{aligned}
\frac{N_{\ddagger}}{N_t} &= \frac{N_{\ddagger}}{N_r + N_{\ddagger}} \\
&= \frac{[\sum_j \exp(-\Delta E_i/kT)]_{\ddagger}}{[\sum_j \exp(-\Delta E_j/kT)]_r + [\sum_j \exp(-\Delta E_j/kT)]_{\ddagger}} \\
&= \frac{Q_{\ddagger}}{Q_r + Q_{\ddagger}}
\end{aligned}$$

where Q is the partition function. Similar relation also holds for N_r.

Hence,

$$\frac{C^{\ddagger}}{C_r} = \frac{N_{\ddagger}}{N_r} = \frac{Q_{\ddagger}}{Q_r}$$

Accordingly,

$$\begin{aligned} \text{rate} &= \frac{kT}{h}\frac{Q_{\ddagger}}{Q_r}C_r \\ &= \frac{kT}{h}\exp\left(-\frac{\Delta G^{\ddagger}}{kT}\right)C_r, \end{aligned}$$

here the definition $G = -kTlnQ$ has been used. $\Delta G^{\ddagger}$, therefore, is the difference of Gibbs free energy between the reactant and the activated states at absolute zero.

It is customary in chemical kinetics to define a rate constant k so that

$$\text{rate} = \mathsf{k}C_r$$

where

$$\mathsf{k} = \frac{kT}{h}\exp\left(-\frac{\Delta G^{\ddagger}(W)}{kT}\right)$$

Appendix B:

Linear Elastic Crack-Tip Field (I)

Fracture processes are controlled by the stress-strain fields at the crack tip. Except in an ideal brittle material, non-linear deformation will occur in the near-tip region due to stress concentration. The results of linear elastic analysis for a cracked body depends on the crack length and the dimension of the non-linear deformation zone which, in most cases, are much smaller than other characteristic dimensions. The non-linear deformation that satisfies this condition is called **small scale yielding** which is embodied in the concept of LEFM.

In a two-dimensional crack problem, let the origin of the oxy coordinates be set at the crack tip with the x-axis pointing the main crack direction, as shown in Figure B1, the near-tip stress field (mode I) is expressed as [22]

$$\begin{aligned}
\sigma_x &= \frac{K}{\sqrt{2\pi r}} \cos\frac{\theta}{2}\left[1 - \sin\frac{\theta}{2}\sin\frac{3\theta}{2}\right] \\
\tau_{xy} &= \frac{K}{\sqrt{2\pi r}} \sin\frac{\theta}{2}\cos\frac{\theta}{2}\cos\frac{3\theta}{2} \\
\sigma_y &= \frac{K}{\sqrt{2\pi r}} \cos\frac{\theta}{2}\left[1 + \sin\frac{\theta}{2}\sin\frac{3\theta}{2}\right]
\end{aligned}$$

where r and θ are the polar coordinates defining point P, K is the stress intensity factor.

The shear stress on the plane that lies at the θ angle with respect to the crack plane can be obtained by stress transformation as

$$\begin{aligned} \tau_\theta &= \tau_{xy}\cos 2\theta + \frac{\sigma_y - \sigma_x}{2}\sin 2\theta \\ &= \frac{K}{\sqrt{2\pi r}}\frac{1}{2}\sin\theta\cos\frac{\theta}{2}. \end{aligned}$$

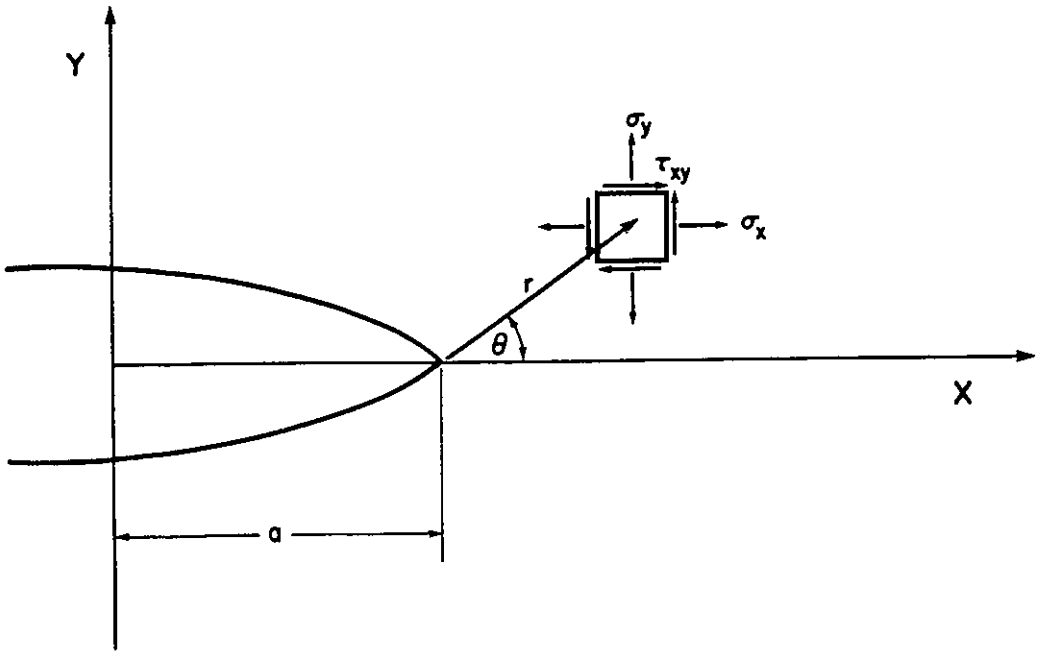

Figure B.1. The coordinate system and stresses associated with the description of LEFM

Appendix C:

Linear Elastic Crack-Tip Field (II)

In LEFM, a crack problem can be, by the principle of superposition, decomposed into (1) the stress problem of an uncracked body with the prescribed stress and displacement boundaries (denoted as S_T and S_u respectively) and (2) the stress problem of the cracked body with a distribution of stress, σ_n, along the crack surfaces which is oppsite in sign and equal to the resolved stress on the assumed crack plane in problem 1, as shown in Figure C1. The crack-tip field is then obtained by solving problem 2, which can be expressed in a generalized form as (Appendix B)

$$\sigma_{ij} = \frac{K}{\sqrt{2\pi r}} f_{ij}(\theta)$$

where the stress intensity factor can be expressed as

$$K = Y\sigma_n\sqrt{\pi a},$$

Y is the shape factor.

If the crack plane is inclined to the stress axis at an angle ϕ, as shown in Figure 4.12, the resolved stress on the crack plane will be given by dividing the resolved load, $P\cos\phi$, by the area of the inclined plane, $A/\cos\phi$ (A is the area of the plane normal to the stress axis), and this yields

$$\sigma_n = \frac{P}{A}\cos^2\phi.$$

Accordingly, the crack tip stress fields for such a crack configuration is expressed as

$$\sigma_{ij} = \frac{K}{\sqrt{2\pi r}} f_{ij}(\theta)\cos^2\phi$$

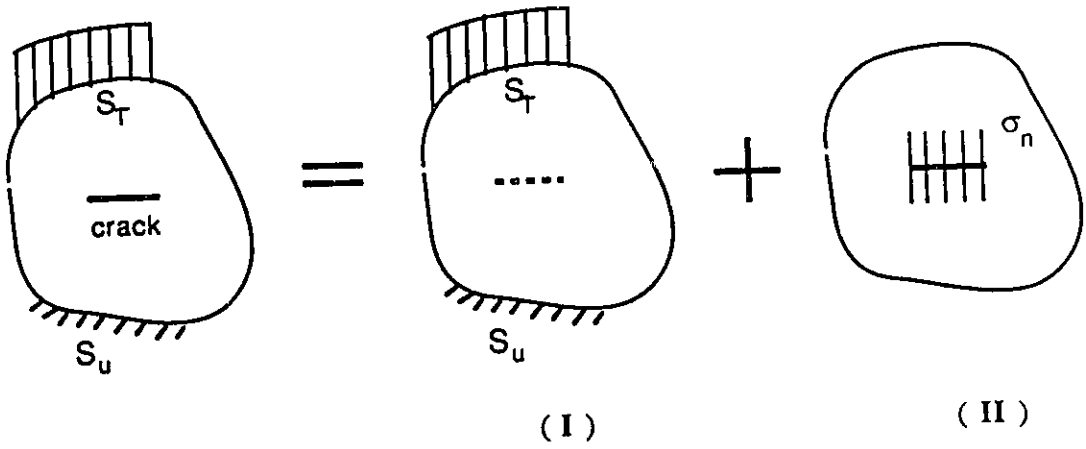

Figure C.1. Decomposition of a crack problem into problems I and II.

Appendix D

Let $\gamma_p(i)$ denote the accumulated plastic strain after i cycle. In the n-th cycle, plastic flow starts at t_s when

$$\Phi(t_s) = \frac{V}{kT}[\tau_{max} - \dot{\tau}(t_R - t_s) - H\gamma_p(n-1) - \tau_0] = 0 \tag{8.7}$$

and ceases at t_f when

$$\Phi(t_f) = \frac{V}{kT}[\tau_{max} - \dot{\tau}(t_f - t_R) - H\gamma_p(n) - \tau_0] = 0. \tag{8.8}$$

From equation (7.28),

$$t_f - t_R = \frac{kT}{V\dot{\tau}\sqrt{1+\lambda^2}} \ln \frac{(1+p)(q-\lambda u_R)}{(q-\lambda)(u_R+p)}. \tag{8.9}$$

Substituting equation (12.3) into (12.2), by rearrangement,

$$\gamma_p(n) - \gamma_p(n-1) = \frac{1}{H}[\tau_{max} - H\gamma_p(n-1) - \tau_0] - \frac{kT}{HV\sqrt{1+\lambda^2}} \ln \frac{(1+p)(q-\lambda u_R)}{(q-\lambda)(u_R+p)} \tag{8.10}$$

where u_R can be obtained from equation (7.26) as

$$\begin{aligned} \frac{u_R - p}{\lambda u_R + q} &= \frac{1-p}{\lambda+q} \exp\left(-\frac{V\dot{\tau}\sqrt{1+\lambda^2}(t_R - t_s)}{kT}\right) \\ &= \frac{1-p}{\lambda+q} \exp\left(-\frac{V\sqrt{1+\lambda^2}[\tau_{max} - H\gamma_p(n-1) - \tau_0]}{kT}\right). \end{aligned}$$

At low temperatures where $\lambda \ll 1$, then $p \cong \lambda/2, q \cong 1$, and

$$u_R \cong p + \exp\left(-\frac{V[\tau_{max} - H\gamma_p(n-1) - \tau_0]}{kT}\right),$$

equation (12.4) reduces to

$$\Delta\gamma_p = \frac{kT}{VH}\left[\Phi(n-1) + \ln\left(\frac{2AH}{\dot{\tau}} + \exp[-\Phi(n-1)]\right)\right] \tag{8.11}$$

where

$$\Delta\gamma_p = \gamma_p(n) - \gamma_p(n-1)$$

$$\Phi(n-1) = \frac{V}{kT}[\tau_{max} - H\gamma_p(n-1) - \tau_0].$$

Writing equation (40) in a continuous form results in

$$\frac{d\gamma_p}{dN} = \frac{kT}{VH}\left[\Phi + \ln\left(\frac{2AH}{\dot{\tau}} + \exp(-\Phi)\right)\right],$$

$$\Phi = \frac{V}{kT}(\tau_{max} - H\gamma_p - \tau_0).$$